MULTIDISCIPLINARY DESIGN OF AN INTEGRATED MICROBURST ALERTING SYSTEM

by

CRAIG R. WANKE

S.B., Massachusetts Institute of Technology (1988)
S.M., Massachusetts Institute of Technology (1990)

SUBMITTED IN PARTIAL FULFILLMENT
OF THE REQUIREMENTS FOR THE
DEGREE OF

DOCTOR OF PHILOSOPHY IN
AERONAUTICS AND ASTRONAUTICS

at the

MASSACHUSETTS INSTITUTE OF TECHNOLOGY
June 1993

Signature of Author _____
Department of Aeronautics and Astronautics
March 1993

Certified by _____
Associate Professor R. John Hansman
Department of Aeronautics and Astronautics
Committee Chairman

Certified by _____
Professor Walter M. Hollister
Department of Aeronautics and Astronautics

Certified by _____
Associate Professor Steven R. Hall
Department of Aeronautics and Astronautics

Accepted by _____
Professor Harold Y. Wachman
Chairman, Department Graduate Committee

Multidisciplinary Design Of An Integrated Microburst Alerting System

by

Craig R. Wanke

Submitted to the Department of Aeronautics and Astronautics
in partial fulfillment of the requirements for the Degree of
Doctor of Philosophy

Abstract

Low altitude wind shear is the leading weather-related cause of fatal aviation accidents in the United States. Localized intense downdrafts known as microbursts are the most dangerous form of wind shear, and pose a serious hazard to aircraft during takeoff or approach. New developments in microburst sensing, ground-air digital data transmission, and electronic cockpit instrumentation are providing a variety of capabilities and options for development of an effective microburst alerting system. In this work, a user-centered approach was applied to identify and analyze critical system design issues in a series of multidisciplinary studies. This approach is designed to optimize the decision-making performance of the end user, and thereby optimize the operational efficiency of the microburst alerting system.

The primary end users of microburst alerts are flight crews, so the initial task was to determine which information is required by the crew for effective microburst alerting and the most effective presentation techniques for this information. This was done with a pilot survey and with two piloted part-task simulator experiments. Iconic graphical alerts were found to be significantly more useful than verbal or text communications, and several format and procedural issues for implementation of graphical alerts were examined. These studies included development of a part-task flight simulator, based on an advanced workstation with powerful graphics and rapid prototyping capabilities, which was found to be an exceptionally useful tool for preliminary evaluation of advanced cockpit information systems. Next, the issue of producing the required alert information - the alert generation task - was addressed. Possible hazard metrics for microburst intensity were compared, and an effective one selected based on a batch flight simulation technique. The energy-based "F-factor" criterion averaged over 3000 ft of aircraft flight path was found to be a much better indicator of aircraft hazard than the "delta-V" (total headwind-to-tailwind change) criterion currently used by the Terminal Doppler Weather Radar (TDWR) microburst detection system and the Low Level Windshear Alert System (LLWAS). A method was then developed for establishing a multi-level microburst alerting structure, using threshold values of a hazard metric based on measureable airmass parameters. The method was applied to determine three-level alerting thresholds for jet transports on approach to landing. Alert generation requires estimates of microburst characteristics; a model-based data assimilation technique for estimating microburst characteristics from multi-sensor measurements was therefore developed. The extended Kalman filter-based technique incorporates elementary fluid mechanics and statistical characteristics of microbursts to improve estimation accuracy, and to allow estimation of quantities which cannot be directly measured. The model-based approach which was developed is quite general and may have applications for other multi-sensor measurement problems. Finally, the implications of the these studies for current, near-term, and possible future microburst alerting systems were examined.

Acknowledgements

Many people have contributed greatly to the completion of this thesis. First, I would like to thank Professor R. John Hansman, who as my advisor throughout my graduate career has been my chief mentor, motivator, problem solver, and idea backboard. The efforts and advice of Dr. Steven Campbell of MIT Lincoln Laboratory and David Hinton of NASA Langley Research Center were also instrumental. I would like to acknowledge my doctoral committee - Professors Walter Hollister, Steven Hall, and Mark Drela - and the rest of the outstanding faculty of the MIT Aero/Astro Department for teaching me the art of engineering. The quarterly meetings of the FAA/NASA Joint University Program for Air Transportation Research were also an important source of constructive criticism throughout the course of this work.

The personal support I received from my family, especially my parents, Rudolph and Helen Wanke and my fianceé Claudia Ranniger, was essential to my motivation and well-being. Their contributions are a part of every chapter, section, figure, and table in this thesis.

I would like to thank the impressive number of graduate students who have passed through the hallowed halls of the Aeronautical Systems Lab during my stay for the many interesting and deep discussions about research, life, the universe and everything. I would especially like to acknowledge the efforts of the graduate and undergraduate students who sweated and toiled over the MIT Advanced Cockpit Simulator - Ed Hahn, Amy Pritchett, Divya Chandra, Jim Kuchar, and Mark Mykityshyn. May its capabilities continue to expand without bound.

This research was supported by the National Aeronautics and Space Administration (NASA) and MIT Lincoln Laboratory under Air Force Contract No. F19628-90-C-0002, and by the Federal Aviation Administration and NASA under grant NGL-22-009-640. The TASS microburst simulation data was provided by Fred Proctor of NASA Langley Research Center. The cooperation of the Air Line Pilots Association (ALPA) and United Airlines made the Terminal Area Windshear Survey possible, and the continued support of ALPA and the many pilots who volunteered their time for both part-task piloted simulator experiments was essential to their success.

Table of Contents

Nomenclature

In the following list, symbols defined specifically for this work are followed by the parenthesized chapter number in which they are first defined. Symbols with multiple meanings are similarly identified by chapter number or appendix letter. Boldface lowercase symbols indicate vector quantities and boldface uppercase symbols indicate matrices.

A	microburst dynamic model, state dynamics matrix (7)
AD	approach degradation (6)
B	microburst dynamic model, deterministic input matrix (7)
C_D	aircraft drag coefficient
C_L	aircraft lift coefficient
d	glideslope altitude deviation (6)
D	aircraft drag
e	vector of wind modeling errors (7)
E	aircraft total energy (2)
F	F-factor (2, 5, 6, 7) or objective function (D)
F_{av}	F-factor averaged over 1 km of aircraft flight path (6)
g	gravitational acceleration
g	gradient of objective function (D)
h	altitude
h_p	potential altitude (2)
h	vector of equations relating state variables to measurements (7)
H	linearized measurement matrix (7)
I	identity matrix
J	Jacobean matrix (D)
K	Kalman filter gain matrix (7)
L	aircraft lift
L	microburst dynamic model, process noise input matrix (7)
M_{extent}	Microburst extent estimation figure-of-merit (7)
MI_{ap}	microburst impact parameter for approach to landing (6)
MI_{to}	microburst impact parameter for takeoff (6)
m	aircraft mass
p	search direction for minimization (D)

$\mathbf{P}$	estimation error covariance matrix (7)
$\mathbf{Q}$	process noise covariance matrix (7)
r	radial distance (C)
R_p	OBV model, microburst core radius (6, 7, C)
$\mathbf{R}$	measurement noise covariance matrix
s	Laplace transform frequency variable
S	aircraft wing reference area
t	time
t_k	time of measurements (7)
T	aircraft thrust
TD	takeoff degradation (6)
$\mathbf{u}$	deterministic input vector (7)
U_0	modified OBV model, eastward ambient wind speed (7, C)
U_h	modified OBV model, eastward ambient wind altitude gradient (7, C)
U_m	OBV model, maximum outflow speed (6, 7, C)
$\mathbf{v}$	measurement noise vector (7)
V	airspeed
V_0	modified OBV model, northward ambient wind speed (7, C)
V_h	modified OBV model, northward ambient wind altitude gradient (7, C)
$\mathbf{w}$	process noise vector (7)
W	aircraft weight
$\mathbf{W}$	vector of wind measurements (7)
W_r	horizontal wind velocity, radially outward from sensor (C)
W_x	horizontal wind velocity along aircraft heading (tailwind positive)
W_{xE}	eastward wind velocity (Earth-referenced)
W_{yE}	northward wind velocity (Earth-referenced)
W_h	vertical wind velocity (updraft positive)
x	eastward distance (7, C)
x_0	OBV model, east microburst core location (7, C)
$\mathbf{x}$	vector of microburst model parameters (7, C)
$\hat{\mathbf{x}}$	estimated microburst model parameter vector (7)
y	northward distance (7, C)

y_0	OBV model, north microburst core location (7, C)
$\mathbf{z}$	wind measurement vector (7)
Z_m	OBV model, altitude of maximum outflow speed (6, 7, C)
α	aircraft angle of attack (6) or OBV model radial shaping parameter (C) or linear search step (D)
α_{ss}	stick shaker angle-of-attack
δ_f	aircraft flap deflection
γ_a	aircraft air-mass relative flight path angle
γ_i	aircraft inertial flight path angle
η	angular glideslope displacement (6)
λ	OBV model scale factor (C)
μ	coefficient of dynamic friction (B) or linear search convergence parameter (D)
θ	aircraft pitch angle (6) or sensor elevation angle (C)
ρ	air density
ψ	sensor azimuth angle (C)
ω	linear search gain reduction multiplier (D)
$\dot{(\,)}$	time derivative of ( )
$(\,)_i$	( ) at the i^{th} update iteration (7)
$(\,)_j$	j^{th} component of vector ( )
$(\,)_k$	( ) at measurement time, t_k (7)
$(\,)^-$	( ) prior to measurement update (7)
$(\,)^+$	( ) after measurement update (7)

Acronyms

ABDR	Airborne Doppler Radar
ACARS	ARINC Communications Addressing and Reporting System
AGL	Above Ground Level (altitude)
ARINC	Aeronautical Radio, Inc.
ASL	Aeronautical Systems Laboratory
ASR	Airport Surveillance Radar
ATC	Air Traffic Control
ATIS	Automatic Terminal Information Service
CDU	Control Display Unit
CRT	Cathode Ray Tube
DEN	Denver-Stapleton International Airport
DFW	Dallas-Fort Worth Airport
EADI	Electronic Attitude Director Indicator
EFIS	Electronic Flight Instrumentation System
EHSI	Electronic Horizontal Situation Indicator
EKF	Extended Kalman Filter
ELM	Extended Length Message (Mode-S)
FAA	Federal Aviation Administration
FLOPS	Floating Point Operations
FMC	Flight Management Computer
GSD	Geographical Situation Display
IEKF	Iterated Extended Kalman Filter
INS	Inertial Navigation System
IR	Infrared
KIAS	Knots, Indicated Airspeed
LCD	Liquid Crystal Display
LIDAR	Light Detection and Ranging
LLWAS	Low-Level Windshear Alert System
LNAV	Lateral Navigation (FMC)
MCP	Mode Control Panel
MIT	Massachusetts Institute of Technology
NASA	National Aeronautics and Space Administration
NCAR	National Committee for Atmospheric Research
OBV	Oseguera-Bowles-Vicroy (microburst model)
PFD	Primary Flight Display
PIREP	Pilot Report
RADAR	Radio Detection and Ranging
TASS	Terminal Area Simulation System
TDWR	Terminal Doppler Weather Radar
VHF	Very High Frequency
VOR	VHF Omnidirectional Ranging
VNAV	Vertical Navigation (FMC)
WTA	Windshear Training Aid

1. Introduction

Low altitude wind shear is the leading weather-related cause of fatal aviation accidents in the U.S. Since 1964, there have been 26 accidents attributed to wind shear resulting in over 500 fatalities [National Research Council, 1983; Wolfson, 1988]. The localized intense downdrafts known as microbursts are the most dangerous form of wind shear, and pose a serious hazard to aircraft during takeoff or approach. For this reason development of sensors for wind shear detection has been a very active research area. In addition, recent developments in ground-to-air digital datalinks and electronic cockpit instrumentation have provided new options for dissemination and presentation of ground-measured microburst alerts. Integration of these new technologies to provide effective microburst detection and alerting constitutes a complex multidisciplinary system engineering problem.

A microburst detection and alerting system needs to perform a series of separate but connected subtasks, illustrated in Figure 1.1. First, data from one or several sensors is processed to detect, locate, and measure characteristics of microbursts. Next, the microburst hazard is evaluated based on the sensor data and the current operational situation. Alerts are then formulated and disseminated to Air Traffic Control (ATC) and affected aircraft. Finally, alerts are presented to the flight crew to best aid in avoiding or escaping the microburst. In the course of this research, several issues critical to the performance of these subtasks were isolated and addressed. These include:

(1) Selection of effective microburst alert information content and cockpit presentation format

(2) Generation of microburst alerts based on the evaluated hazard

(3) Evaluation of the microburst hazard to aircraft based on measureable microburst characteristics

(4) Assimilation of data from several wind shear sensor systems into a combined hazard assessment ("data fusion")

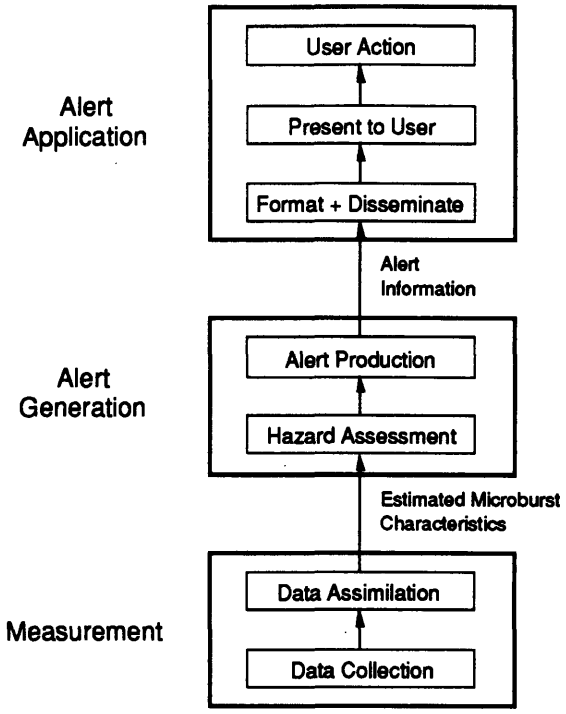

Figure 1.1. Microburst Alerting Task Breakdown

This report documents the analyses and experiments done to address each of the above issues, and discusses their implications for overall microburst alerting system design. Chapter 2 provides a background review including a summary of microburst meteorology and a review of current microburst detection, alert dissemination, and cockpit presentation technologies. Chapter 3 outlines the user-centered, top-down design approach used in this work and presents an overview of the specific studies which were done. The user requirements definition phase included a pilot opinion survey on wind shear (Chapter 4) and two piloted part-task simulator studies of candidate microburst alert formats (Chapter 5). Chapter 6 presents a batch flight simulation study of metrics for microburst hazard assessment. A technique for establishing multi-level alert hazard thresholds is also developed. An algorithm for multi-sensor estimation of microburst characteristics is described in Chapter 7. Chapter 8 discusses the implications of these studies for current and future microburst alerting systems. Finally, the major results and contributions of this work are summarized in Chapter 9.

2. Background

2.1. The Microburst Threat

2.1.1. Meteorology

The existence of "downbursts" as an aviation hazard was first hypothesized by Fujita and Byers [1977] to explain the crash of Eastern Flight 66 on 24 June 1975 at New York's John F. Kennedy airport. A downburst is a descending column of air which strikes the ground and spreads out in a radial pattern, similar to that formed by a jet of fluid striking a solid wall. The outflowing winds can also form a horizontal ring vortex (Figure 2.1). Downbursts have been observed to cause tornado-like damage such as flattened trees and buildings due to the high wind speeds which can occur. Downbursts have been classified into "macrobursts" and "microbursts" according to the size of the high wind region. Microbursts are defined to have a horizontal extent of less than 4 km, and macrobursts of larger than 4 km. The majority of wind shear related fatal aviation accidents have been attributed to microbursts, which have produced measured wind speeds of as much as 75 m/s (168 mph) [Fujita, 1985].

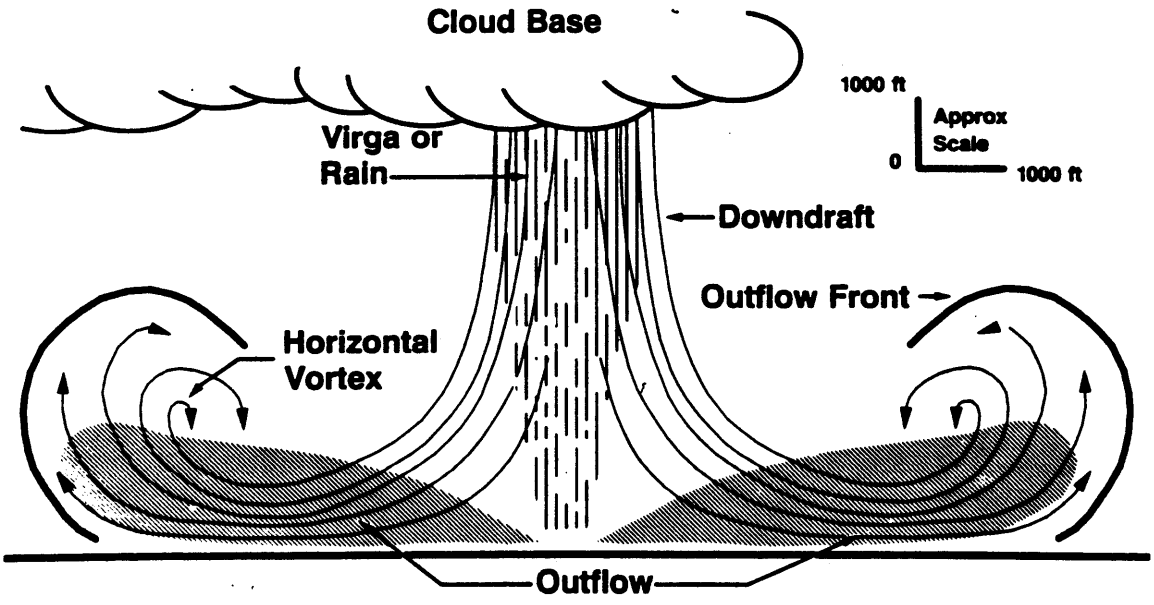

Figure 2.1. Cross-sectional view of a microburst. Viewed from above, the outflow region would appear roughly circular or elliptical. Reproduced from the Windshear Training Aid [FAA, 1987].

Observational studies have indicated that several different weather patterns can produce microbursts [Wolfson, 1988]. Isolated cumulonumbus clouds, also known as "air mass thunderstorms," can produce strong microbursts accompanied by heavy rain. These storms typically occur on hot, humid summer afternoons, and are common in many parts of the United States. The "wet" microbursts resulting from these storms are particularly hazardous to aircraft, since they can have very strong outflows and are often accompanied by heavy rain.

Wet downbursts, both microbursts and microbursts, can also be produced by larger scale storm complexes or frontal storms. This type of microburst-producing storm typically exhibits high radar reflectivity (at least 50 dbZ) and is easily recognized as an aviation hazard. In addition, these storms are long-lived and follow fairly predictable paths. Therefore, the associated microbursts are normally avoided by standard thunderstorm avoidance procedures.

The microburst forms discussed above have been termed "wet" microbursts since they are associated with significant rainfall. "Dry" microbursts, in which little or no rain reaches the surface, have also been observed to occur. These microbursts are typically produced by shallow, high-based cumulonumbus clouds. Dry microbursts have principally been observed in the high plains regions east of the Rocky Mountains during summer afternoons. They occur when precipitation falling from a high cloud base evaporates, cooling the air and producing an associated downdraft. The evaporating precipitation appears as hazy shafts below the cloud base. These "virga" are the primary visual evidence of a dry microburst.

Single microbursts typically have lifetimes on the order of 15 minutes. This short lifespan and correspondingly short development time adds to the microburst hazard, due to the difficulty of detection and alerting in the little time available. Dry microbursts can also occur in roughly linear groups known as "microburst lines." Since microburst lines

typically last about 1 hour and propagate very slowly (mean speed 1.3 m/s), they can have a strong impact on airport operations. These same characteristics imply that they can be more easily detected than single microbursts. Wet microbursts have also been observed to occur in groups, but do not typically organize into long-lived microburst lines.

2.1.2. Effect on Aircraft

The aviation hazard posed by microbursts has two major components. An aircraft entering a microburst first encounters a performance-increasing headwind. This is followed by a downdraft and a rapid transition from headwind to tailwind, both of which tend to drive the aircraft below glideslope and reduce airspeed (Figure 2.2). These effects are aggravated if the pilot or autopilot is unaware of the microburst, and reduces thrust during the headwind portion of the event to prevent the aircraft from rising above the glideslope.

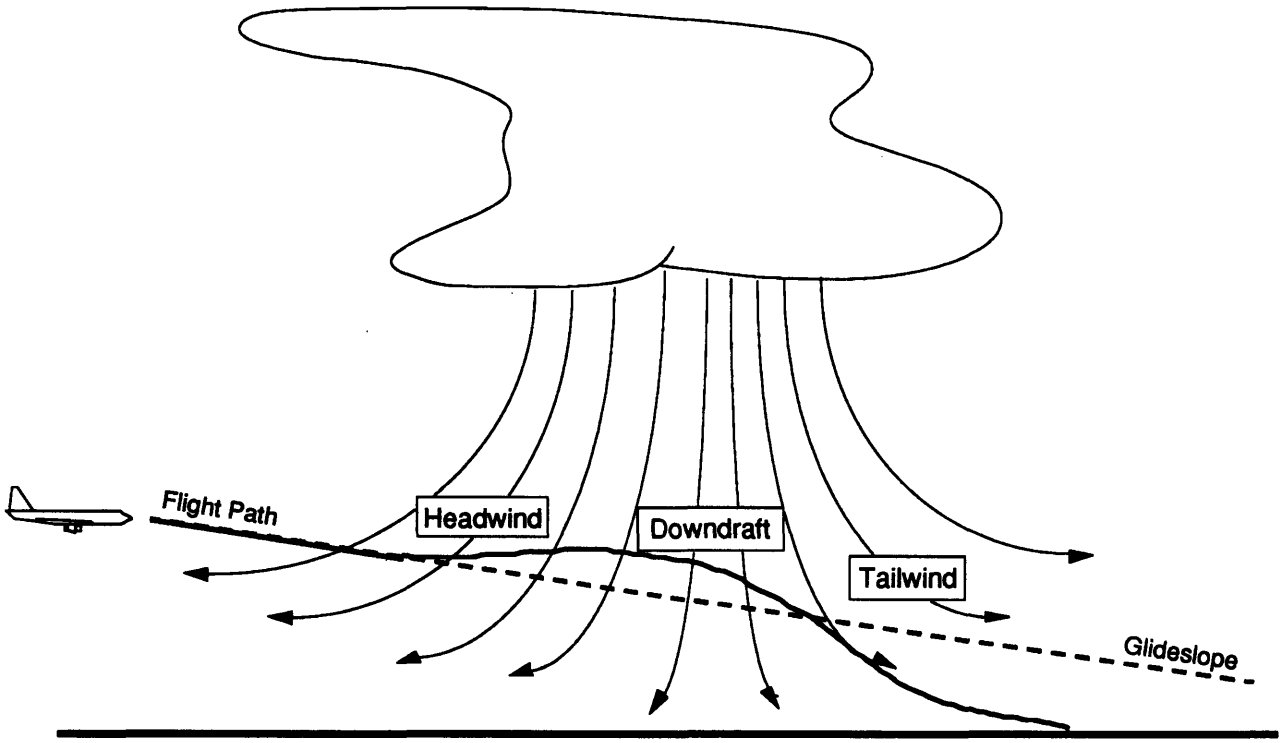

Figure 2.2. Microburst encounter on approach.

A quantitative measure of the impact of microbursts on aircraft has been developed by researchers at the NASA Langley Research Center [Bowles, 1990; Hinton, 1990]. This measure, called F-factor, is based on analysis of the total energy of an aircraft and how it is affected by the local windfield. The energy state of an aircraft can be quantified by summing the air-relative kinetic energy and the ground-relative potential energy. The air-relative kinetic energy is used since the air-relative velocity (airspeed) rather than the inertial speed impacts the immediate climb capability of the aircraft. Similarly, the altitude above ground-level (AGL) is more relevant to aircraft recovery than barometric altitude. This energy sum per unit weight (specific energy), also referred to as "potential altitude" or "aircraft energy height," is:

$$h_p = \frac{E}{W} = \frac{V^2}{2g} + h \tag{2.1}$$

where V is aircraft airspeed, h is AGL altitude, and g is sea level gravitational acceleration. Assuming that airspeed can be converted to climb rate with no energy losses, the time rate of change of this quantity is equivalent to the potential rate of climb of the airplane:

$$\dot{h}_p = V\left(\frac{\dot{V}}{g}\right) + \dot{h} \tag{2.2}$$

Combining this definition with point-mass longitudinal equations of motion for flight in a non-uniform atmosphere, the potential rate of climb becomes:

$$\dot{h}_p = V\left\{\left(\frac{T - D}{W}\right) - \left[\frac{\dot{W}_x}{g}\cos\gamma_a + \frac{\dot{W}_h}{g}\sin\gamma_a - \frac{W_h}{V}\right]\right\} \tag{2.3}$$

where W_x is the tailwind-positive horizontal wind component, W_h is the updraft-positive vertical wind component, T is engine thrust, D is aircraft drag, and γ_a is flight-path angle relative to the airmass. Note that $\dot{W}_x$ is the time derivative of the horizontal wind *in the aircraft frame*. The bracketed term in the above expression contains the effect of wind

shear on potential rate of climb. Assuming small flight-path angles, the term in brackets becomes:

$$F \equiv \frac{\dot{W}_x}{g} - \frac{W_h}{V} \tag{2.4}$$

and is denoted "F-factor." The expression for potential climb rate then reduces to:

$$\dot{h}_p = V\left(\frac{T - D}{W} - F\right) \tag{2.5}$$

Equation 2.5 indicates that F is a direct measure of the loss in available climb rate (for a constant airspeed trajectory) or, equivalently, the loss in available *excess thrust-to-weight ratio* (T - D)/W due to the local windfield. Positive values of F indicate a performance-decreasing situation with loss of climb capability, and negative values indicate performance-enhancing winds. If F exceeds the excess thrust-to-weight ratio for a particular aircraft, that aircraft will be unable to maintain altitude and must descend. This constitutes a hazardous situation during takeoff and landing operations. For this reason, F is often referred to as "hazard factor" and is an *instantaneous* measure of the hazard posed by the immediate windfield.

F is a non-dimensional quantity, and a function purely of the local winds and airspeed. It contains two components, one due to head-to-tailwind shear and one due to downdraft. At lower altitudes, the shear term dominates due to high microburst outflow velocities; at higher altitudes, the downdraft term dominates due to the descending cool air in the microburst core. The use of F as a hazard criterion and for alert thresholds will be discussed in ensuing chapters.

Another component of the aviation hazard is due to short-scale phenomena such as vortices and severe turbulence (both of which have been associated with microbursts). These short-scale events can destabilize the aircraft and degrade performance. F-factor does not take these effects into account since it is based on point-mass aircraft motion

equations and does not include short time scale aircraft dynamics. The crash of Delta 191 at Dallas-Fort Worth Airport in 1985 provides an illustrative historical case [Fujita, 1986]. The microburst windfield during this event included several strong vortices on the scale of the aircraft length and wingspan. Flight recorder data indicates that the aircraft experienced large rolling motions (up to 20° from level) and large pitch angle excursions (from +14° to -9°). At the time of impact, the airspeed (approximately 165 KIAS) was still well above stall and the aircraft had sufficient energy to avoid ground contact. The short-scale vortex disturbances apparently made the aircraft difficult to control and reduced the ability of the pilot to fly a recovery maneuver. Piloted simulations have been performed with simulated winds from the DFW case and support this hypothesis. [Hinton, 1989].

2.2. Microburst Sensing Systems

Both airborne and ground-based microburst detection systems are being developed, based on a variety of sensor technologies. Ground-based systems are generally more mature than airborne systems, and in some cases are already in the deployment phase.

2.2.1 Ground-Based Systems

LLWAS. The Low Level Wind Shear Alert System (LLWAS), currently in service at most major U.S. airports, is a system of anemometers (usually 5 or 6) designed to measure shifts in surface wind speed and direction within the airport perimeter. New measurements are received at 10 second intervals. LLWAS can detect macroscopic wind shears such as gustfronts; however the anemometer spacing is larger than the characteristic surface dimension of many microbursts, and thus the standard LLWAS is fairly ineffective for microburst detection [National Research Council, 1983]. An extended version of LLWAS including up to 16 anemometers with tighter spacing is

currently under development [Wilson and Gramzow, 1991]. The extended systems cover approach/departure corridors in addition to the airport surface, and have been successful in detecting a severe microburst and saving at least one approaching transport category aircraft during a test at Denver's Stapleton Airport in 1989 [Wilson and Gramzow, 1990]. Advanced LLWAS systems are scheduled for installation at seven major airports in 1992, and other existing systems have been slightly upgraded as an interim measure.

TDWR. The most effective ground-based system is Terminal Doppler Weather Radar (TDWR). TDWR is a C-band, pencil-beam, pulsed Doppler weather radar, located 10-15 km from the airport, which measures winds over the airport and associated approach/departure corridors. The Doppler radar measures wind components radial to the radar beam. The radar emits pulses of microwave energy, of which some is reflected by airborne particulates (precipitation, dust, insects, etc.) in the target volume. Wind velocities are computed from the Doppler shift present in the reflected energy, assuming that the airborne particles are traveling at the speed of the wind. Microbursts are detected by isolating regions of radial shear in the measured radial velocity field [Merritt et. al., 1989]. TDWR microburst measurements are available at 1 minute intervals.

Several years of TDWR operational evaluations have proven the ability to reliably detect both wet and dry microbursts, especially strong ones. As shown in Table 2.1, a 98.5% probability of detection was achieved for microbursts with at least 20 m/s horizontal velocity change [Campbell et. al. 1989]. This was accompanied by a false alarm probability of only 5.2%.

Ground-based radars such as TDWR have greater microburst detection capabilities than airborne radars due to the greater available power and reduced ground-clutter problems due to upward look angles. A corresponding disadvantage is that a single TDWR cannot be sited so as to look directly down the approach and departure corridors of all an airport's runways. Since Doppler radars cannot measure winds

Table 2.1. TDWR microburst detection performance. ΔV is the maximum measured horizontal wind change across the microburst. Huntsville microbursts are primarily "wet", Denver's are primarily "dry".

Data Set	Number of Microbursts	Microburst Detection		
		ΔV < 20 m/s	ΔV ≥ 20m/s	All
Huntsville, 1986	48	85.6%	100.0%	89.2%
Denver, 1987/88	78	83.7%	97.9%	87.8%
All Data	126	85.4%	98.5%	88.4%

perpendicular to the radar beam, this means that TDWR cannot always measure the winds directly along the aircraft flight path (as airborne radars do).

The TDWR system also detects gustfronts and precipitation, and all TDWR products are provided to the control tower on a graphical display for alerting and planning purposes. Current plans call for 47 total TDWR installations in the U.S. [Evans, 1991; Moore et. al. 1991]. Further plans include development of a microburst prediction product, which could potentially give 5 minute warning of impending microbursts. The prediction algorithm uses the ability of the TDWR to scan aloft for events which have been observed to precede microburst formation [Campbell, 1991].

Airport Surveillance Radar. Airport surveillance radars, specifically the ASR-9, have also demonstrated some capability for wind shear detection. The ASR-9 has a "fan beam" antenna, which has a radiation pattern broad in elevation. This antenna has significantly lower gain than a pencil-beam radar antenna (as with TDWR), limiting achievable signal-to-noise ratios and hence detection capability. In addition, the ASR-9 experiences intense ground clutter at short ranges. Despite these limitations, testing has indicated a probability of detection of 97% for microbursts with greater than 30 knot total horizontal wind change, with a corresponding false alarm probability of 14% [Weber, et. al. 1991]. Modification of an ASR to perform wind shear detection is a promising alternative for locations which do not warrant TDWR installations.

2.2.2 *Airborne Systems*

Airborne systems include *reactive* sensors, which alert the crew upon penetration of a microburst, and active and passive *forward-look* systems, which remotely sense microbursts ahead of the aircraft.

Reactive Sensors. Reactive sensors provide real-time measurements of the immediate windfield by differencing inertial measurements of aircraft state (linear accelerations, angular rates) with air data system measurements (airspeed, vertical speed). F-factor can be computed directly by reactive systems, since all relevant quantities (see Eqn. 2.4) can be directly measured. However, these systems can only reliably detect a microburst several seconds after the aircraft has entered it. If the microburst is severe enough, this may be too late for a successful recovery maneuver even if initiated immediately. Reactive wind shear alert systems are becoming standard equipment on transport-category aircraft, and certification requirements for both reactive sensors and microburst escape guidance systems have been set by the Federal Aviation Administration [FAA, 1990].

Active Forward-Look Sensors. There are several airborne forward-look microburst detection technologies in varying stages of development, but none of them have been deployed in the field as of this writing. Active forward-looking sensors include Doppler radar and Doppler lidar (laser radar) [Bowles, 1990]. These sensors measure the Doppler shift from reflected microwave or laser radiation to determine wind components radial to the sensor (usually aimed along the aircraft flight path). Since aircraft are usually flying horizontally or at small flight path angles, only the horizontal winds are measured, and the vertical winds ahead of the aircraft cannot be directly measured. However, algorithms have been developed to estimate vertical winds from horizontal wind shear and thereby allow estimation of F-factor for hazard assessment. [Bowles, 1990; Vicroy, 1992]. Airborne Doppler systems must overcome problems of

rain attenuation (due to their relatively low transmission power) and ground clutter (due to downward look angles) in order to become viable. During NASA flight tests performed in the summer of 1991, it was demonstrated that airborne Doppler radars can successfully detect microbursts without false alerts due to ground clutter [Bracalente, 1992]. Airborne Doppler radars with microburst detection capabilities are currently in the certification phase. Preliminary testing of a Doppler lidar was done by NASA in the summer of 1992, but results are not available as of this time.

Passive Forward-Look Sensors. Passive forward-looking sensors based on infrared (IR) radiometry are also under development [Adamson, 1988]. IR systems measure the temperature difference between the cool air descending in the microburst core and the local air temperature at the aircraft's current position. The difference in temperature has been correlated with peak F-factor in the microburst core through computational microburst simulations [Proctor, 1988; 1989]. Initial testing has shown some promise, but problems were encountered including false alerts caused by rain contamination of sensor measurements [McKissick, 1992]. IR systems are currently still in the development phase.

Although none of the forward-looking sensor systems are currently operational, flight tests of prototype IR, Doppler radar, and Doppler lidar have been done by NASA Langley Research Center in 1991 and 1992. Initial results are promising, but the analysis of flight test data is not complete as of this writing [Lewis, 1993].

2.3. Technologies for Alert Dissemination

VHF Radio. The only communication link presently available between ATC and aircraft for dissemination of wind shear alerts is standard VHF verbal radio communications. Using voice channels for alerts is problematic for several reasons. The high density of radio communications in busy terminal areas makes the addition of any

further transmissions, particularly time-critical ones, undesirable. In addition, requiring controllers to disseminate microburst alerts may result in unacceptably high controller workload levels. Also, the latency time due to controller involvement in the alert process may be detrimental to successful microburst avoidance. A few seconds of delay can have significant impact on the ability of aircraft to recover from microburst encounters [Hinton, 1990]. One possible solution is to employ a digital ground-air datalink and automate alert generation and delivery.

Mode-S Datalink. The FAA's Mode-S surveillance datalink is a promising candidate for digital uplink of hazardous weather information in the terminal area due to its ability to rapidly disseminate messages to individually selectable aircraft. Mode-S is an extension of the altitude encoding Mode-C transponder in the ATC Radar Beacon System allowing message delivery from ATC to individual aircraft. Each message can carry 48 useful bits of information, and the time for the interrogation beam to scan the entire coverage area ranges from 4 to 12 seconds. Messages can be also be linked in groups of up to 4 frames or sent as a longer Extended Length Message (ELM) with less urgency [Orlando, Drouhilet 1986]. Because ELMs can be delayed when the terminal area is crowded, it would be desirable to send time-critical microburst alerts in the standard 48-bit surveillance mode. This places a strong constraint on alert format length.

ACARS Datalink. The ARINC Communications Addressing and Reporting System (ACARS), a privately-sponsored VHF bi-directional digital datalink, is currently in use by many major airlines. It provides an alphanumeric datalink capability for flight management information such as uplink of destination weather or arrival gate information, or downlink of engine performance or winds aloft data. In addition, ACARS can now be used at some airports to receive pre-departure clearances from ATC and to program the aircraft's Flight Management Computer with the proposed route of

flight, winds aloft, and performance data [Midkiff and Hansman, 1992]. ACARS provides another possible channel for microburst alert dissemination.

2.4. Technologies for Alert Presentation

As mentioned above, VHF voice channels are the only currently available method for delivery of ground-generated microburst alerts. However, the advent of digital datalink will allow electronic presentation of ground-generated alerts to the flight crew. The Electronic Flight Instrumentation Systems (EFIS) in modern transport aircraft could be used both for this purpose and to present alerts from onboard sensor systems. An EFIS is a set of color cathode ray tube (CRT) displays or flat-screen liquid crystal displays (LCD) used to graphically or textually present information. An EFIS typically includes a Primary Flight Display (PFD) with the artificial horizon and altitude and airspeed information), an Electronic Horizontal Situation Indicator (EHSI) which provides a track-up "moving map" navigation display with programmed route and destination airport, and an engine and auxiliary systems display to allow the crew to monitor engine health and other onboard systems operation. In addition, weather radar precipitation returns can often be displayed directly on the EHSI.

The most likely modes of operation for microburst alerts would be either a graphical iconic display using the EHSI map display and/or a weather radar display, or a textual display on either the EHSI or PFD. These could be accompanied by discrete alert lamps and aural tones or recorded or synthetic voice. The use of these displays is subject to many constraints, and formats must be carefully designed to minimize added crew workload and maximize crew situational awareness. These topics will be further discussed in Chapter 4.

2.5. Current Alert and Response Procedures

2.5.1. The Windshear Training Aid

Current operational procedures for microburst detection and alerting are based on the FAA's Windshear Training Aid [1987]. The Windshear Training Aid (WTA) was written to inform pilots, controllers, and airline management about wind shear, and it emphasizes early recognition and avoidance techniques. WTA microburst avoidance procedures are predicated on the *absence* of an accurate quantitative microburst detection capability such as TDWR which can reliably alert prior to microburst penetration. In order to evaluate the need for avoidance, the probability of microburst presence is evaluated from LLWAS alerts, weather reports, and visual clues as outlined in Table 2.2. Wind shear clues from this table are to be considered cumulative, such that two indications of MEDIUM probability should be taken to indicate a HIGH probability. It should be noted that high pilot workload in the terminal area and the relative rarity of hazardous wind shear makes it difficult for even well-trained crews to fully assimilate the evidence of wind shear before penetration.

Table 2.2. Microburst Windshear Probability Guidelines. Redrawn from the *Windshear Training Aid* [FAA, 1987].

Observation	Probability of Windshear
PRESENCE OF CONVECTIVE WEATHER NEAR INTENDED FLIGHT PATH:	
• With localized strong winds (Tower reports or observed blowing dust, rings of dust, tornado like features, etc.	HIGH
• With heavy precipitation (Observed or radar indications of contour, red, or attenuation shadow)	HIGH
• With rainshower	MEDIUM
• With virga	MEDIUM
• With moderate or greater turbulence (reported or radar indications)	MEDIUM
• With temperature/dew point spread between 30°F and 50°F	MEDIUM
ONBOARD WINDSHEAR DETECTION SYSTEM ALERT (Reported or observed)	HIGH
PIREP OF AIRSPEED LOSS OR GAIN:	
• 15 knots or greater	HIGH
• Less than 15 knots	MEDIUM
LLWAS ALERT/WIND VELOCITY CHANGE:	
• 20 knots or greater	HIGH
• Less than 20 knots	MEDIUM
FORECAST OF CONVECTIVE WEATHER:	LOW

NOTE: These guidelines apply to operations in the airport vicinity (within 3 miles of the point of takeoff or landing along the intended flight path and below 1000 feet AGL). The clues should be considered cumulative. If more than one is observed the probability weighting should be increased. The hazard increases with proximity to the convective weather. Weather assessment should be made continuously.

CAUTION: CURRENTLY NO QUANTITATIVE MEANS EXISTS FOR DETERMINING THE PRESENCE OR INTENSITY OF MICROBURST WINDSHEAR. PILOTS ARE URGED TO EXERCISE CAUTION IN DETERMINING A COURSE OF ACTION.

HIGH Probability indicates that critical attention need be given to this observation. A decision to avoid (e.g. divert or delay) is appropriate. MEDIUM Probability indicates that consideration should be given to avoiding. Precautions are appropriate. LOW probability indicates that consideration should be given to this observation, but a decision to avoid is not generally indicated.

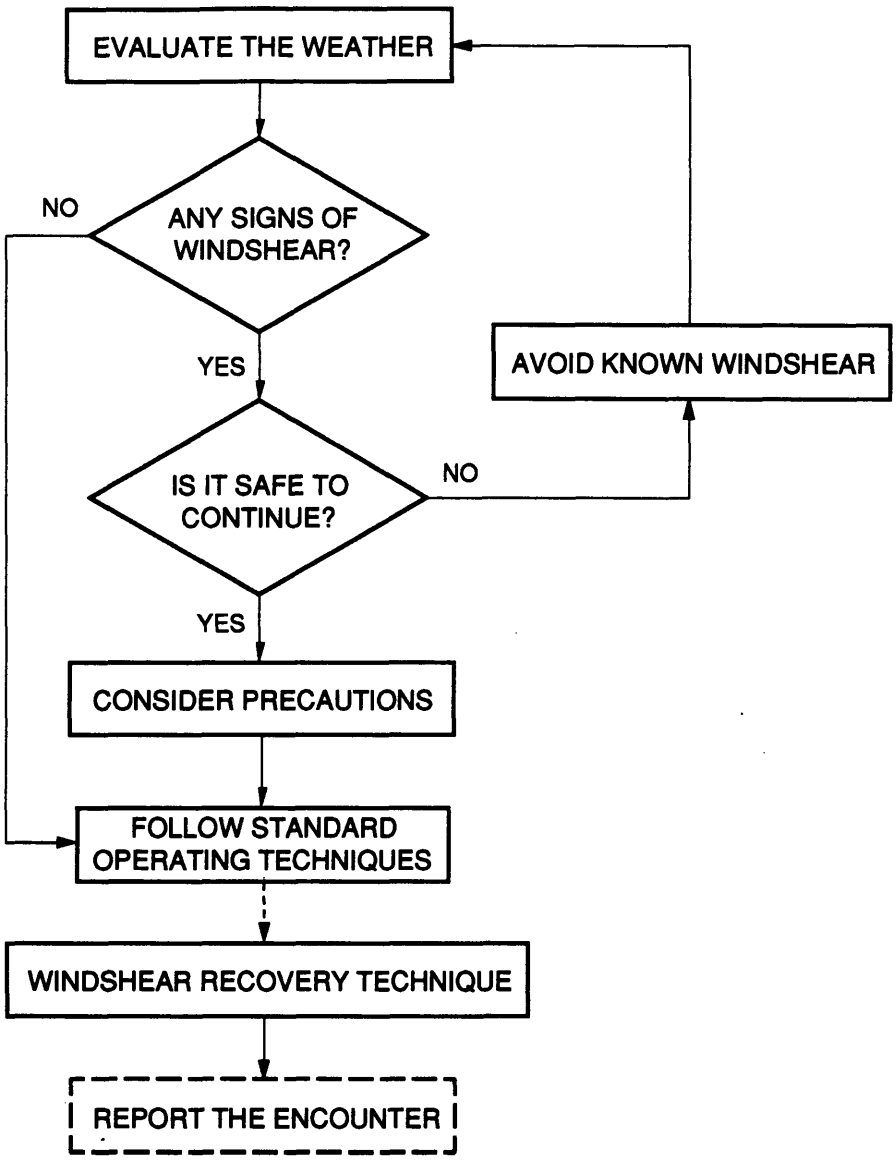

Figure 2.3. Model of Flight Crew Actions. Redrawn from the *Windshear Training Aid* [FAA, 1987].

The WTA also provides a model of flight crew actions (Figure 2.3) to use with the probability guidelines. This model is intended to simplify and expedite operational wind shear decisions for the pilot. Although the general policy followed in the WTA is to avoid areas of known wind shear, situations may arise where microburst penetration is unavoidable and recovery maneuvers are required. The WTA outlines a recovery procedure involving application of maximum thrust and maintenance of a constant pitch angle (typically 15°), and establishes conditions under which a recovery should be

initiated. The effectiveness of this procedure has been addressed by several investigators including Hinton [1989, 1990] and Mulgund and Stengel [1992]. The technique yields reasonable results given its simplicity. Hinton concluded that a difference of only 5 seconds in recovery maneuver initiation time has more impact on aircraft survival than the difference between use of several candidate recovery techniques. This strongly emphasized the need for rapid microburst recognition and forward-look microburst detection.

The last item on the model of flight crew actions (Figure 2.3), "Report the Encounter," is critical. Pilot reports (PIREPs) of wind shear may provide the only conclusive advance warning of microburst presence given the current state of microburst sensor system deployment. During a multiple-microburst event which occurred at Denver Stapleton Airport on July 11, 1988 five aircraft made missed approaches due to microbursts. None of them issued a PIREP or advised the tower of their reasons for making the missed approach, because of high pilot workload. Therefore, this data was not relayed to subsequent aircraft [Schlickenmaier, 1989]. A PIREP from one of the first aircraft to abort would clearly have been useful for alerting subsequent aircraft, one of which descended to less than 100 feet AGL approximately one mile short of the touchdown zone. All of the flight crews involved had been trained using the Windshear Training Aid.

2.5.2. The TDWR/LLWAS system

At airports with prototype TDWR installations, microburst alerting is more formalized. TDWR generates new microburst products at one minute intervals, and these products are presented in the control tower both as icons on a Geographical Situation Display (GSD) (Figure 2.4) and as formal alerts on an alphanumeric display. These procedures were developed during TDWR operational evaluations at Denver, Kansas City, and Orlando over the past several years.

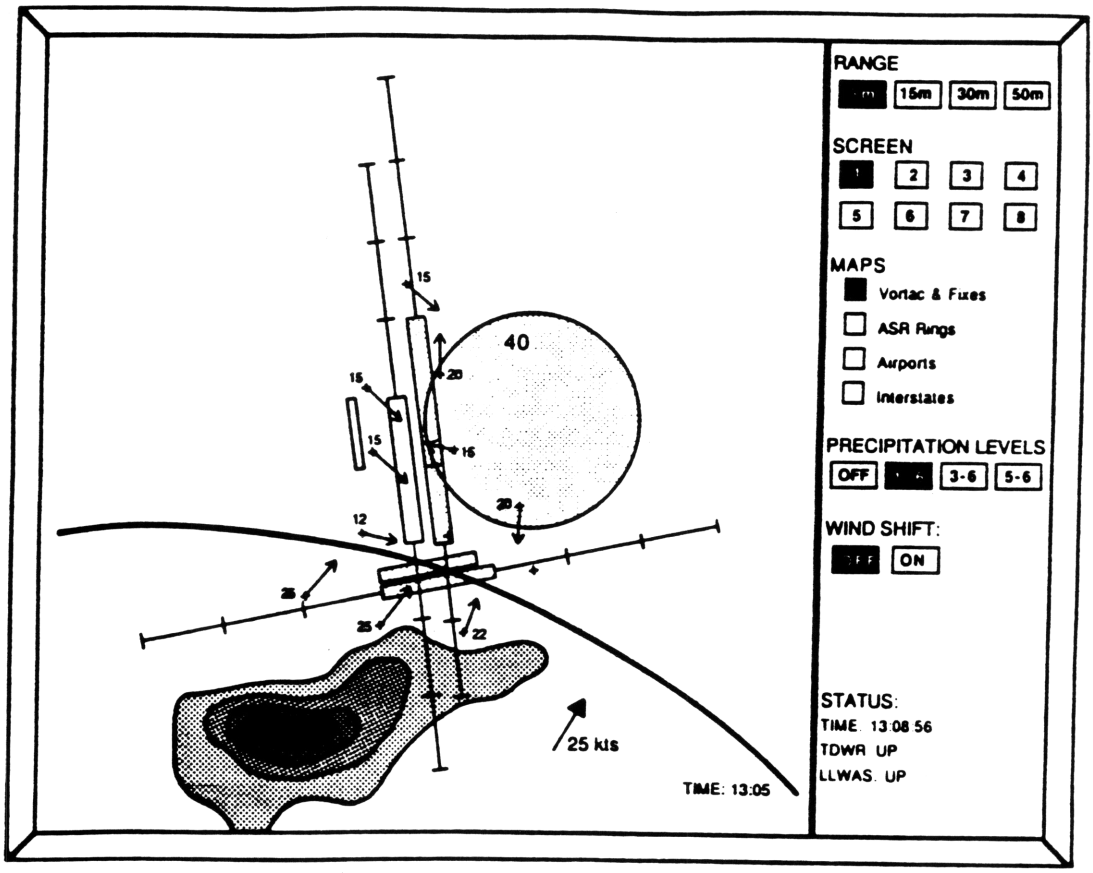

Figure 2.4. Schematic View of TDWR Geographical Situation Display (GSD). The GSD is a color display in the control tower. Microburst regions appear as solid red circles or bandaid shapes labeled with the horizontal windspeed change. Gustfronts, LLWAS wind vectors, and six-level radar reflectivity can also be displayed. Reproduced from [NCAR, 1988].

Surface microbursts are detected by identifying regions of velocity divergence; if the detected wind component radial to the radar shows a steady rapid increase with range, a surface outflow is present and a "shear segment" is scored. Definite groups of these segments are "boxed" by the processing algorithm, subjected to tests for significant strength and size, and identified as microburst regions. These regions are displayed as red circles or "band-aid" shapes on the GSD, and labeled by the maximum measured wind change within each shape [Merritt, et. al., 1989].

An initial alerting methodology based on these shapes was determined by a TDWR/LLWAS User Working Group of pilots, air traffic controllers, FAA officials, researchers, and others. [NCAR, 1988; Sand and Biter, 1989] The resulting criterion for

microburst alerts is illustrated in Figure 2.5, and applies to both TDWR and improved LLWAS systems. The "wind shear warning boxes" in the figure were defined by the Working Group based on the assumption that aircraft below 1000 ft AGL in landing or take-off configuration are most susceptible to wind shear. The boxes are 1 nm squares extending 3 nm from the runway landing threshold, 2 nm from the departure end of the runway, and directly over the runway. A microburst event of measured horizontal wind change greater than 30 knots which impacts any part of these boxes triggers a microburst alert. Events of 20 to 30 knots wind change trigger a "wind shear with loss" alert. This alert is radioed to the pilot as he contacts the tower for final approach, since the alert displays are currently only available to the tower controller.

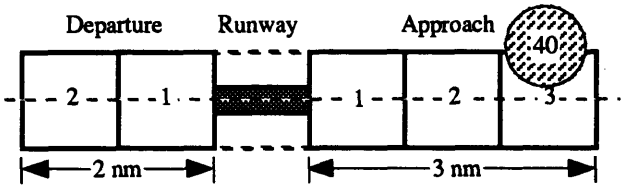

The alert corresponding to the 40 knot microburst pictured above might be:"United two two six, Denver tower, threshold wind one six zero at six, expect a four zero knot loss on three mile final."

Figure 2.5. TDWR/LLWAS microburst alerting corridor

The verbal message to be relayed from the controller to the pilot is presented on an alphanumeric "ribbon" display in the control tower (Figure 2.6). The display includes one line for each approach and departure runway and the corresponding wind shear status. The source of the information (TDWR, LLWAS, or both) is transparent to the controller and the alerting procedure is identical in all cases.

The July 11, 1988 microburst event mentioned above was the first major microburst event to endanger aircraft which occurred under documented TDWR coverage. As such, it provided invaluable information on potential problems with the proposed ground-based microburst alert strategy. For example, the TDWR microburst alerts were given verbally by the tower controller embedded in a standard "cleared to land" message. As a result, four of five aircraft to whom the alert was issued elected to

Type of wind shear	Runway	Threshold winds	Wind shear Headwind change (kts)	Location
	CF	190 16 G 25		
MBA	35 LD	160 22	50-	RWY
MBA	35 RD	180 5	25-	RWY
MBA	35 LA	030 23	55-	1 MF
	35 RA	180 10	60-	3 MF
MBA	17 LA	180 5	25-	RWY
MBA	17 RA	160 22	55-	RWY
	17 LD	180 10	60-	RWY
MBA	17 RD	030 23	55-	RWY

Figure 2.6. Example of alphanumeric ribbon display for TDWR and LLWAS alerts. For an aircraft arriving on Runway 35 Left (35 LA) the message is "United two-two-six, microburst alert, threshold wind zero-three-zero at two-three, five-five knot loss, one mile final, centerfield wind one-nine-zero at one-six, gust two-five." Redrawn from [NCAR, 1988].

continue the approach and did in fact encounter dangerous wind shear conditions. This event has been extensively documented by Schlickenmaier [1989] and its implications for alerting procedures were discussed by Wanke and Hansman [1989; 1990].

The TDWR operational evaluations also provided valuable data on the importance of issuing accurate warnings. During the 1988 TDWR Operational Evaluation, data was collected from 111 pilots who landed or took off during alert periods. Of this group, 34% indicated that nothing was encountered, and 31% reported that nothing much was encountered. These cases have been termed "nuisance alerts" since the TDWR did in fact report an actual microburst, but it simply did not affect the alerted aircraft. A nuisance alarm rate this high can unnecessarily disrupt airport operations and damage pilot confidence in the alerting system.

The reasons for this high nuisance alert rate have been studied by Wanke and Hansman [1990]. One reason is that a microburst which impinges on the edge of the alerting corridor is called out in the same way as a microburst located directly on the approach/takeoff path (Figure 2.7). Due to the localized nature of microbursts, a microburst which is laterally offset in this way may have little or no effect on an approaching or departing aircraft. This was demonstrated using computationally-

modeled microburst windfields by Wanke and Hansman [1990]. A correction technique for this deficiency is being developed and has undergone testing in recent TDWR operational evaluations [get a reference on shear integration].

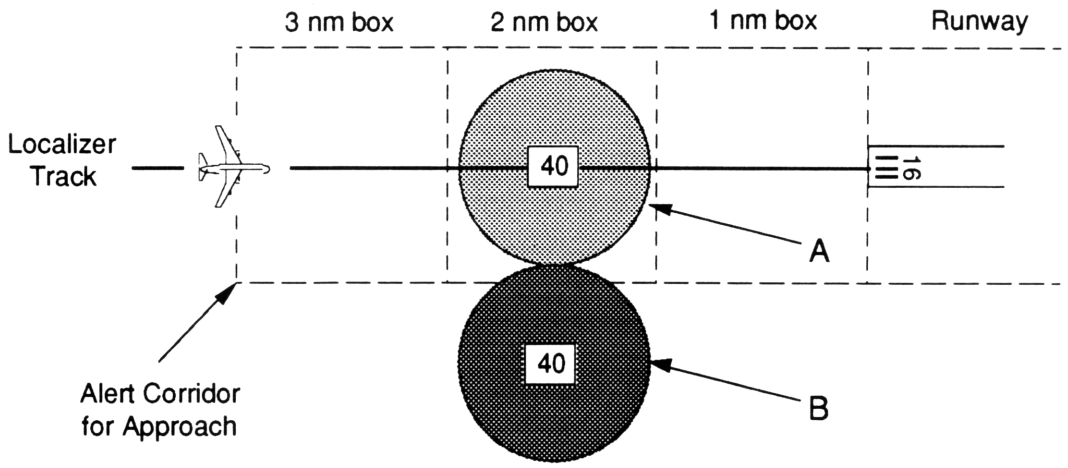

Figure 2.7. Lateral displacement example. The two microbursts A and B shown in this example would generate the same alert: "... expect a four zero knot loss on two mile final."

Another contributing factor to overwarning is that measured maximum velocity change is used to quantify microburst strength. The alert format implies that this velocity change should be interpreted as the airspeed loss which would be experienced by an aircraft penetrating the microburst. In reality, the aircraft would experience an initial airspeed gain followed by a (greater) airspeed loss. In addition, the amplitude of the airspeed disturbance is highly dependent on the aircraft dynamics and the control strategy which is used by the pilot or autopilot. Further discussion of these and several other possible causes of overwarning is given by Wanke and Hansman [1990; 1992b].

2.6. Future Microburst Alerting Systems

In the early 1990's, ground-based doppler radars, along with existing and improved LLWAS installations, will be the primary sources of advance microburst alert data. This data will be supplemented by onboard reactive wind shear alert systems, PIREPs, and eventually airborne forward-look sensors when they are certified and deployed. Digital datalink systems, in particular Mode-S, are nearing the operational

stage and will provide new channels for microburst alert dissemination. Also, the availability of digital datalink may make "automated PIREPs" possible. Data from airborne reactive and/or forward-look sensors could be transmitted directly to the ground without need for pilot intervention. Finally, the deployment of EFIS on transport-category aircraft provides numerous options for effective presentation of microburst alerts to the flight crew.

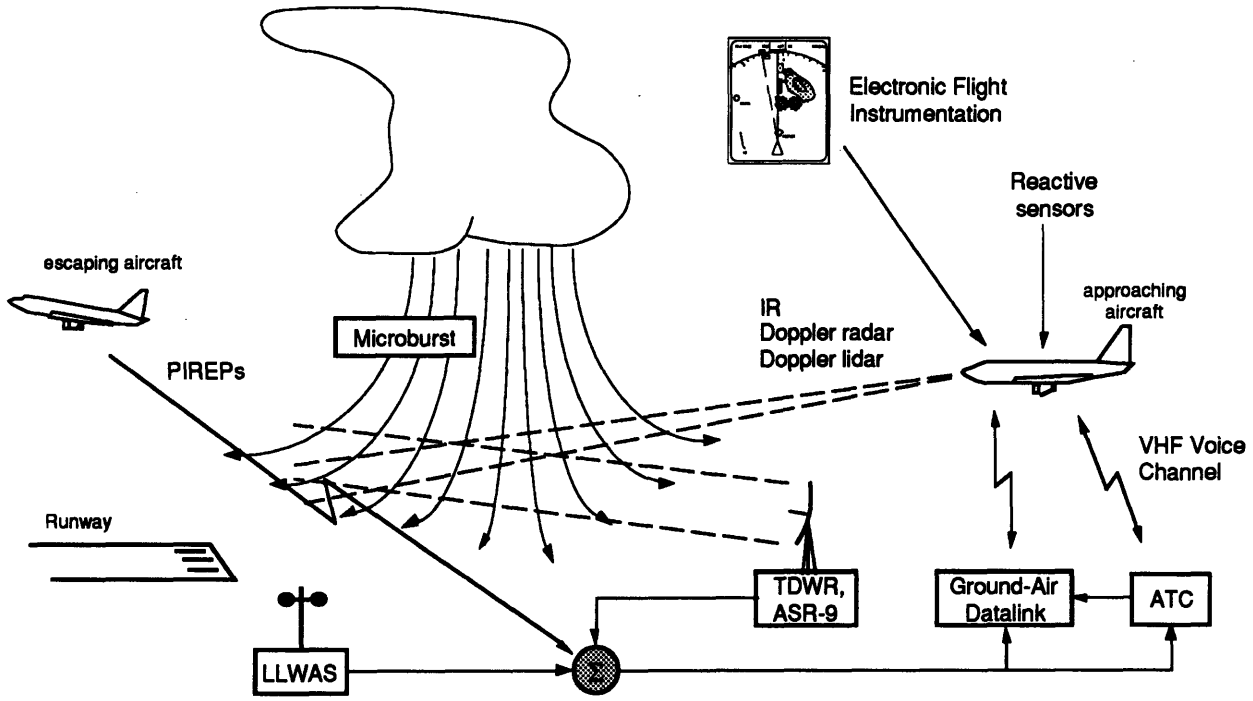

Figure 2.8. Advanced microburst detection and alerting system options.

This rapid technological expansion, illustrated in Figure 2.8, clearly has strong potential for reducing the microburst threat. Effective use of this potential requires significant study, and is the basis for work which follows. In the next chapter, the integrated microburst alert system design task is discussed.

3. Microburst Alerting System Design Issues

3.1 Problem Definition

The mission of a microburst alerting system is to detect, locate, and evaluate the hazard to aviation from microbursts in order to: (1) allow aircraft to avoid hazardous microbursts where possible, and (2) aid in recovery from unavoidable microburst encounters. This mission should be accomplished while minimizing to the extent possible: (1) additional pilot and controller workload, (2) detrimental impact on airport operational efficiency, and (3) cost. The work presented in this report is principally concerned with near-term systems, thus limiting the available resources for system development to those discussed in Chapter 2.

3.2 Alerting Task Breakdown

3.2.1 High-Level Task Breakdown

Figure 3.1 illustrates a high-level breakdown of the overall microburst alerting process. There are three primary tasks: Measurement, Alert generation, and Alert application. The Measurement task begins with collection of data from one or several possible ground-based and airborne sources. These measurements are then assimilated to detect microbursts and estimate important characteristics of detected microbursts. The characteristics are passed to the Alert generation task, which has two parts. The first is to evaluate the aviation hazard posed by the microburst. The second part is to produce alerts based on the results of the hazard evaluation and on the current operational situation. Finally, in the Alert application task, alerts are formatted, disseminated and presented to end users, who take appropriate action based on a set of specified procedures. In the following sections, these tasks are addressed in more detail, and examples of each task are given in the context of current and near-term microburst alerting systems.

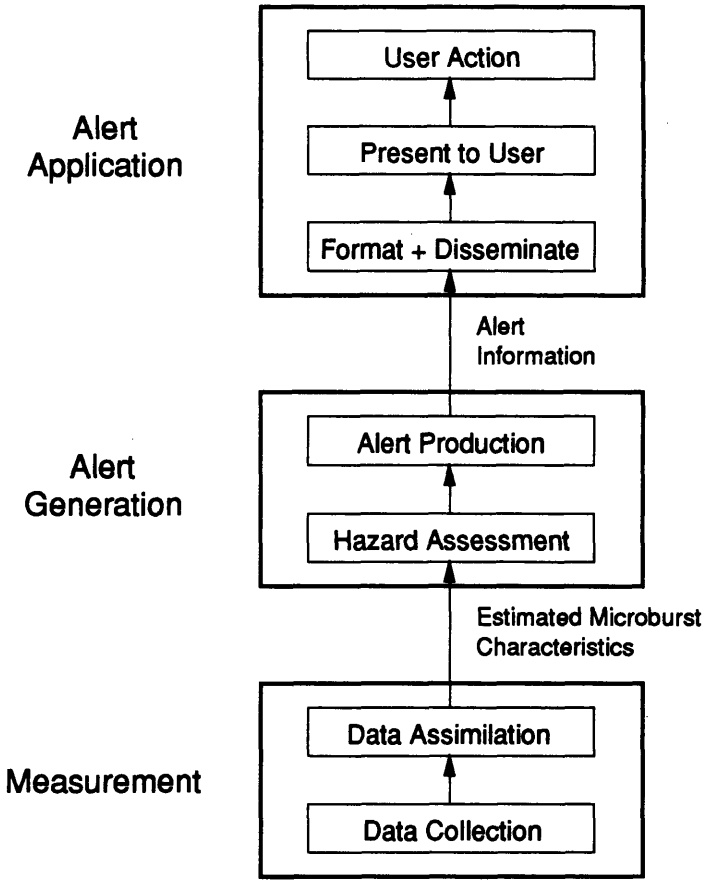

Figure 3.1. Microburst Alerting Task Breakdown

3.2.2 Measurement

The microburst measurement task is complex, since there is a wide array of microburst sensors with differing measurement characteristics. Most importantly, the measured quantity varies between sensors. For example, Doppler sensors measure radial wind components over a large area, LLWAS measures two-dimenstional winds at discrete points, and IR sensors measure ambient air temperature differences ahead of the aircraft. Other varying sensor characteristics include range, resolution, coverage volume, accuracy, and update frequency. An additional complication is that the sensors can be located either on the ground or on one or more aircraft in the terminal area.

Figure 3.2 is a pictorial representation of possible measurement task elements and information flow paths. In addition to atmospheric measurements, flight crew observations and pilot reports (PIREPs) provide useful data. Data can either be assimilated on the sensor platform itself (ground station or aircraft) or combined with data from other sensor platforms prior to assimilation. The results of data assimilation are estimated microburst characteristics. Possible microburst characteristics include strength, location, spatial extent (radius), temperature drop in the core, and advection speed. When multiple sensors are available, the assimilation process can in principle "fuse" data from different sensor systems to produce improved estimates.

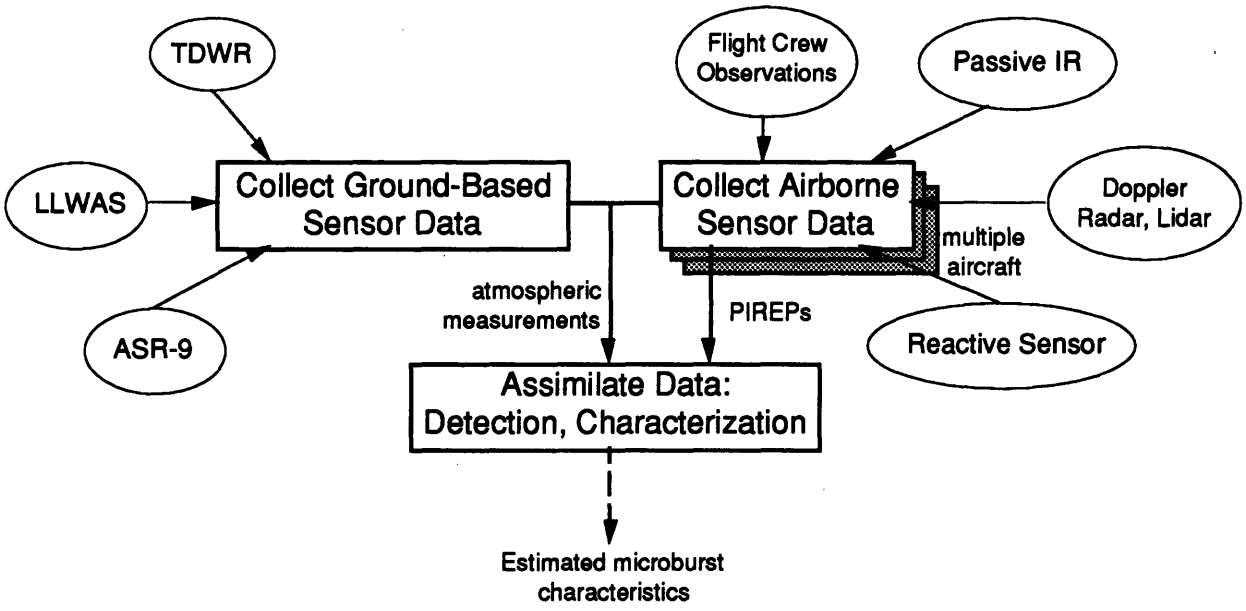

Figure 3.2. Measurement and Assimilation Task

3.2.3 Alert Generation

The alert generation task begins with hazard assessment. The aviation hazard posed by a microburst is evaluated from the estimated microburst characteristics using a suitable "hazard criterion," which will be further discussed in Chapter 6. The resulting hazard value is usually indicative of the aviation hazard for a worst-case scenario, in

which an approaching or departing aircraft penetrates the most threatening part of the microburst.

Alerting criteria are then applied to determine if an alert is necessary and what level of alert to issue. The alerting criteria typically consider the hazard value and the microburst location relative to the runway or to the affected aircraft. Other operational data such as aircraft performance capabilities and the current locations of affected aircraft may also be considered.

3.2.4 Alert Application

The first part of the alert application task is to format and disseminate alerts to end users, including ATC and/or flight crews of affected aircraft. If ground-air transmission is required, either ATC voice channels (as in current practice) or digital datalinks may be employed. The received alerts may be presented to flight crews and ATC in a variety of ways including verbal messages, discrete panel lights, and electronic display of text or graphical symbols. Finally, ATC and the affected flight crews decide on appropriate actions to take. A fairly general decision tree for flight crew actions was given in Figure 2.3. For ATC, possible actions include runway reconfiguration or even airport closure.

Figure 3.3 illustrates several possible structures for the alert application process. The current TDWR and LLWAS systems follow route A in the diagram, in which alerts and PIREPs reach the aircraft via standard VHF radio communications. Future ground-based systems may uplink alerts directly from the alert generation hardware to the aircraft instrumentation for display (route B). Alerts generated by airborne systems are presented directly to the flight crew (route C). This information could then reach ATC by one of two routes: by a formal pilot report over VHF radio link as in current practice (route D), or by digital datalink as an automated report (route E).

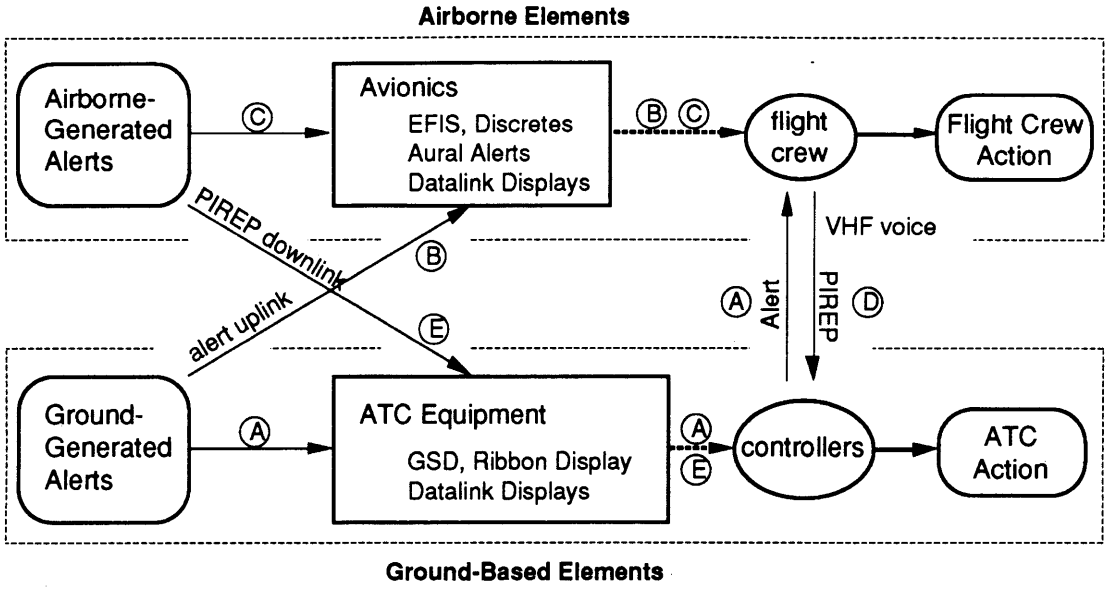

Figure 3.3. Possible structures for the alert application task. The circled letters indicate the possible routes of information flow described in the preceding paragraph.

3.3 Task Breakdown Examples

It is illustrative to examine the microburst task breakdown in the context of current and near-term microburst alerting capabilities. The following example microburst alert system implementations will be discussed:

Terminal Doppler Weather Radar. The prototype TDWR alerting system as it is currently implemented for operational evaluations.

Unaided airborne alerting. Standard airborne alerting procedures in the absence of a quantitative microburst detection capability, as discussed in the Windshear Training Aid.

Airborne predictive alert system. An automated airborne alerting system using a forward-look microburst sensor.

3.3.1 Terminal Doppler Weather Radar

Measurement. In the TDWR system, radial wind velocity measurements are collected. This data is assimilated in two steps: (1) Regions of radial shear or "shear segments" are identified, and (2) groups of shear segments are enclosed by shapes, which are labeled by the maximum velocity change measured within the shape. An example of

a multi-sensor data assimilation process is the prototype TDWR-LLWAS integration algorithm, in which TDWR shapes are combined with similar shapes generated from LLWAS wind data to improve the estimated microburst characteristics [Cornman and Mahoney, 1991].

Alert Generation. The prototype TDWR system uses maximum horizontal velocity change ("delta-V") as a hazard criterion. Both the hazard level and the microburst position are considered when producing alerts. As described in Chapter 2, alerts are issued when microbursts impinge on "alerting boxes" associated with active runways, and only to aircraft currently on final approach or preparing for takeoff. This alert may be a "wind shear with loss" (20 knots ≤ delta-V < 30 knots) or a "microburst alert" (delta-V ≥ 30 knots).

Alert Application. TDWR alerts are disseminated and applied along route A in Figure 3.3. Alerts are presented to air traffic controllers both graphically on the GSD (Figure 2.4) and as text on a ribbon display (Figure 2.6). Information on the ribbon display is verbally disseminated to approaching and departing aircraft via standard VHF radio communications procedures. The pilot then decides either to avoid the microburst (abort the approach, delay takeoff) or continue normal operations with suitable precautions.

3.3.2 Unaided Airborne Alerting

Measurement. The standard airborne alerting measurement process is much different than that used by TDWR. Flight crews collect visual information, onboard sensor data (such as weather radar returns, airspeed variations, trim thrust setting), and possibly PIREPs through the air traffic controller. The assimilation task, done by the flight crew, is to detect evidence of microbursts in this data, and if detected to estimate microburst position and strength.

Alert Generation. The hazard evaluation is conceptually achieved by a review of the wind shear indicators described in Table 2.2, which can be viewed as a list of hazard criteria. The hazard evaluation process is the identification of LOW, MEDIUM and HIGH risk factors based on data assimilated by the crew. The final "alert" is produced when the flight crew combines this rating with knowledge of the current aircraft position and configuration. Note that this procedure is internalized by the flight crew as a result of training, and thus in practice actual "risk ratings" are subjective and are not necessarily arrived at in the above formalized fashion.

Alert Application. For unaided airborne alerting, no dissemination or presentation is required other than intra-cockpit communication among the flight crew. As when receiving TDWR alerts, the crew decides either to continue normal operations or to initiate microburst avoidance or recovery procedures. An avoidance or recovery maneuver should be followed by a pilot report.

3.3.3 Airborne Predictive Alerting System

Measurement. In an airborne system based on a forward-looking (predictive) sensor, atmospheric measurements ahead of the aircraft would be collected. These would then be assimilated using an onboard computer which would identify potential microburst regions based on shear measurements (for Doppler systems) or temperature changes (for IR systems). All processing would be accomplished onboard the aircraft.

Alert Generation. In automated airborne forward-look systems, it is most likely that averaged F-factor would be the hazard criterion. This will be further discussed in Chapter 6. Approximate formulas have been developed to estimate F from shear and temperature measurements [Bowles, 1990]. Alerts would be produced when a microburst is detected which (1) surpasses a preset F-factor threshold, and (2) is on or very near to

the aircraft's projected flight path. Again, all processes would be accomplished onboard the aircraft.

Alert Application. Alerts would be formatted, disseminated, and presented to the flight crew by onboard avionics systems (route C, Figure 3.3). Alerts can be presented by a variety of means, including aural tones, synthetic voice, discrete panel indicators, or on the EFIS.

3.4 Research Overview

3.4.1 The User-Centered Design Approach

The Measurement, Alert Generation, and Alert Application tasks could be accomplished in several different ways. Consequently, there are many important issues and tradeoffs to be resolved in the development of advanced microburst alerting systems. In this work a user-centered approach has been employed to isolate and address several of the more critical system design issues. The user-centered approach led to a "top-down" analysis technique, beginning with alert application issues. The results of each study established the requirements for the next, and the process propagated downward until the measurement task was addressed.

For microburst alerting, the primary end user is the flight crew. Therefore, the initial step was to attempt to determine the information required for effective microburst alerting and the most effective presentation techniques for this information. In addition, the effect of new microburst alert formats on recommended crew actions was studied. These issues relate to the alert application task, and were approached under the assumption that accurate, timely alerts could be produced.

Next, the issue of producing the required alert information - the alert generation task - was addressed, assuming that microbursts could be detected and their

characteristics accurately estimated. This work centered on the selection of an appropriate microburst hazard criterion and use of this criterion to establish an effective multi-level alert structure.

Once the requirements for effective multi-level alerting were established, the problem of accurately estimating microburst characteristics was investigated. This study was predicated on a multi-sensor measurement environment such as the one illustrated in Figure 3.2.

3.4.2 Overview of Design Studies

The specific studies which were undertaken are introduced below, categorized by the three major microburst alerting tasks illustrated in Figure 3.1.

Alert application issues were addressed in three separate studies.

- Terminal Area Wind Shear Survey. This survey was conducted to obtain pilot input on (1) the usefulness of currently available data for wind shear avoidance, and (2) requirements for new wind shear alerting systems.
- Comparison of Cockpit Presentation Modes. When digital datalinks become operational, it will be possible for ground-generated microburst alerts to be disseminated over voice channels, displayed as an alphanumeric (text) message, and/or depicted graphically on electronic flight instrumentation systems (EFIS). A piloted part-task flight simulator experiment was conducted to compare the relative efficiency of these *verbal, textual,* and *graphical* presentation modes.
- Evaluation of Candidate Graphical Microburst Alerting Displays. A piloted part-task simulator experiment was conducted to address issues specifically related to the graphical display of microburst alerts on electronic cockpit instrumentation.

The microburst *alert generation* task was addressed through two studies.

- Comparison of Possible Hazard Criteria. A methodology for evaluating microburst hazard criteria was developed based on batch flight simulation. It was

used to compare several candidate hazard criteria for jet transports on final approach and takeoff.

- Selection of Hazard Thresholds for Alert Generation. A technique was developed for determination of hazard threshold values to be used for generating multi-level microburst alerts. The technique was applied to a three-level alert strategy for jet transports on final approach.

Measurement data assimilation in a multi-sensor environment was also addressed.

- A Model-Based Algorithm for Multi-Sensor Estimation of Microburst Characteristics. A technique was developed and tested which can improve estimates of microburst characteristics using one or several data sources without incurring prohibitively large computational or data transmission requirements. A simple analytical microburst model is used to approximate the actual windfield, and a "best" set of model parameters are estimated from measured winds using an extended Kalman filtering technique.

4. Terminal Area Wind Shear Survey

4.1. Objectives

A pilot opinion survey (included in Appendix A) was developed to obtain input on the usefulness of currently available data for wind shear avoidance, and on desirable characteristics of new wind shear alerting systems. More specifically, the survey addressed the following areas:

1) User assessment of current wind shear alerting procedures.
2) User confidence in currently available wind shear alerting information.
3) Desired information content of advanced wind shear alerts.
4) Desired presentation and timing of advanced wind shear alerts.

4.2 Survey Respondents

The survey was distributed in 1988 to 250 active United Airlines (UAL) pilots of Boeing 757, 767, 747-400, and 737-300 aircraft. Each of these aircraft types is equipped with an Electronic Flight Instrumentation System (EFIS) and a Flight Management Computer (FMC). 51 of the pilots responded. The important survey results are presented below; the results are presented in full detail in [Wanke, 1990].

Of the respondents, 51% have had what they considered to be a hazardous wind shear encounter. This percentage is higher than expected, since microburst encounters are quite rare. Based on statistics from microburst field studies, Stratton [1992] estimated that the probability of encountering hazardous wind shear in the U.S. was one encounter per 22,000 terminal operations. However, most of the encounters described by the survey respondents occurred at Denver-Stapleton airport, a UAL hub and an area noted for heavy microburst activity during the summer months. In addition, pilots who have had a

hazardous wind shear encounter may have been more likely to respond to the survey, so there may be some bias in the results.

4.3. Currently Available Wind Shear Alert Information

The first section of the survey was designed to examine general attitudes about microbursts and currently available wind shear alert information. The following findings were obtained:

- Most of the pilots (90%) agreed that "Microbursts pose a major safety hazard to transport category aircraft."
- Only 15% of the respondents agreed that "Currently available wind shear alert data is sufficient for safe operation in the terminal area," while 44% disagreed.
- *All but one* (98%) of the pilots felt that "a system to provide aircrews with better and more timely wind shear alerts is necessary."

These responses clearly indicate that pilots are dissatisfied with current wind shear alert data and would be receptive to improvements. The pilots were asked to rank the usefulness of four currently available wind shear data sources (Figure 4.1). Both pilot reports (PIREPs) and visual clues were found to be more useful for wind shear avoidance than the Low Level Windshear Alert System (LLWAS). However, neither PIREPs or

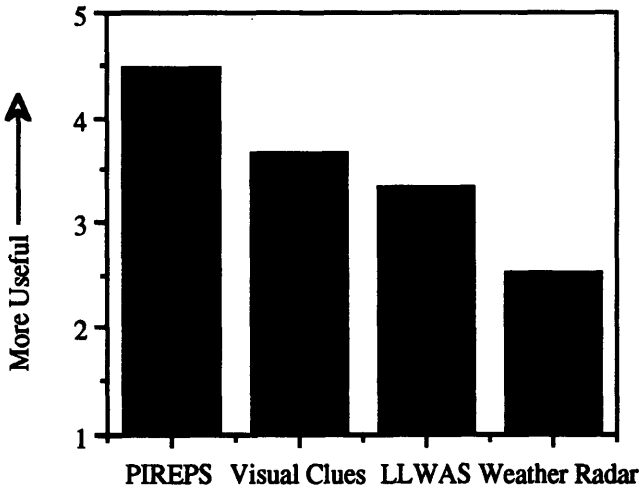

Figure 4.1. Mean pilot ranking of wind shear information sources

visual information are always available. These results illustrate the need for improved wind shear detection and alerting systems.

The importance of good PIREP collection and distribution was stressed by pilot comments:

> "The best real time data comes from pilot reports to tower controllers (ATC) to subsequent flights. The biggest drawback to this system is the workload on the controllers and more radio traffic."
>
> "Info is available at times, but is not provided to the stream of aircraft that is segmented on separate frequencies. Too many times an early encounter is not passed on to following aircraft in a timely manner."

4.4. Future Wind Shear Alerting Systems

The second section of the survey focussed on options for future wind shear alert system implementation. Pilots were asked to rank five possible cockpit presentation modes for ground-generated microburst alerts from most preferable to least preferable. Figure 4.2 presents the mean rankings, inverted so that 5 indicates most preferable while 1 indicates least preferable. Responses indicated that pilots are receptive to graphic displays. The specific suggestion of integrating wind shear information with an EFIS moving map display was strongly supported with a mean ranking of 4.3. Also of interest was the high preference for alerts issued verbally by ATC (mean ranking of 3.9), which is likely a result of familiarity with current standard radio procedures. Display of wind shear alerts on an alternate graphical display was also ranked above alphanumeric displays and ATIS*. Comments indicated that the low ranking of ATIS was primarily due to the long time between updates. The ATIS system would need to be changed significantly to achieve the timeliness required for microburst alerts.

* The ATIS (Automatic Terminal Information Service) is a continuous radio broadcast of airport weather conditions and other non-control information in selected terminal areas.

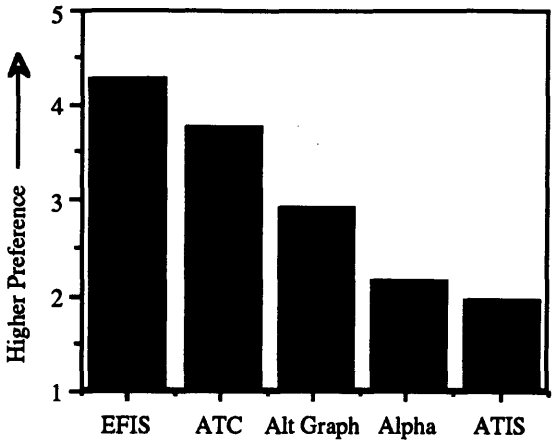

Figure 4.2. Mean pilot rankings of possible relay/presentation modes for ground-generated alerts

Pilots were also asked to rank six possible microburst alert information elements. Since the length of digital datalink messages is limited, identification of the most important information elements is necessary. The responses (Figure 4.3) indicated that location and intensity of microbursts are clearly the most important information items. Size, microburst movement, and intensity trends are of secondary importance, and shape data is generally felt to be least important. Ranking of this information is useful for design of alerts which fit within message length constraints and still retain enough

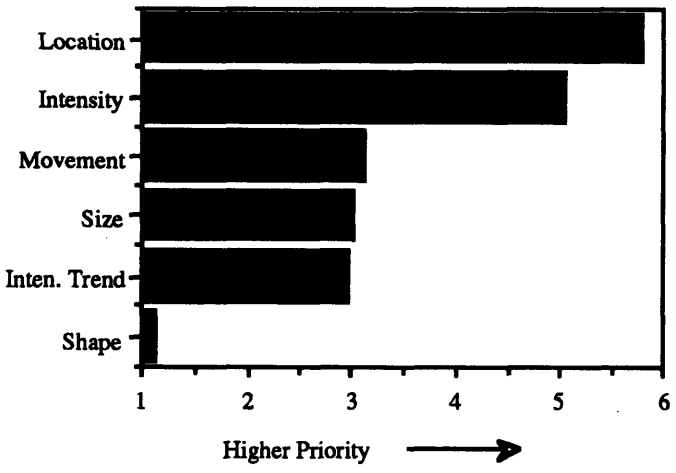

Figure 4.3. Mean pilot rankings of microburst information by importance

information to be useful. In this case, the data indicates that the message should include at a minimum location and intensity, and that movement, size, and intensity trend information may also be useful.

4.5. Summary of Survey Results

The survey results which were directly applicable to microburst alert system design are summarized below.

1) Pilots believe that currently available microburst alert information is inadequate for safe operation in the terminal area.

2) PIREPS of wind shear are valued highly, and considered the best currently available source of wind shear warnings. PIREP collection and distribution needs to be considered carefully in future system development.

3) Pilots are receptive to graphically-presented alerts, but showed little enthusiasm for alphanumerically-presented alerts.

4) Pilots identified microburst location and intensity as the primary alert information elements. Microburst movement, size, and intensity trends were considered less important.

Points 3 and 4 were explored further in the part-task simulation studies described in the next chapter.

5. Piloted Part-Task Simulator Studies

5.1. Overview

The terminal area wind shear survey provided initial user input for alert design. Additional user input under more controlled conditions was obtained through piloted simulation. This work focused on the effect of microburst alert format and presentation on the pilot's decision-making process. Since the primary area of interest was pilot decision-making (the "outer loop") rather than flying performance (the "inner loop"), a part-task simulation approach was chosen.

A part-task advanced cockpit simulation facility was developed for this purpose, and two experiments were performed. The first was a Comparative Study of Cockpit Presentation Modes, in which it was found that the graphically presented microburst alerts had important advantages over textually or verbally presented alerts. Consequently, an Experimental Evaluation of Graphical Microburst Alert Displays was done, in which specific graphical alert format issues were addressed and procedural implications of using a graphical alert presentation were identified.

The part-task simulation approach was found to be very useful, and has been used to study several other cockpit display and information transfer issues in addition to microburst alerting. Therefore, Section 5.2 gives a detailed description of the design and capabilities of the simulation facility. Section 5.3 describes the presentation mode comparison experiment, and Section 5.4 documents the graphical microburst alert format experiment.

5.2. The MIT Advanced Cockpit Simulator

5.2.1 Motivation

The implementation of advanced technology has significantly changed the cockpit environment in current "glass cockpit" aircraft. Recent developments in display technology, on-board processing, data storage, and datalinked communications are likely to further alter the environment in second and third generation "glass cockpit" aircraft. It is important that these technologies be implemented in a manner which will enhance both human and aircraft performances, in terms of both safety and efficiency. Because many of the changes in cockpit technology center around information management, proper design of advanced cockpit systems requires careful consideration of the human performance issues, particularly in the cognitive domain.

The MIT Aeronautical Systems Lab (ASL) has developed a part-task flight simulator specifically to study these issues. The simulator, based on a high-performance graphics workstation, replicates the Electronic Flight Instrumentation System (EFIS), Flight Management Computer (FMC), and primary autoflight systems of a modern "glass-cockpit" aircraft such as the Boeing 757/767 or 747-400. The simulator was initially developed to study cockpit presentation of microburst alerts, but has been used to study other topics including terrain awareness and alerting displays, datalink of ATC clearance amendments, and electronic approach plates.

5.2.2 Functional Requirements

To evaluate human cognitive performance issues, the autoflight systems and primary flight displays which affect decision-making needed to be simulated as exactly as possible. In addition, the need to test many different prototype displays demanded rapid reconfigurability. These requirements were achieved by simulating the graphical displays on a commercially-available workstation with high-performance graphical capabilities.

The simulation software was written in a modular fashion so that different displays could be implemented by recoding or replacing the appropriate modules.

A further requirement was simplicity. Since only outer-loop, cognitive-level issues were to be evaluated, it was assumed that all aircraft control would be performed using autoflight systems. Therefore, the autoflight and flight management systems needed to be simulated, but the direct flying controls (stick, rudder, throttles, etc.) could be omitted. For this reason no special hardware was required beyond general-purpose computers and some simple control panels, greatly reducing development and simulator set-up times.

5.2.3 Simulator Elements

Overview. As shown schematically in Figure 5.1, the full MIT ASL Advanced Cockpit Simulator facility utilizes three computers and several control panels to emulate

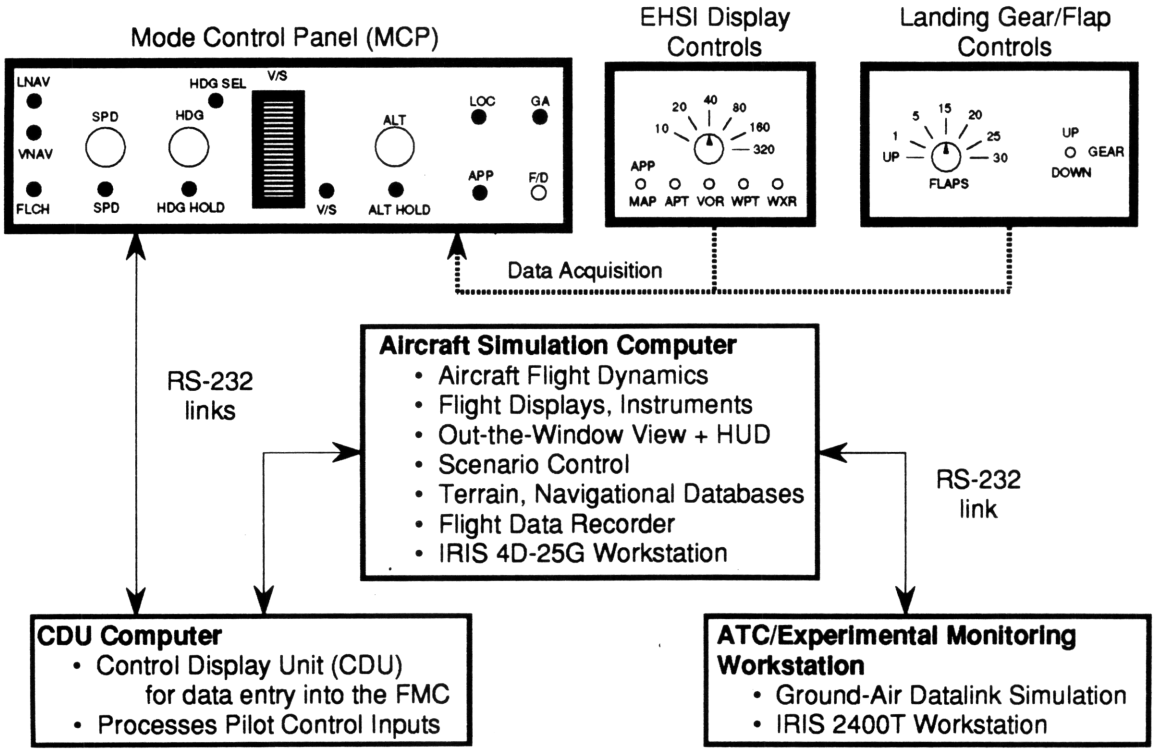

Figure 5.1. MIT ASL Advanced Cockpit Simulator. The simulator includes three computers and some auxiliary control panels, connected by standard RS-232 serial links.

cockpit displays, autoflight systems, and Air Traffic Control (ATC). A Silicon Graphics IRIS 4D-25G graphics workstation is used to display the cockpit instruments (Figure 5.2) and compute flight dynamics. The Control Display Unit (CDU) is emulated by an IBM-XT computer, and a Silicon Graphics 2400T workstation is used as an Air Traffic Control workstation (Figure 5.3). The portable version of the simulator omits the ATC workstation. Pilot input through the control panels is detected by the IBM-XT through a data acquisition unit. All three computers exchange data through standard RS-232 serial communication links.

Instrumentation. The simulator's cockpit displays are based on current "glass-cockpit" aircraft such as the Boeing 757/767 and 747-400. The IRIS screen depicts two

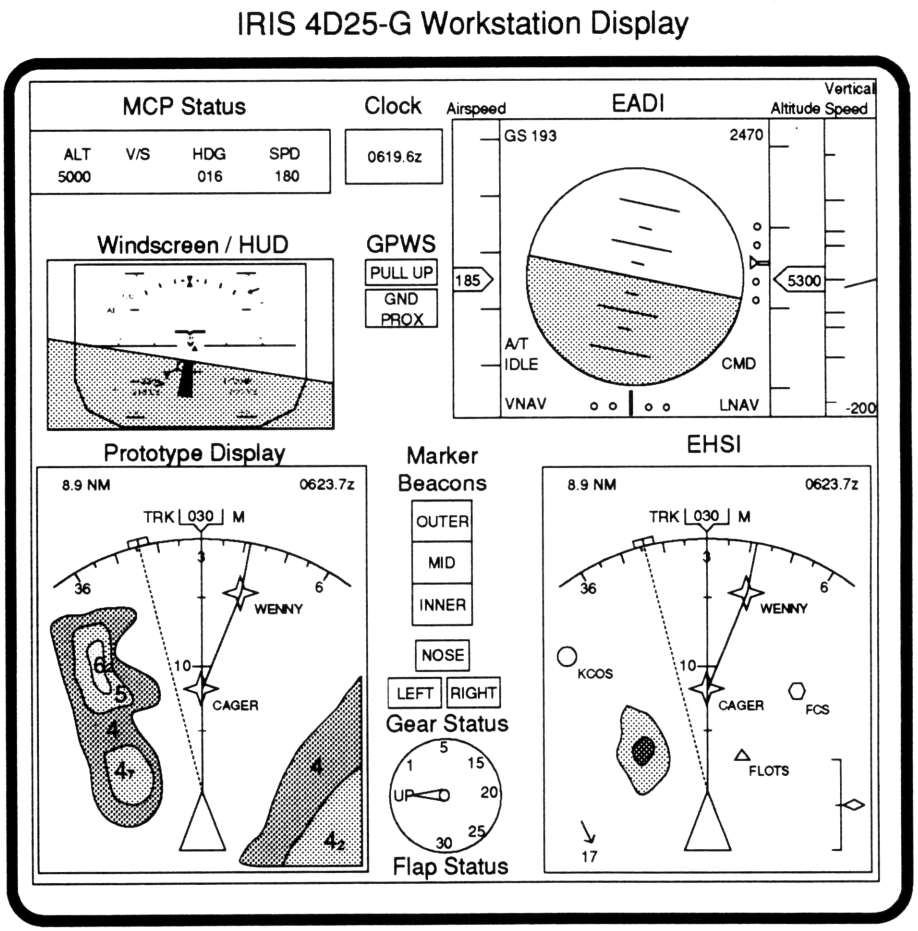

Figure 5.2. Primary Flight Instrumentation. This is a schematic view of the IRIS 4D-25G display in a typical configuration. Note that the electronic displays are actually in color on the simulator.

major cockpit displays, the Primary Flight Display (PFD) and Electronic Horizontal Situation Indicator (EHSI), along with several secondary displays. Additional displays can be rapidly prototyped and added to the simulator for evaluation. The nominal flight displays may then be rearranged or modified to accommodate the new displays as needed.

Airspeed, altitude, and vertical speed are indicated on the PFD using moving tape displays similar to those found on the B747-400. An Electronic Attitude Director Indicator (EADI) displays the artificial horizon, ground speed, radio altitude, and Instrument Landing System (ILS) localizer and glideslope deviations.

The EHSI is located below the PFD, as in the B757 or 767. The EHSI is the primary navigational instrument, and the simulator version is based on the map mode used in the B757/767. It includes information such as aircraft heading, ground track, FMC-programmed route, nearby airports and navaids, and wind information. Weather radar returns can also be displayed. A control panel is provided for setting the EHSI display range (10 to 320 nm) and for suppressing weather radar returns or off-track intersections, navaids, or airports.

Flap, gear, and marker beacon light displays are provided to the left of the EHSI. Controls allow the pilot to set the flaps and lower or raise the landing gear during the approach. Additional controls such as a manual pressurization valve can be added to the simulation if a side task is necessary to increase the ambient crew workload.

A simple perspective out-the-window view is provided as a means by which to cue the pilot that the aircraft has descended below the cloud deck. While in instrument conditions, the display appears gray. Below the cloud deck, a perspective view of the airport appears.

Autoflight and Flight Management Systems. The entry of flight path information into the Flight Management Computer (FMC) is accomplished through a Control Display

Unit (CDU) which is simulated with an IBM-XT computer. Several screen displays, or "pages," can be selected: The "Route" page to select a destination; the "Legs" page to select waypoints and vertical path constraints; and the "Direct-To" page to change the immediate waypoint. The CDU is linked to the EFIS so that active and modified routes are displayed both textually, on the CDU, and graphically, on the EHSI. At first, the CDU interface used a standard computer keyboard and monochrome monitor. At this time, a replica of the Boeing 757/767 CDU display and keyboard is being integrated into the system to enhance realism.

Non-FMC control of the aircraft is performed through an autopilot Mode Control Panel (MCP), similar to that used on the Boeing 757/767. A standard set of autothrottle and autoflight modes are available, including LNAV/VNAV flight (following FMC-programmed lateral and vertical flight paths) and the various capture ("select") and hold modes for airspeed, heading, vertical speed, and altitude. It is also possible to engage localizer and glideslope capture modes and a go-around mode for missed approaches.

Aircraft Dynamics. The basic aircraft flight dynamics are based on longitudinal point-mass equations of motion in wind axes, and simple decoupled first-order roll angle dynamics. The aircraft data used (provided by NASA Langley Research Center, and used by Hinton [1990]) is for a Boeing 737-100 aircraft, and includes non-linear curve fits for C_L and C_D as functions of angle-of-attack, flap position, and gear position. The multivariable inner-loop controller designed for this model took the form of a fully-coupled proportional-plus-integral cascade compensator and allows the aircraft to follow airspeed, flight path angle, and heading commands from the autoflight systems.

The autoflight systems provide outer loop control inputs and can operate in several different modes, ranging from simple altitude or heading holds up to full lateral and vertical path guidance (LNAV and VNAV) based on the FMC programmed route. Localizer and glideslope tracking modes can be engaged for final approach. Because

outer-loop controllers for the various autoflight modes are based on approximate frequencies and damping ratios for the Boeing 767 aircraft control system [Nadkarni, 1988], the aircraft responds like a 767 when being controlled through the autoflight systems.

For the microburst alerting experiments, a microburst wind model is available including both constant wind components and simulated microburst winds from an analytical model [Oseguera and Bowles, 1988].

ATC/Experiment Control Workstation. The ATC workstation (Figure 4.6) is used to monitor the progress of the aircraft's flight and, in some experiments, to issue ATC clearance amendments by a simulated datalink. A mouse-based graphical user interface provides the ability to select and deselect navigational information, determine the aircraft location relative to a scenario reference point, and select and specify content and format of the scripted ATC messages. The controller is in contact with the pilot through a wireless headset simulating a standard VHF radio link. Simulated datalink messages are

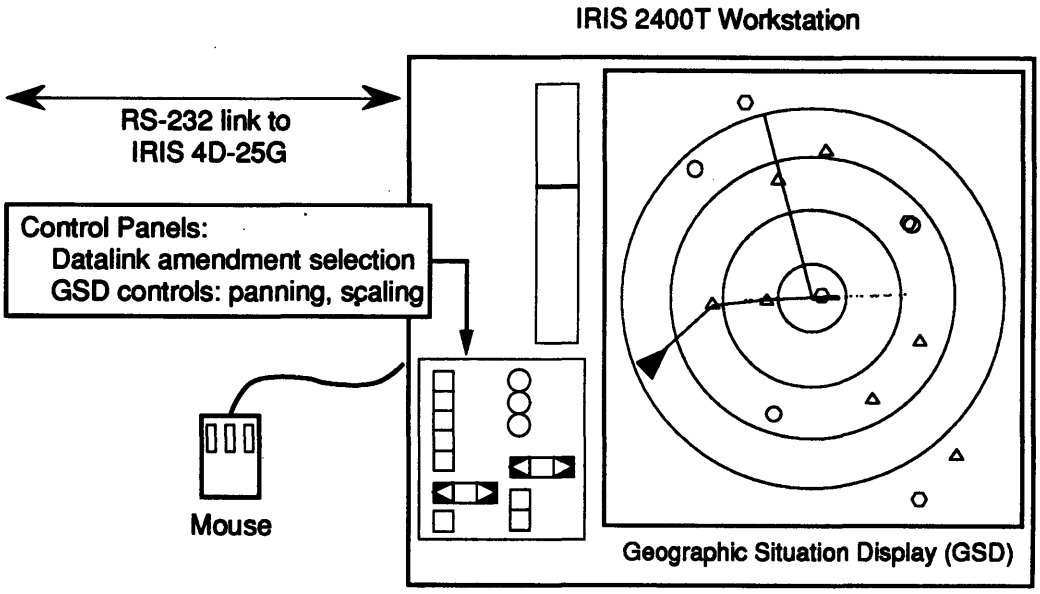

Figure 5.3. ATC/Experimental Control Workstation Display. The Geographic Situation display provides a airport-centered view of the scenario region, including the position of the simulator aircraft. It can be panned and rescaled by the simulation controller.

transmitted from the ATC workstation to the simulation computer via a serial communications link. It should be noted that this display was not intended to reproduce any actual or proposed advanced ATC workstation; it was designed only for simulation control.

Rapid Prototyping Capabilities. The flight displays were created using software written in the C programming language with IRIS Graphics Library primitives. This method of implementation allows flight displays to be rapidly reconfigured or redesigned to meet the varying demands of experimental studies. Typically, new displays may be created and added to the simulator in a matter of days. Commercially available display prototyping software was not used because of the excessive computational overhead associated with these systems.

Two additional programs were written to aid in developing displays common to several experiments. First, a software package was developed for the IRIS which facilitated the flexible, rapid creation of new chart display formats [Kuchar, 1990]. The program, called *Map*, allows the user to interactively create and modify electronic charts. Information may be grouped together in object-oriented layers which are then selectable by the pilot when flying the simulator. Also, a program called *WxrEdit* was developed to draw simulated weather radar reflectivity returns.

Scenarios can be set up and rapidly changed via English-language input files, which are read by the simulator software upon startup. These files define the starting aircraft position and state, pre-programmed FMC information, and scripted events to take place during a run. Scenario files also indicate *Map* and *WxrEdit* files to be loaded at start and during the runs.

5.3. Comparative Study of Cockpit Presentation Modes

5.3.1 Objectives

The analysis of the wind shear survey data in Chapter 4 indicated the requirement for better terminal area wind shear alerts, including possible use of digital datalinks for dissemination of ground-measured wind shear alerts. However, if wind shear alerts are uplinked electronically, there are several options for how they could be presented to the pilot. A part-task simulator experiment was therefore conducted to evaluate the advantages and disadvantages of *Alphanumeric (Textual)* and *Graphical* presentation modes in comparison to conventional *Verbal* communications for microburst alerts.

The microburst alert experiment was done in conjunction with a parallel study on presentation modes for ATC clearance amendments. The results presented below are primarily from the microburst alerting portion of the experiment. Complete results from the ATC portion of the experiment are available in [Chandra, 1989] and [Wanke, et. al., 1990].

5.3.2 Experimental Design

Overview. In this experiment, active airline pilots flew nine descent and approach scenarios into the Denver-Stapleton airport under potential microburst conditions. During these scenarios, ATC clearance amendments and microburst alerts were issued to the pilot in three different presentation modes: *Verbal*, *Alphanumeric (Textual)*, and *Graphical*. Pilot decision-making performance was observed. Subjective data was obtained from post-experiment interviews and from a simple workload evaluation technique.

Presentation Modes: ATC Clearances. *Verbal* clearance amendments were given by the simulation controller in a manner consistent with current ATC operating

procedures. *Textual* clearance amendments contained the same wording as the verbal alerts. These amendments were triggered remotely by the controller, and the text of the message appeared on the CDU screen when called up by the pilot. In the *Graphical* mode, clearance amendments appeared on the EHSI as an alternate route indicated by a dashed white line. The arrival of both textual and graphical amendments was signaled by an aural tone, and both types of amendments were accepted or rejected with a single CDU keystroke. Pilots were not required to read back text or graphical amendments, but did read back verbal amendments as per standard procedures.

Presentation Modes: Microburst Alerts. In order to ensure that all presentation modes had the same information content, and to measure the pilot's ability to discriminate between threatening and non-threatening situations, microburst alerts always contained warnings for *all* possible approach runways. It should be noted that this is not the standard TDWR/LLWAS procedure in which verbal alerts are only issued for the runway being used by the aircraft. Initial audio cues were given in all three presentation modes, so that the method and time of initial notification was kept constant.

Verbal microburst alerts were issued as radio messages from the controller. *Textual* microburst alerts appeared in an alphanumeric window just below the EHSI display. The content of the verbal and text alerts was modeled after TDWR alerts. A sample verbal alert: "IRIS three-five-four, Microburst Alert. Expect four-zero knot loss, 2 mile final approach runway one-seven-left." *Graphical* microburst alerts appeared on the EHSI as flashing solid white circles with the intensity (headwind-to-tailwind change in knots) drawn inside them in red numerals. The circles encompassed the microburst outflow region, and were typically 1 to 1.5 nm in diameter. An example is shown in Figure 5.4.

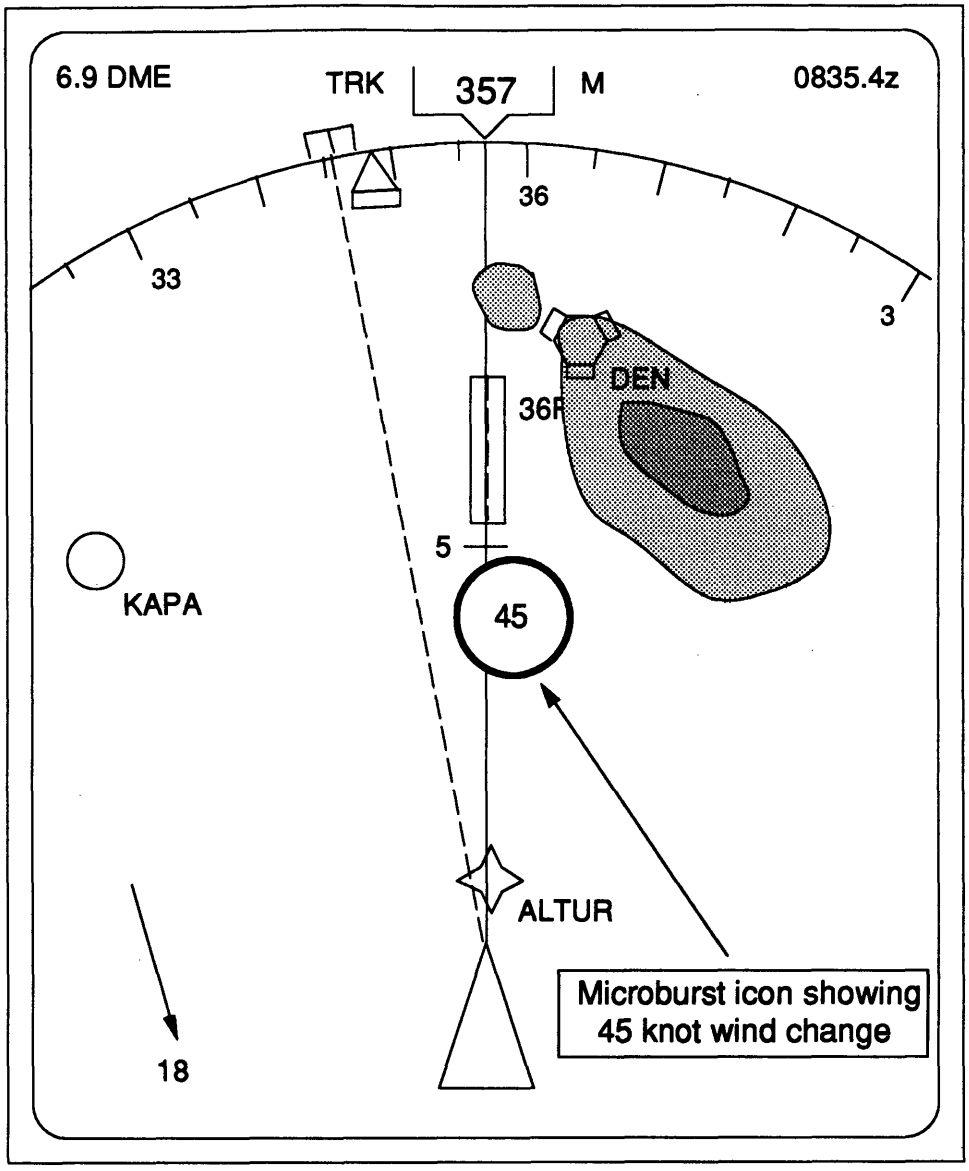

Figure 5.4. Schematic View of Graphical Microburst Alert Format. The microburst icon is a filled white circle or "band-aid" shape with a red border and red text indicating the measured max wind change.

Scenario Design. All nine scenarios were set in the Denver terminal area for two reasons: (1) The high incidence of microburst activity made microburst alerts credible, and (2) a large number of descent profile and landing runway combinations were possible. Both ATC amendments and microburst alerts occurred in each scenario. This made it more difficult for the pilot to anticipate microburst alerts.

Each scenario was divided into two phases. The aircraft started at the outer limit of the terminal area with an initial flight plan pre-programmed into the FMC. During descent, three amendments which required reprogramming of the FMC were given.

The microburst alerting phase of the scenario began when the aircraft was vectored towards the final approach course. There were three independent variables in the microburst alerting phase:

1) Presentation mode: *Verbal*, *Textual*, or *Graphical*

2) Situation: *Threatening* or *Non-Threatening*

3) Time of alert: *On final approach* (at the outer marker) or *Early* (once at 20nm and once at 10nm from the airport)

In a "threatening" situation, a microburst occurred directly on the final approach path of the runway being used. In a "non-threatening" situation, a microburst occurred on the approach or departure end of a different runway, well outside the TDWR alerting boxes for the active runway. Note that these definitions are slightly ambiguous, in that occurrence of a microburst anywhere near the airport can be considered somewhat threatening.

The time of alert was also varied. In six of the scenarios, the alerts were given when the aircraft reached the outer marker (6 to 9 nm from touchdown). In the other three, the first alert was given earlier when the aircraft was 20 nm from the Denver VOR, follwed by a second alert 10 nm from the VOR. In all cases, the microburst position and intensity did not change once an alert was issued. The test matrix is given in Table 5.1.

Table 5.1. Scenario Characteristic Matrix

Block ID	Run #	Scenario Type	Time of Alert
A	1	Non-Threatening	On Final
	2	Threatening	Early
	3	Threatening	On Final
B	4	Threatening	Early
	5	Threatening	On Final
	6	Non-Threatening	On Final
C	7	Threatening	On Final
	8	Non-Threatening	On Final
	9	Threatening	Early

The matrix was divided into three blocks. All ATC amendments and microburst alerts in a block were given in the same mode, and the mode was rotated between blocks. Over the subjects tested, all scenario blocks were tested in all three modes, and the order in which the subject encountered the modes was rotated. This was done to counterbalance learning and scenario-dependent effects.

Subjects. With the support of the Air Line Pilots' Association, eight active 757/767 line pilots volunteered for the experiment. All subjects were male; five were captains, and three were first officers. The pilots ranged in age from 30 to 59 years, with a mean of 47 years. In addition, several other pilots of varying experience assisted in the development of the simulator and the scenarios.

Experimental Procedure. At the start of the session, the pilot was asked to complete the first stage of a NASA-designed workload evaluation [Hart and Staveland, 1986] which asked him to prioritize the different types of workload for the specific task of flying a 757/767 aircraft. Next, the features of the simulator were demonstrated. A sample scenario was used to demonstrate all of the three modes for both phases of flight. When the subject became comfortable with the operation of the simulator, the test scenarios began. The pilot was requested to fly the simulator with the same level of responsibility as he would use in an actual aircraft.

At the start of each scenario, the pilot was given an initial clearance into Denver-Stapleton and provided with the charts necessary to make the approach. Each scenario lasted from 20 to 35 minutes. During the flights, one experimenter served as the ATC controller and one remained in the cockpit with the pilot to answer questions about physical operation of the simulator. After each scenario the pilot completed a separate subjective workload evaluation sheet for the descent phase (the clearance amendment task) and for the approach phase (when microburst alerts were given). After the complete session there was a debriefing in which the pilot's impressions of the simulator and the presentation modes were solicited. The cockpit was videotaped during the experiment to record ATC and intra-cockpit communications and actions. In addition, the simulator software recorded all flight data and pilot control inputs during the run.

5.3.3 Results and Discussion

Quantitative data for the clearance amendment delivery task included time performance data and a record of detection of unacceptable clearances [see Chandra, 1989; Wanke, et. al., 1990]. For microburst alerts, pilot decision-making performance was measured. Subjective workload ratings were taken for both tasks at the end of each scenario. Although statistical significance was not achieved for the majority of quantitative measures due to the small number of subjects, the convergence of evidence from several measures permits reasonable confidence in the trends that were obtained.

Performance Data. The measure of pilot performance for the microburst alerts was the percentage of "correct decisions" made in each presentation mode. An incorrect decision was scored for either (1) avoidance action taken during a "non-threatening" scenario, or (2) no avoidance action taken in a "threatening" scenario. The data (Figure 4.8) show that the fewest errors were made with graphical microburst alerts, and that the most were made with text alerts. This implies that text alerts may actually degrade

performance relative to verbal alerts, although the difference was not statistically significant.

An additional observation was that the positional information contained in the graphical mode actually led several pilots to request and program non-standard missed approach procedures in advance in order to avoid the wind shear areas completely. When the pilots were given the same information in the other modes, this was generally not observed.

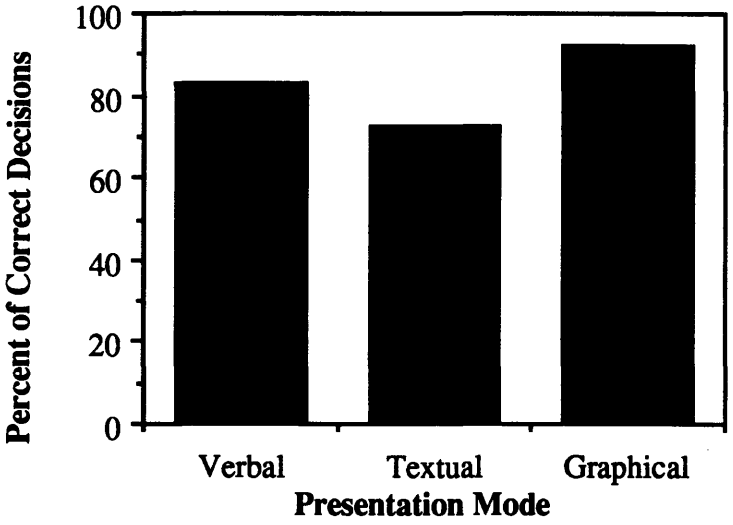

Figure 5.5. Pilot decision-making performance for microburst alerts by presentation mode

Workload Ratings. The NASA Task Load Index [Hart and Staveland, 1986] was selected to assess workload for both tasks in each of the modes. This scale divides workload into six components: mental demand, physical demand, temporal demand, effort, frustration and performance. The ratings were made along a continuous scale from "very low" to "very high". Weightings for each of the six factors given above are obtained individually for each subject through a paired comparison task during subject orientation. The weights are simply the number of times a particular component was chosen to be a more important contributor to workload.

The overall workload ratings for each mode are plotted in Figure 5.6. For both tasks, the average workload rating for the graphical mode was lower than the rating for the verbal and textual modes. The six sub-scale ratings all showed a similar trend. The appearance of greater workload induced by the textual condition is not a significant effect.

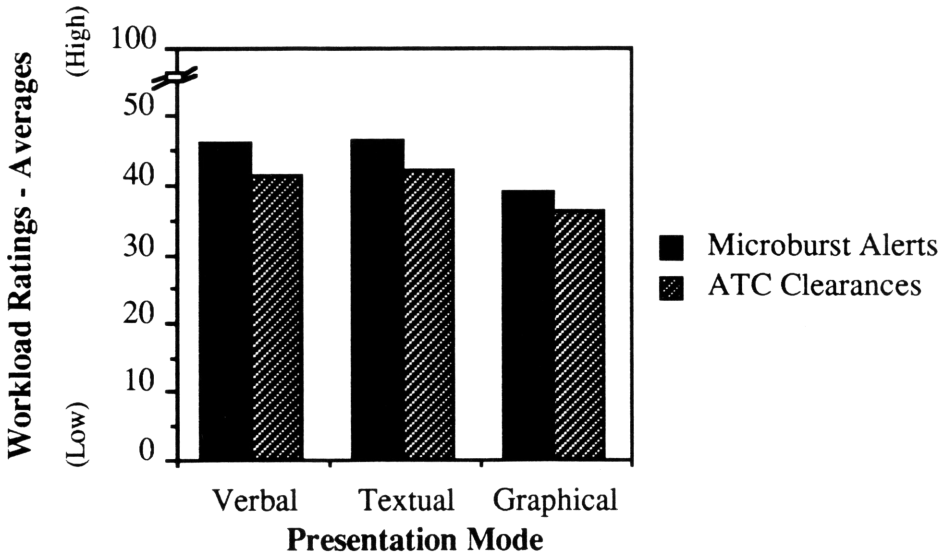

Figure 5.6. Mean pilot subjective workload ratings by presentation mode

Pilot Preferences. Pilot comments and subjective evaluations of the presentation modes were obtained through loosely structured post-experiment interviews. In their evaluation of the modes, pilots overwhelmingly preferred the graphical mode of presentation (Figure 5.7) for both types of messages. For microburst alerts, the text mode was consistently rated less desirable than the verbal mode. Pilots indicated that textual information was undesirable during final approach due to the additional head-down time required to read it. For clearance amendments, the text and verbal modes seemed to be equally desirable from the averaged ratings. However, some pilots greatly preferred the text mode over the verbal, while others preferred the exact opposite (hence the mid-range average value). All pilots indicated that they were comfortable with current verbal procedures, and they did not feel that the advantages of the text mode were significant.

The pilots were also asked about the usefulness of "party-line" information, which is implicit information acquired by listening to communications between ATC and other aircraft in the terminal area. Digital datalink messages, if directed to specific aircraft, would effectively eliminate "party-line" information. Some pilots stated that this information gave them a better understanding of the overall situation and enabled them to be better prepared when an alert arrived. Other pilots indicated that they could do without the information. This is an important consideration for datalink use, and has been addressed by other MIT investigators [Midkiff and Hansman, 1992].

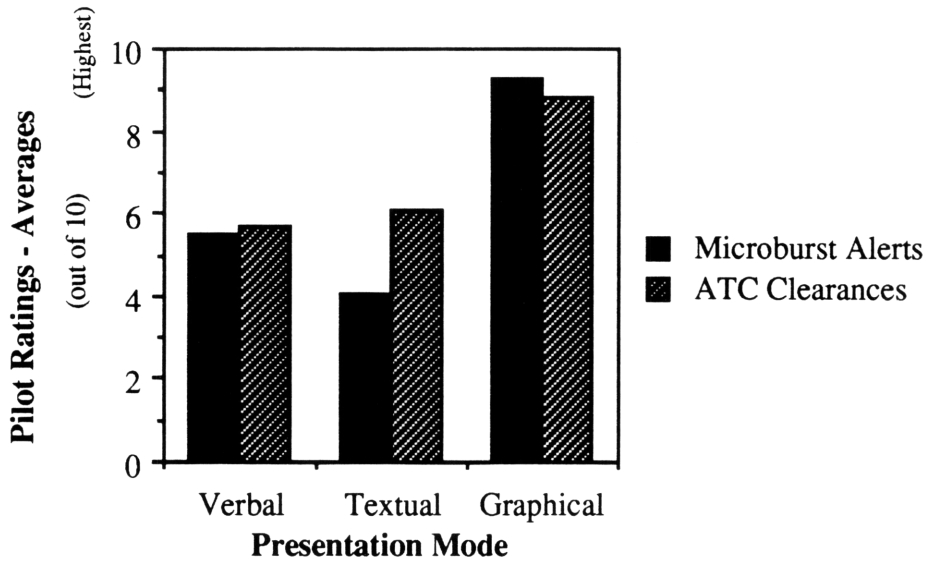

Figure 5.7. Pilot preference ratings by presentation mode

5.3.4 Conclusions

The consistency between the survey and simulation results allows the following conclusions to be drawn. Pilots are generally receptive to the idea of automated ground-to-air information transfer and electronic cockpit presentation. From the survey results, the post-simulation interviews (pilot preferences), and the simulation results (workload, performance) it appears that graphical presentation of both microburst alerts and clearance amendments offers important advantages over verbal communications. To

obtain this benefit, the format of graphical microburst alerts must be designed to clearly convey only the necessary information without clutter or data overload. Pilots identified this minimum presentation to be a simple symbol showing microburst location, approximate extent, and intensity.

Information received over a digital datalink may also be presented as alphanumeric (textual) messages. Again, the survey results were consistent with the experimental results. For microburst alerts, the textual mode of presentation was universally rated poorly, while the ratings were mixed for ATC amendments. In both cases, the textual mode did not appear to reduce workload or improve performance. For ATC amendments, comments indicated that the familiarity of operational pilots with verbal communications outweighed any advantages of textual presentation. For microburst alerts, which occur during final approach, pilots disliked the additional head-down time required to read textual information.

5.4. Experimental Evaluation of Graphical Microburst Alert Displays

5.4.1 Objectives

The experiment discussed in Section 5.3 demonstrated that graphical alerts have benefits in terms of faster comprehension time, reduced crew workload, and increased crew situational awareness. Based on these results, a second simulator experiment was designed to evaluate specific format and implementation issues associated with graphical microburst alerts displayed on an Electronic Horizontal Situation Indicator (EHSI). The issues addressed are summarized below:

1) Is it possible to add microburst alerts to the EHSI display during normal flight operation without creating visual "clutter"?

2) Should multiple levels of microburst intensity be displayed, or is one level ("hazardous") sufficient?

3) Should measurements from all of the available sensors be combined to form a single "fused" alert, or should alerts from different sources be independently displayed?

4) Does lack of correlation between weather radar reflectivity and microburst alerts affect pilot confidence in the alerts?

5) What are the procedural implications of displaying graphical alerts.

5.4.2 Experimental Design

Overview. In this experiment, active airline pilots flew a series of descent and final approach scenarios, under weather conditions conducive to wind shear, in the MIT Advanced Cockpit simulator. Similar situations were flown with several different display formats in order to evaluate the issues listed above. After the flight segment of the experiment, the pilots were asked to complete an exit questionnaire in order to obtain their opinions of the different display options. Additional data was obtained from observations and measurements made during the flight scenarios as well as from short debriefing sessions which took place between the scenarios.

Microburst Display Formats. Three prototype microburst alert formats were designed with several different features related to the issues listed above. Pilots flew similar scenarios with the three displays, and were then asked in the exit questionnaire to comparatively rate the displays both as a whole and by specific display feature. Schematic views of the three display formats are shown in Figures 5.8, 5.9, and 5.10. Note that an analytical microburst model was incorporated in the simulator software to generate realistic microburst winds, so the icons and associated intensity levels for the three display formats did actually correspond to winds experienced by the simulated aircraft.

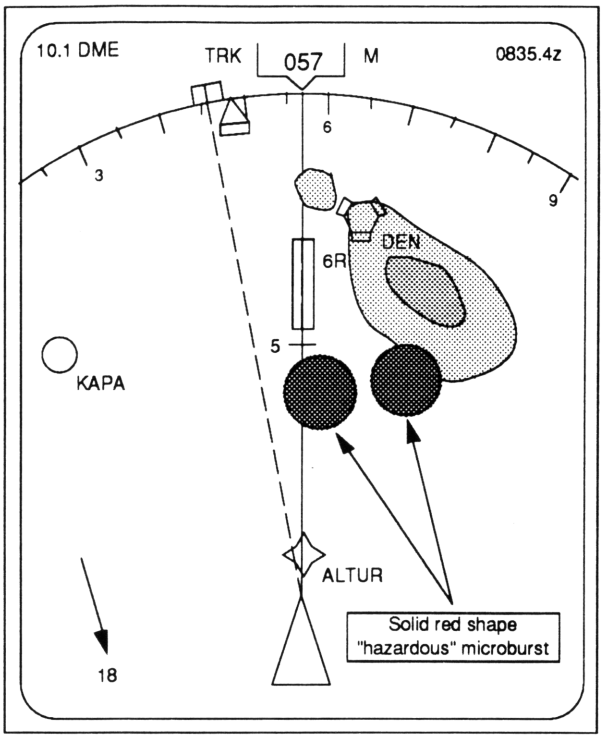

Figure 5.8. Example of Display A on the EHSI.

Display A was the simplest display. Only "hazardous" microburst regions were shown, and data from all available sensors was assumed to be combined or "fused" to provide a single alert. Alerts were displayed as flashing solid red circles on the EHSI. The hazard threshold was based on the "F-factor" microburst hazard criterion (Section 2.1.2) averaged over one-half mile. When this value exceeded 0.1, an alert was issued. The advantages of using the F-factor criterion, rather than maximum horizontal wind change (as used in the TDWR system and in Section 5.3), to set alert thresholds will be addressed in Chapter 6.

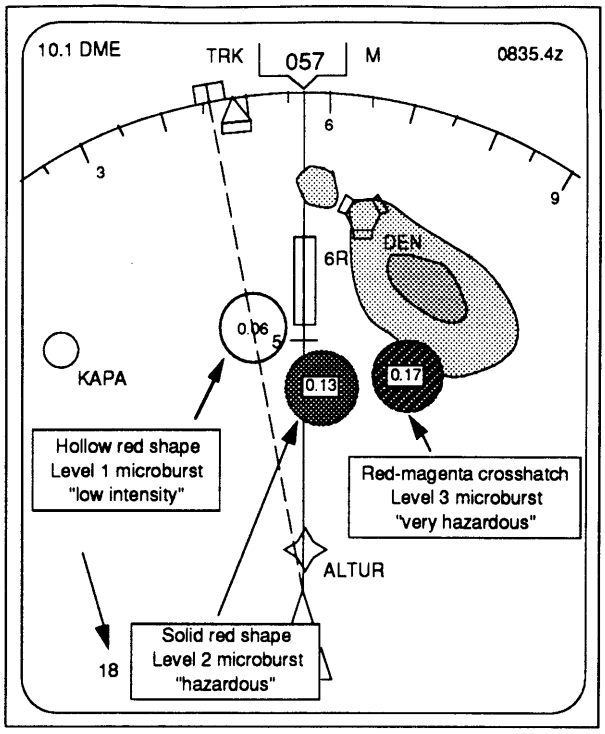

Figure 5.9. Example of Display B on the EHSI.

Display B was designed to evaluate the need for intensity information. It was a three-level display, also based on F-factor averaged over one-half nautical mile. A description of the level structure is given in Table 5.2. A level 1 microburst alert was displayed as a flashing hollow red circle, a level 2 alert was displayed as a flashing solid red circle, and a level 3 alert was displayed as a flashing magenta/red striped circle. In addition, the F-factor values were overlaid in white numerals, in order to generate pilot commentary about the use of numerical data on the display. Note that level 1 alerts as defined for this display would not be shown at all on displays A or C, since the hazard value range falls below the "hazardous microburst" threshold ($F > 0.1$).

Table 5.2. Alert intensity levels for Display B

Alert Level	F-Factor Range	Description
1	$0.05 \leq F < 0.1$	"low intensity"
2	$0.1 \leq F < 0.15$	"hazardous"
3	$F \geq 0.15$	"critically hazardous"

The explanation of the F-factor hazard criterion to the pilot was critically important to this study. This was done with reference to the three-level display (B). It was explained that F-factor measures the loss of effective thrust-to-weight ratio (and hence available climb rate) due to the windfield, and that a typical jet transport-category aircraft has an excess thrust-to-weight ratio of approximately 0.15 (varying with aircraft type and weight). It was then explained that a level 1 alert would indicate a loss of one-third to two-thirds of the aircraft's climb capability, a level 2 alert would indicate loss of two-thirds to all of the aircraft's climb capability, and a level 3 alert would indicate a microburst which would essentially compel the aircraft to descend.*

Display C was designed to evaluate the need for knowledge of the source of the alerts, and specifically provided separate alert icons for ground-based and airborne forward-look wind shear sensors. Ground-based alerts were issued for $F > 0.1$ and were displayed as flashing solid red circles. Regions of hazardous wind shear detected by airborne sensors (i.e. where $F > 0.1$) were displayed as red/yellow striped regions. The airborne sensor was assumed to have a maximum range of 5 nm and to scan 20° to each side of the aircraft's flight path. In all cases, the airborne alerts and ground-based alerts were roughly consistent. The problem of receiving conflicting measurements from the different sensors was therefore not addressed.

* This explanation of F-factor was suggested by Dr. Roland Bowles and David Hinton of the NASA Langley Research Center.

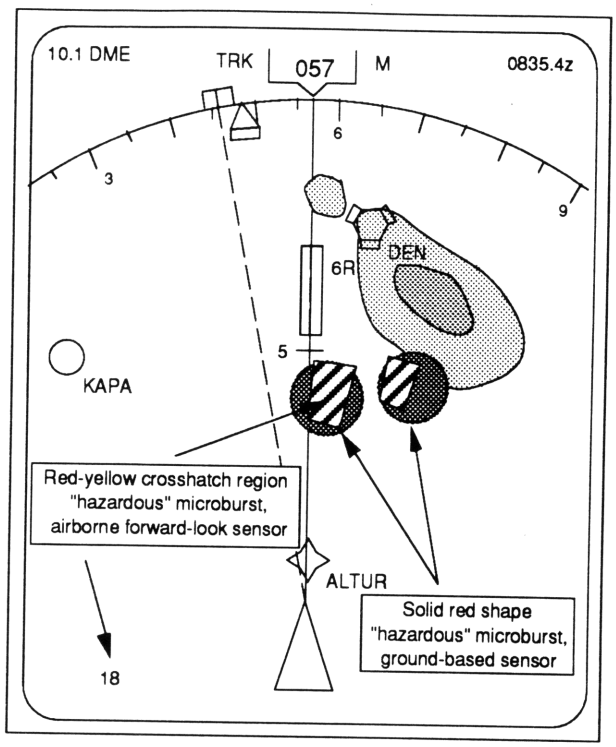

Figure 5.10. Example of Display C on the EHSI.

Scenario Design. A total of 12 approach scenarios were flown by each pilot subject. These were chosen to evaluate the reaction of the pilot under differing conditions to the three displays, both quantitatively and qualitatively, and to stimulate commentary for the exit questionnaire. There were 3 independent variables in the experimental matrix:

1. Microburst display format: *A*, *B*, or *C*.

2. *"Wet"* or *"dry"* microburst conditions (Presence or absence of heavy precipitation)

3. *Threatening* situation (hazardous microburst present on approach path) or *non-threatening* situation (No hazardous microbursts within 1.5 nm of approach).

The precipitation (radar reflectivity) patterns for the "wet" and "dry" cases were chosen to be loosely representative of "typical" microburst events as described in the

literature [Wolfson, 1988; Fujita, 1985]. In the wet cases, thunderstorms were present in close proximity to the airport, with microbursts occurring either in the center or on the edge of high-reflectivity regions. In the dry cases, only light precipitation was present in the area of microburst activity.

The "threatening" and "non-threatening" cases were chosen to stimulate commentary on the operational use of the alerts. In the "threatening" case, hazardous microburst alerts (level 2 or 3) appeared directly on the flight path, and in the "non-threatening" case hazardous microburst alerts occurred at a lateral distance of 1.5 to 2 nm from the flight path. "Non-threatening" in this case does not presuppose that the pilot *should* make the approach if a microburst is present 1.5 nm laterally displaced from the flight path; it only indicates that, under the current TDWR alert methodology, no alert would be issued (Section 2.5.2). In both cases, alerts began to appear when the aircraft approached to within 12-15 nm of the airport, and grew from level 1 to level 2 or 3 events before the aircraft reached the outer marker.

The nominal test matrix is shown in Table 5.3. Note that the effect of high vs. low precipitation was only tested using display A. Also, microbursts were present in only 8 of the 12 runs. In order to prevent anticipation, the microburst alert experiment was run in conjunction with a graphical terrain display experiment. In the cases where no microburst was present, terrain threats were present. The scenarios were carefully designed to prevent interference between the two experiments, and appeared to be effective in reducing pilot anticipation of both terrain and weather threats. The 12 scenarios were classified into three groups by display type, and the order of presentation of the blocks was alternated between subjects to attenuate learning effects. In each scenario, the aircaft was initially positioned between 25 and 50 nm from the airport, and was then vectored to an ILS approach. The scenarios averaged 10 to 15 minutes in length.

Table 5.3: Scenario Characteristics. The order of the four blocks shown below was rotated between subjects to counterbalance learning effects.

Run #	Display Type	Wet/Dry	Scenario Type
1	A	Wet	No Microbursts
2	A	Dry	Non-Threatening
3	A	Wet	Threatening
4	A	Dry	Threatening
5	A	Dry	No Microbursts
6	A	Wet	Non-Threatening
7	B	Wet	Non-Threatening
8	B	Wet	No Microbursts
9	B	Wet	Threatening
10	C	Wet	Threatening
11	C	Wet	Non-Threatening
12	C	Wet	No Microbursts

Experimental Procedure. The experiment began with an explanation to the subject of the purpose of both the microburst alert and terrain depiction studies. This included a brief discussion of the state-of-the-art in microburst detection and digital datalink, as well as the explanation of F-factor described above. The three display types were demonstrated and explained. Next, the pilot was given a practice run with the simulator to familiarize himself with the autopilot system, displays, and display controls.

The 12 scenarios were then run in two groups of 6, with a break between the groups. At the beginning of each run, the pilot was provided with an approach plate and the ATIS* , and given as much time as needed to study them. During each run, one of the experimenters acted as the air traffic controller, and communicated with the pilot via a wireless headset. The controls and displays were videotaped, and the appropriate numerical data was recorded by the simulation computer. After the 12 runs, an exit questionnaire was conducted in order to obtain comments and numerical rankings of the

* The ATIS (Automatic Terminal Information Service) is a continuous radio broadcast of airport weather conditions and other non-control information in selected terminal areas.

displays and their features. The experiment required approximately 3 hours per subject to complete.

Subjects. All of the subjects were active line pilots currently flying EFIS/FMC-equipped aircraft (Boeing 757-767, MD-88). Nine subjects participated, and all were males between the ages of 36 and 51. Three of the pilots were captains, and six were first officers. The subjects averaged 5890 hours of total flight experience, and averaged 1130 hours of flight experience on EFIS/FMC-equipped aircraft.

5.4.3 Results and Discussion

Visual Clarity of Alerts on EHSI. In the exit questionnaire, the pilots were asked to rate the three displays individually for visual clarity on a scale from 1 ("very difficult to read") to 4 ("very easy to read"). The results were similar for all three displays; all were rated easy or very easy to read, with average ratings between 3.5 and 4. In the final approach situation, the pilots were typically observed to set the EHSI to the minimum available range (10 nm) with airports, navaids, and off-route waypoints suppressed, so the microburst alerts were by far the most prominent features on the display.

Overall Display Ratings. The numerical preference rankings from the exit questionnaire give the best idea of the general acceptability of the three display formats. In this question, the subjects were asked to rank the three displays (A, B, and C) by order of preference from 1 (most preferable) to 3 (least preferable). Display B, with three intensity levels, was ranked highest on average, followed by the discrete Display C second, and Display A last (Table 5.4). Although several of the pilots remarked on the need for simple and easy to comprehend displays, display A was *never* ranked the best. This may indicate that the single-level, fused-data icon representation did not contain sufficient information. Several pilots contended that they would like to see a display with

Table 5.4 Mean pilot preference rankings for the three display types. A ranking of 1 indicated most preferable, 3 indicated least preferable.

Display Type	Number of Times Ranked First	Mean Ranking
A	0	2.67
B	5	1.56
C	4	1.78

both multiple intensity levels and information separated by source, although no suggestions about how this would be implemented were offered.

Figure 5.11 shows the averaged responses to a question which asked the pilots to rate the three formats *individually* from 1 to 4 in terms of how useful they are to understanding the weather situation. A response of 1 indicated "not at all useful," while 4 indicated "very useful." The data indicates that display B was thought to be most useful, followed by display C. This is consistent with the overall preference ranking discussed above. It is also important that all of the mean ratings exceeded 3, which indicates that all of the displays were considered generally useful.

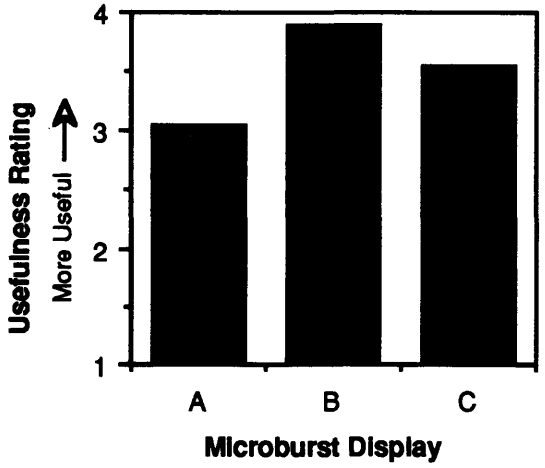

Figure 5.11. Mean pilot usefulness ratings for the three displays

Need Rating of Specific Display Features. The exit questionnaire included a section concerned with specific features of the displays. The subjects were asked to rank the need for three particular display features, from 1 ("unnecessary") to 4 ("essential"). The numerical results are summarized in Table 5.5. The ratings and associated subject

Table 5.5. Pilot rating of specific display features by need. The response scale ran from 1 (unnecessary) to 4 (essential).

Display feature	Mean need rating	Standard deviation
3-level intensity information (Display B)	3.17	0.353
Numerical F-factor information (Display B)	2.22	1.20
Different sensors displayed separately (Display C)	2.44	1.21

comments are discussed below. Note that Display A, having none of the specific features rated, served as a standard against which to evaluate the features.

Need Ratings: Three-level Intensity. The concept of displaying three levels of intensity (as in display B) rather than the single level alert (as in display A) was strongly supported, with an average rating of 3.17. All subjects rated three-level intensity information between 3 and 4. Several pilots remarked that having multiple intensity levels was important to their decision-making process, since it implicitly provided intensity trend information. With respect to this point, it should be noted that in all scenarios the microbursts increased in intensity during the approach. This is not unrealistic, but tended to draw attention to the intensity trend issue. Another observation was that microburst intensity level influenced how closely the pilot would approach the microburst. Pilots indicated that they would give a wider berth to a level 3 microburst than a level 2, even though both were above the "hazardous" intensity threshold. One of the subjects also stated that having multiple intensity levels made the alerts more compelling, and induced closer study of the situation (as compared to a single-level alert format).

Need Ratings: Numerical F-factor Information. The numerical F-factor display feature was rated lower than three-level intensity (2.22), and the large standard deviation indicates the large spread of responses on this question. Four of the subjects ranked this feature "unnecessary". One pilot indicated that the numbers would be distracting, and that color-coded information is much easier to interpret. Another pilot stated that more alert levels would be desirable, but that the F-factor numbers required too much thought.

He suggested a scale from 1 to 10. However, several did rate them highly in terms of need, and one pilot actually preferred the numbers to the three-level intensity arrangement due to the finer intensity resolution available. In general, the performance implication of the F-factor numbers was understood and found to be a good justification for the alert level thresholds, but no consensus was reached as to their usefulness in real-time situations.

Need Ratings: Different Icons for Different Information Sources. Similarly mixed responses were received for the need to know the source of the information (display C). Again, the average was near middle scale (2.44), but the responses were strongly split between the ends of the scale. Several pilots reacted positively to the separated alerts since they found it useful to know when the airborne sensor confirmed the ground-based report. One pilot stated he would not need verbal confirmation of the alert from the tower if he saw that the airborne and ground-based sensors were reporting approximately the same information. This was borne out by his actions when flying the simulator. It is important to note that in the scenarios the ground-based and airborne sensor alerts were never contradictory.

Other pilots indicated that different icons were not necessary, since if *any* sensor reported a microburst on or near the flight path, there would be no question of complying with the alert. Given this fact, they found knowledge of the alert source to be irrelevant. One pilot stated in the exit debriefing "if I saw one or the other alone, I would still have to assume that it was one hundred percent accurate."

Decision Distance. In the cases where a hazardous microburst was present directly on the approach track, the point where the pilot initiated a missed approach was observed. The distance from this decision point to the nearest microburst icon on the flight path was defined as the "decision distance". It was tabulated for all 36 of the "threatening" scenario runs. The mean decision distance was 4.26 nm with a relatively

low standard deviation of 1.15 nm. This result is potentially useful for helping define crew response procedures for these alerts. It also emphasizes the importance of a reliable ground-based detection and uplink capability, since most of the pilots made their decision at the approximate design limit range of several of the airborne sensors currently under development [Bowles, 1990].

Effect of Graphical Alerting on Missed Approach Planning. It was observed that the pilots typically asked for a turn when requesting a missed approach. In several cases, the pilot informed the tower well in advance (sometimes before the aircraft had reached the outer marker) of which direction he would like to turn in the case of a missed approach. Several subjects indicated that the positional information which allowed this kind of missed approach planning was the best feature of a graphical presentation.

One pilot commented that, if the controller insisted on a straight ahead missed approach which took the aircraft through the microburst alert, he (the pilot) would exercise his authority to make an emergency deviation. In another case, a pilot requested a turn to avoid a microburst which took the aircraft directly through a high reflectivity thunderstorm precipitation core indicated in red by the weather radar. The aircraft at this point was still several miles from the microburst. A straight ahead missed approach would have taken the aircraft through the microburst region at about 2000 feet AGL with a well-established positive climb rate. The hazard involved in the straight ahead missed approach in this case was low, and probably less than that involved in making the turn into the storm. In none of the cases did the pilots appear to consider a straight-ahead missed approach as an option, even when the decision to abort the approach was made 5 to 10 nm from the microburst location.

Display of Low Intensity Alerts. A connected issue relates to display of low intensity or less hazardous microburst alerts. Although none of the scenarios were explicitly designed to test this issue, it was apparent from several of the pilots' comments

and actions that a graphical alert of *any* magnitude on or very near the approach was grounds for a missed approach. Comments suggested that this was due to two possible reasons: (1) microbursts were observed to change in intensity fairly quickly, and (2) if *anything* is reported on the flight path, and the aircraft experiences *any* wind shear or other atmospheric disturbance, then the pilot may appear negligent for proceeding with the approach in the presence of an alert icon. In view of this latter possibility, it is possible that any graphical alert *no matter how low in intensity* located on the approach or departure track will induce the pilot to abort, if not for safety than for legal reasons. It is apparent that the lowest alert threshold must be carefully set in order to balance safety vs. operational efficiency.

It must also be considered that such behavior may have been an artifact of the simulation environment. This high level of caution is in sharp contrast to the responses to verbal alerts issued during recent TDWR operational evaluations. Low intensity "wind-shear-with-loss" alerts do not require a missed approach to be made, and pilots have been observed to continue approaches during microburst alerts of fairly high intensity [Stevenson, 1989; McCarthy and Sand, 1990].

Acceptable Lateral Separation Distance. Since several scenarios forced the pilots to make decisions about microbursts which occurred 1.5 to 2 nm from the approach, it was possible to ask the question "how close can a hazardous microburst icon come to the approach path before you will decide not to make the approach?" Six of the subjects were able to give a quantitative distance, based on a "hazardous" microburst alert icon as used in Display A. Responses ranged from 2 nm up to 15 nm, and four of the six pilots who answered this question gave distances of 2 and 3 nm.

In contrast, the current TDWR alerting methodology only gives an alert if any part of the microburst shape comes within 1 nm of the approach, and even with this criterion "nuisance alerts" occur (see Section 2.5.2). This implies that the positional

information contained in graphical alerts could have a positive effect on pilot confidence in the alerting system. If the pilot makes an approach when a microburst alert is given for an event 1 or 2 nm from the approach path, and experiences no wind shear, the graphical alert makes it visually apparent that the aircraft has not actually penetrated the center of the microburst region. Under the current verbal alerting system, which gives no clear indication of the position of the microburst core, the pilot perceives such a situation as a false alarm.

Microburst Alerts During "Wet" and "Dry" Conditions. One of the issues explicitly tested was the sensitivity of pilot decision-making to varying precipitation levels. No significant differences in pilot response were observed between "wet" and "dry" microburst situations. In one case, when microbursts appeared under very light rain conditions, a pilot commented that "that shouldn't be there," but in no cases did a pilot simply ignore an alert because of light precipitation. In reality, when "dry" microbursts are present, other visual clues (virga, dust rings, etc.) would likely be present. These were not simulated.

5.4.4 Conclusions

The following conclusions were reached with respect to the simulation objectives stated in Section 5.4.1:

- Graphical microburst alerts on the EHSI were found to be clear and useful.
- Alerts with multiple intensity levels were preferred over single-level alerts. Comments indicate that alert levels should be identified by different icon colors or patterns rather than numbers.
- Pilot opinion was divided over the issue of whether to present "fused" or "discrete" alerts. The primary tradeoff appears to be the improved accuracy available through data fusion versus the added confidence gained by the pilot when he is aware of reinforcing data from different sensors.

- The effect of precipitation (radar reflectivity) on the credibility of the microburst alerts was found in this experiment to be negligible. The pilots in all cases gave the microburst alerts 100% credence regardless of the intensity or proximity of the precipitation present. However, the absence of external visual cues in this experiment may have affected the results.

- The positional information inherent in the graphical alert formats was well received by the pilots, allowing them to plan and request a missed approach with lateral maneuvers to completely avoid the event.

- It was observed that the subjects made the decision to execute a missed approach an average of 4.26 nm in advance of encountering a microburst icon positioned on the final approach track.

- The pilots demonstrated a strong tendency to avoid the microburst icons at all cost, even in cases where the icon would be overflown at safe altitudes and airspeeds. This was true even for microburst icons with intensities below the "hazardous" threshold.

The implications of these results for existing and future microburst alerting systems are discussed in Chapter 8.

6. Microburst Alert Generation

6.1 Overview

As described in Chapter 3, the process of alert generation depends strongly on the "hazard criterion" used to quantify the danger microbursts pose to aircraft. In this chapter, results from two studies related to selection of a hazard criterion and its use for alert generation are presented.

Evaluation of Microburst Hazard Criteria. The aviation hazard due to a microburst is a function of both the windfield and pilot/aircraft system characteristics. As such, the microburst aviation hazard is not a directly measureable quantity. A microburst "hazard criterion," however, is a quantity which can be directly measured or inferred from airmass measurements and provides an indication of the microburst aviation hazard. An effective hazard criterion should *correlate well* with the impact of a microburst on an aircraft trajectory. In the first study, this principle was used to compare several possible criteria and identify effective ones.

Determination of Hazard Threshold Values. Once an acceptable hazard criterion has been established, the question that remains is: what value of the hazard criterion should trigger an alert? This question should be answered in the context of aircraft performance. Each alert threshold value should represent a specific level of aircraft trajectory degradation, and be related to recommended or required flight crew operational procedures. Establishing thresholds, therefore, requires knowledge of the direct relationship between hazard criterion values and aircraft trajectory degradation. This relationship is dependent not only on the windfield, but on the aircraft and pilot characteristics and the phase of flight. In the second study, this relationship was established for the specific case of jet transport aircraft on final approach, and used to develop an alert structure based directly on aircraft performance. The alert structure for

this study was based on the three-level iconic scheme preferred by pilots in the graphical display format experiment (Section 5.4).

6.2 Evaluation of Microburst Hazard Criteria

6.2.1 Methodology

A batch aircraft simulation technique was developed to compare several possible microburst hazard criteria. The major steps in the technique are outlined below, and described fully in the following sections.

1) Define a nominal microburst encounter situation. This includes specification of aircraft characteristics, pilot/autopilot characteristics, phase of flight, and initial conditions.

2) Define a "microburst impact parameter," a quantity indicating the effect of the microburst on the aircraft trajectory.

3) Select a set of possible microburst hazard criteria.

4) Establish a test ensemble of microburst windfields for use in evaluation.

5) Simulate the nominal microburst encounter for each windfield in the ensemble.

6) Compute the hazard criteria for each windfield in the ensemble.

7) Compute the microburst impact parameter for each simulation run.

8) Compute the linear correlation coefficient between each hazard criterion and the microburst impact parameter for the complete set of simulation runs (one run for each windfield in the ensemble).

The resulting linear correlation coefficients are indications of the "goodness" of each of the candidate hazard criteria. Note that "correlate well" as used to evaluate the effectiveness of hazard criteria has been specialized here to mean good *linear* correlation. Linearity is a desirable characteristic for simplicity in applying the hazard criterion. If the linear correlation coefficient is close to 1, the hazard criterion is closely related to the aircraft trajectory degradation caused by the microburst. If it is close to zero, it is not related.

The above procedure was accomplished for the two major types of hazardous microburst encounter: (1) approach to landing, and (2) takeoff. Note that values for the candidate hazard criteria were computed assuming that perfect measurements of microburst characteristics were available. The measurement task itself will be addressed in the following chapter.

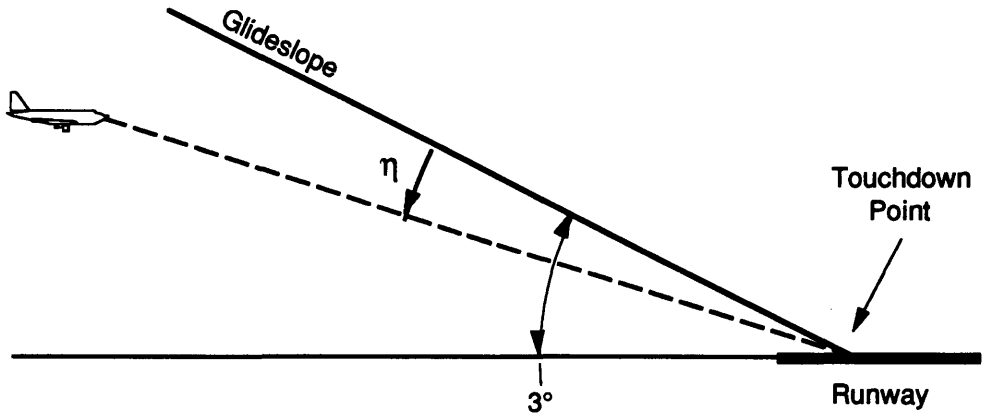

Figure 6.1. Aircraft on ILS Landing Approach. The angles in the figure are not to scale.

6.2.2 Microburst Impact on Landing Approach

For approach to landing, the aircraft was assumed to be executing an Instrument Landing System (ILS) approach at a constant airspeed (Figure 6.1). For an aircraft on an ILS approach, either descending below the glideslope or losing airspeed constitute hazardous conditions. Therefore, an "Approach Degradation" (AD) parameter (similar in concept to those used by McCarthy, et. al. [1979] and Turkel, et. al. [1981]) was defined which combines both angular glideslope deviations (η) and airspeed (V) changes:

$$AD \equiv \sqrt{K_1 \left(\frac{\eta}{0.7°}\right)^2 + K_2 \left(\frac{V_{ref} - V}{V_{ref} - V_{ss}}\right)^2} \tag{6.1}$$

$$\text{where } K_1 = \begin{cases} 1, & \eta < 0 \\ 0, & \eta \geq 0 \end{cases} \qquad K_2 = \begin{cases} 1, & V < V_{ref} \\ 0, & V \geq V_{ref} \end{cases} \tag{6.2}$$

V_{ref} is the reference (nominal) approach airspeed, and V_{ss} is the "stick shaker" airspeed*. To develop this measure, it was assumed that a critical situation develops if either (1) the aircraft drops two "dots" (0.7°) below the glideslope**, or (2) the aircraft's airspeed drops to the "stick shaker" airspeed. Thus, either of these situations constitute a "unit hazard." The root-mean-square of the fractional hazards due to falling below the glideslope or losing airspeed is a point measurement of the approach degradation. Note that only deviations below glideslope or below reference airspeed are taken into account. The angular error vs. glideslope measurement was chosen rather than altitude error to emphasize the increased danger due to being below glideslope at lower altitudes.

Since the success of an ILS approach requires that the aircraft be established and stabilized on the glideslope for several miles before landing, AD is integrated over the entire approach to produce an overall "microburst impact parameter" MI_{ap}. The simulations were halted when the aircraft would normally initiate a flare maneuver (at an altitude of approximately 100 feet AGL).

$$MI_{ap} \equiv \int_{t_0}^{t_{flare}} [AD]\, dt \tag{6.3}$$

Note that MI_{ap} is equivalent to the "J" parameter used in [Wanke and Hansman, 1991]. The initial time, t_0, was chosen well prior to microburst penetration such that $AD(t_0) = 0$. The selection of t_0 then does not affect the value of the integral.

* The "stick-shaker" warns the pilot of impending stall, and the stick-shaker airspeed is normally set to 5-10 knots above the actual stall airspeed.

** Two "dots" of glideslope deviation means that the pilot's glideslope deviation indicator has reached full scale in the low direction, which is the equivalent of falling 0.7° below the 3° glideslope as measured from the runway threshold.

6.2.3 Microburst Impact on Takeoff

For takeoff and climbout, the aircraft does not attempt to track a specific vertical path. Rather, the goal is to maintain a safe airspeed (V) and climb rate ($\dot{h}$). Therefore, the following takeoff degradation (TD) parameter was defined:

$$TD \equiv \sqrt{K_1 \left(\frac{\dot{h}_{nominal} - \dot{h}}{\dot{h}_{nominal}} \right)^2 + K_2 \left(\frac{V_{nominal} - V}{V_{nominal} - V_{ss}} \right)^2} \tag{6.5}$$

$$\text{where } K_1 = \begin{cases} 1, & \dot{h} < \dot{h}_{nominal} \\ 0, & \dot{h} \geq \dot{h}_{nominal} \end{cases} \qquad K_2 = \begin{cases} 1, & V < V_{nominal} \\ 0, & V \geq V_{nominal} \end{cases} \tag{6.6}$$

The nominal values were computed from a takeoff simulation with no winds present, and indexed as a function of altitude AGL. Again, TD is only non-zero when the airspeed or climb rate are <u>below</u> the nominal values for a given altitude. As for the approach case, TD was integrated over the trajectory, from the time of rotation (when the aircraft first leaves the runway) until the time when the aircraft reaches an altitude of 2000 feet AGL:

$$MI_{to1} \equiv \int_{t_{rotation}}^{t_{h = 2000 \text{ ft AGL}}} [TD]\, dt \tag{6.7}$$

Since the aircraft is not attempting to stabilize on a specific trajectory, the integrated TD is a less compelling measure of aircraft performance loss than integrated AD is for approaches. During the climbout, it is a critical situation if the aircraft achieves zero climb rate or approaches stall at any time. Therefore, the maximum value of TD achieved was also tabulated as a second takeoff microburst impact parameter:

$$MI_{to2} \equiv \max [TD] \qquad \text{for } 0 < h < 2000 \text{ feet AGL} \tag{6.8}$$

6.2.4 Candidate Hazard Criteria

There are several possible microburst hazard criteria based on wind measurements. The following were chosen for evaluation:

1) Maximum horizontal velocity change, ΔV or "delta-V" (headwind-to-tailwind change across the event)
2) Mean shear, ΔV/ΔR, defined as total velocity change divided by the shear distance, the distance between the headwind and tailwind peaks
3) Peak F-factor
4) Largest mean F-factor over a given distance (1500, 3000, 4500, 6000 foot lengths were tested)

"Delta-V," as mentioned above, is the criterion currently used in TDWR operational evaluations for both alert thresholds and intensity reporting. Mean shear is an alternative criterion which could be easily computed from TDWR or Doppler sensor measurements. It is obtained by dividing DV by the radial distance across which it is measured. These two criteria are illustrated in Figure 6.2.

The F-factor criterion is based on the impact of a microburst windfield on the total

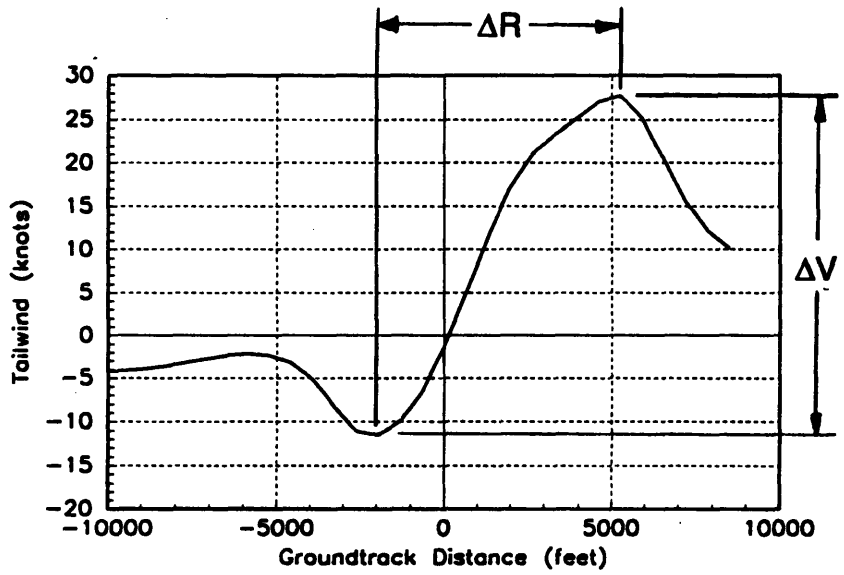

Figure 6.2. Horizontal wind change (ΔV) and mean shear (ΔV/ΔR) criteria. This is a typical plot of horizontal wind vs. ground track distance for a constant-altitude path through a microburst.

energy (kinetic plus potential) of the aircraft. It is a direct measure of the loss of potential rate-of-climb (or loss of effective thrust-to-weight ratio) due to the immediate windfield. It is dependent on the time rate of change in the aircraft frame of the horizontal (tailwind positive) velocity $\dot{W}_x$, the vertical wind velocity W_h, and the aircraft airspeed V. F is described in Section 2.1.2.

$$F \equiv \frac{\dot{W}_x}{g} - \frac{W_h}{V} \tag{6.9}$$

F-factor is a natural measurement for reactive sensors based on inertial instruments, since all of the parameters can be directly measured. Doppler sensors, however, must infer F since the vertical winds cannot be directly measured. Forward-looking infrared systems under development also infer F, estimating it from an empirical relationship between F and the temperature gradient sensed along the aircraft flight path.

The "largest mean F-factor over a given distance" is computed by taking a running average of F-factor over a specified distance along the aircraft trajectory. The largest average value is selected as the hazard rating. Since F is an instantaneous measurement, this effectively aggregates the total performance loss over the specified distance. This was done for averaging windows of four different lengths.

6.2.5 Microburst Windfields

The microburst wind data used to test the criteria was generated by the Terminal Area Simulation System (TASS) developed by Proctor [1987]. It is a detailed computational model of a multiple microburst event which occurred at Denver-Stapelton airport on July 11, 1988. This event caused one near accident and a total of five aircraft to make missed approaches (see Section 2.5.2). Data from five specific times during this event was available, and 12 paths through various parts of the windfield at different times were selected for analysis. These paths all penetrate the approximate center of at least

one microburst, and vary in total horizontal velocity change (at 300ft AGL) from 42 to 70 knots. Shear distances, measured from peak headwind location to peak tailwind location, vary from 6592 feet to 20000 feet. Figure 6.3 illustrates one of the horizontal velocity fields from the TASS model and some of the paths used.

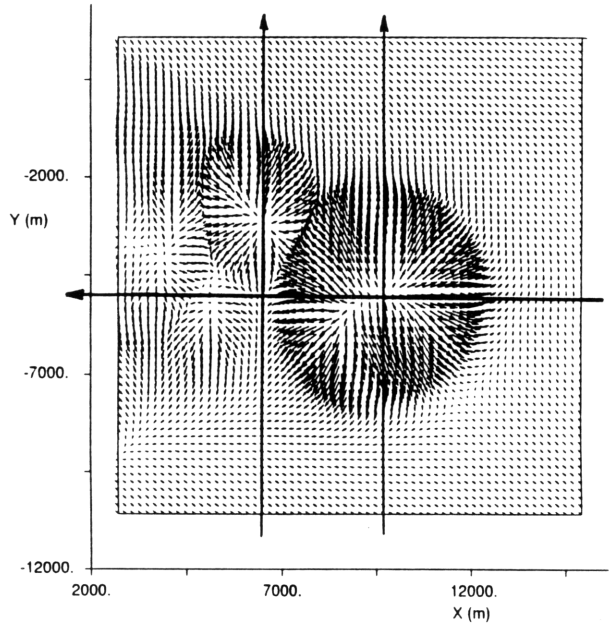

Figure 6.3. TASS windfield for 7/11/88 at 2212.75 UTC. This is a vector plot of the horizontal winds at 271 feet AGL. The lines indicate three of the paths used in the simulation runs.

6.2.6 Aircraft Characteristics and Simulation

Equations of Motion. The aircraft/microburst interaction simulation was based on longitudinal point-mass equations of motion in wind axes, which describe flight in a vertical plane with no short-period pitching dynamics. The aircraft data used (provided by NASA Langley Research Center, and used by Hinton [1990]) was for a Boeing 737-100 aircraft, and included non-linear curve fits for C_L and C_D as functions of angle-of-attack, flap position, and gear position. The equations of motion are:

$$\dot{V} = \frac{T}{m}\cos\alpha - \frac{D}{m} - g\sin\gamma_a - \dot{W}_x\cos\gamma_a - \dot{W}_h\sin\gamma_a \tag{6.10}$$

$$\dot{\gamma}_a = \frac{1}{V}\left[\frac{T}{m}\sin\alpha + \frac{L}{m} - g\cos\gamma_a + \dot{W}_x\sin\gamma_a - \dot{W}_h\cos\gamma_a\right] \tag{6.11}$$

$$\dot{x} = V \cos \gamma_a + W_x \tag{6.12}$$

$$\dot{h} = V \sin \gamma_a + W_h \tag{6.13}$$

$$\alpha = \theta - \gamma_a \tag{6.14}$$

$$C_L = f(\alpha, \text{flaps, gear position}) \tag{6.15}$$

$$C_D = f(\alpha, \text{flaps, gear position}) \tag{6.16}$$

Approach Modeling. The approach controller was a two-loop system (Figure 6.4). The inner-loop controller was designed to control airspeed and flight path angle, and took the form of a fully coupled proportional-plus-integral cascade compensator. Feedback gains were determined by an eigenstructure assignment technique. An outer loop was then used to track the glideslope by commanding flight path angle. Two versions of the outer loop (glideslope tracking) compensator were used, in order to examine the effect of control strategy on the correlation results.

Controller A used simple gain feedback, and produced a fairly slow response. Controller B used a dynamic compensator which produced a faster response, and tended to weight glideslope deviations more heavily than airspeed deviations. The "slow" controller (A) had a dominant mode natural frequency of approximately 0.1 rad/sec,

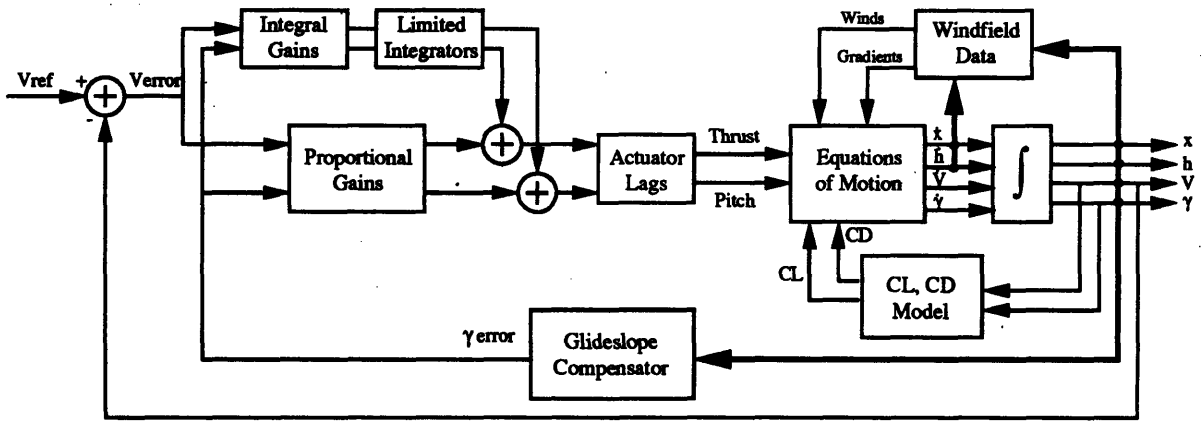

Figure 6.4. Simulation block diagram for approach

Table 6.1. Glideslope tracking autopilot characteristics.

Autopilot	Compensation Type	Dominant mode characteristics	
		Damping Ratio	Frequency, rad/sec
A	Gain	0.65	0.16
B	Lead compensation	0.78	0.38

while the "fast" controller had a dominant mode natural frequency of approximately 0.4 rad/sec (Table 6.1). Further details of these controllers and the 737-100 model data are included in Appendix B.

Takeoff Modeling. The takeoff control laws were considerably simpler than the approach control laws. The aircraft was initially positioned on the runway at rest. The takeoff roll was executed at maximum rated thrust with a pitch angle of 8°. A simple model of tire/runway friction was included. When rotation speed V_r was reached, the climbout pitch angle (typically 18°-20°) was commanded. This pitch angle was held for the duration of the climbout phase, unless the stick shaker angle-or-attack was reached in which case the pitch angle was lowered to prevent stall onset. The simulation terminated when the aircraft reached an altitude of 2000 feet AGL. The climbout pitch angle was set to trim the aircraft at an airspeed of V_r + 15 knots.

Initial Conditions: Approach. For each windfield, an approach was made such that the aircraft penetrated the core of the microburst at a specified distance from the desired touchdown point. Two distances were used: (1) 8000 feet from touchdown (glideslope altitude of 420 feet) and (2) 15000 feet from touchdown (glideslope altitude of 785 feet). The aircraft was trimmed for a 3° ILS approach at 148 knots with landing gear extended and flaps set at 25°. The available thrust was limited to approach maximum, which results in a maximum thrust-to-weight ratio of approximately 0.17. As stated above, it was assumed that the pilot or autopilot was unaware of the presence of the microburst. Thus, no microburst escape maneuvers were executed.

Sample results from one of the approach simulation runs are shown in Figure 6.5. The dashed lines on the altitude and airspeed charts represent the nominal approach trajectory. Note that the aircraft first encounters a headwind and slight updraft. This produces a slight airspeed increase, which causes the autopilot to command idle thrust (at 70 to 80 seconds). This is followed by a downdraft and a rapid transition from headwind to tailwind as the aircraft passes through microburst core (80 to 110 seconds). During this time the airspeed drops to 128 knots, and the aircraft drops considerably below glideslope. The autopilot commands a high pitch angle and maximum available thrust is response to these deviations. Finally, the tailwind drops off and the aircraft finishes the run at high airspeed and well above the glideslope.

Initial Conditions: Takeoff. For the takeoff cases, the microburst core was positioned 6000 feet from the takeoff roll initiation point. In this position, the aircraft entered the hazardous wind shear region at approximately the rotation point. The aircraft gross weight was set at the takeoff maximum of 97,000 lbs. Maximum rated thrust was 24,000 lb st., yielding a thrust-to-weight ratio of 0.247.

Sample histories from one of the takeoff runs are shown in Figure 6.6. Again, the nominal altitude and airspeed curves are shown as dashed lines. Note that the headwind is encountered during the takeoff roll, resulting in a slightly shorter takeoff roll than for the nominal case. Immediately after takeoff, the airspeed starts to drop as the aircraft passes through the shear region. The effect of the microburst is also visible in the climb rate plot as a sharp drop-off at 50 to 70 seconds. At 70 seconds, the aircraft leaves the core and the airspeed and climb rate rapidly recover to normal values.

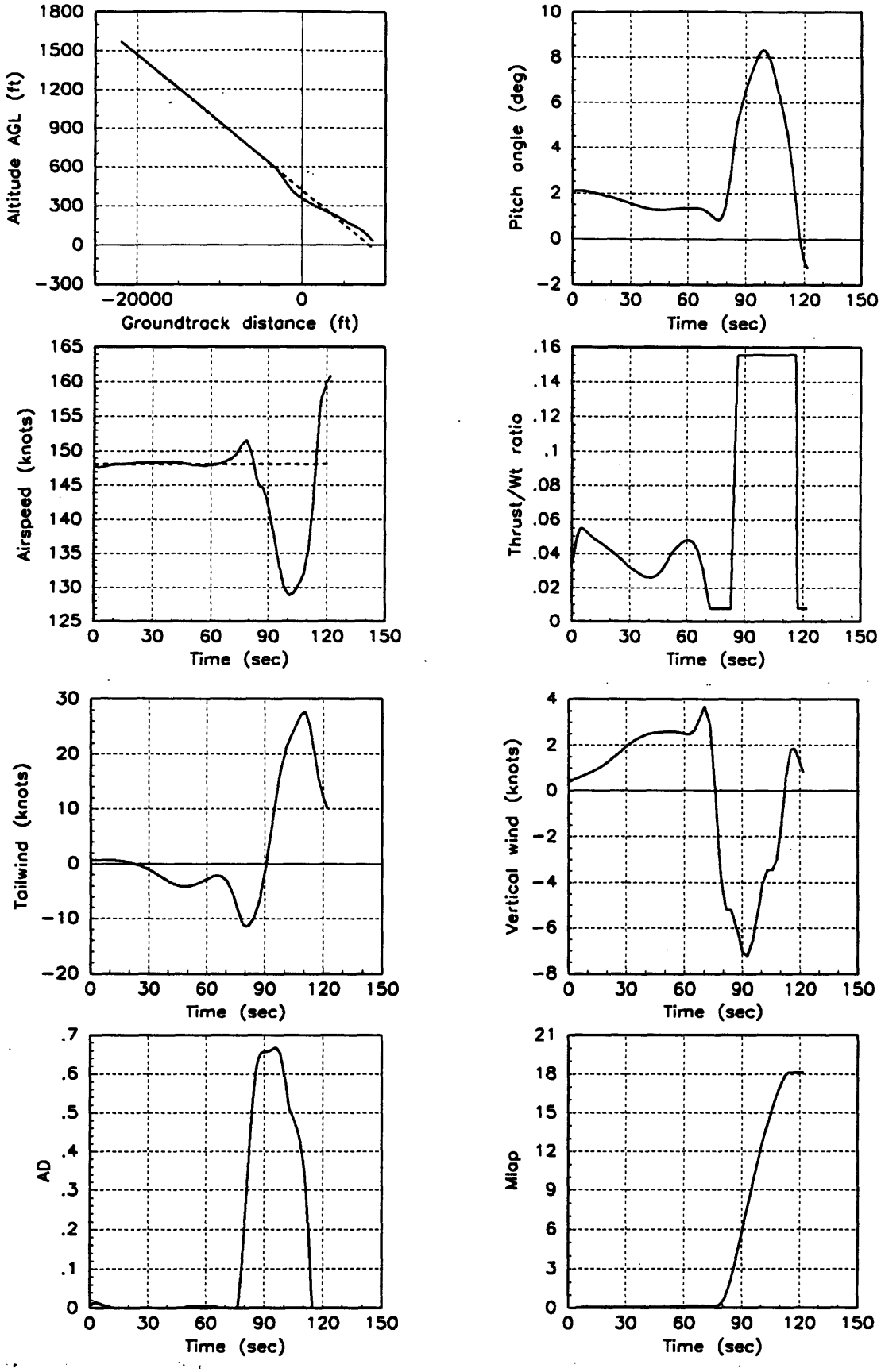

Figure 6.5. Sample results for an approach simulation run. In the above case, autopilot A was active. The aircraft was initially positioned 5 nm from touchdown at an approach speed of 250 ft/sec (148 knots)

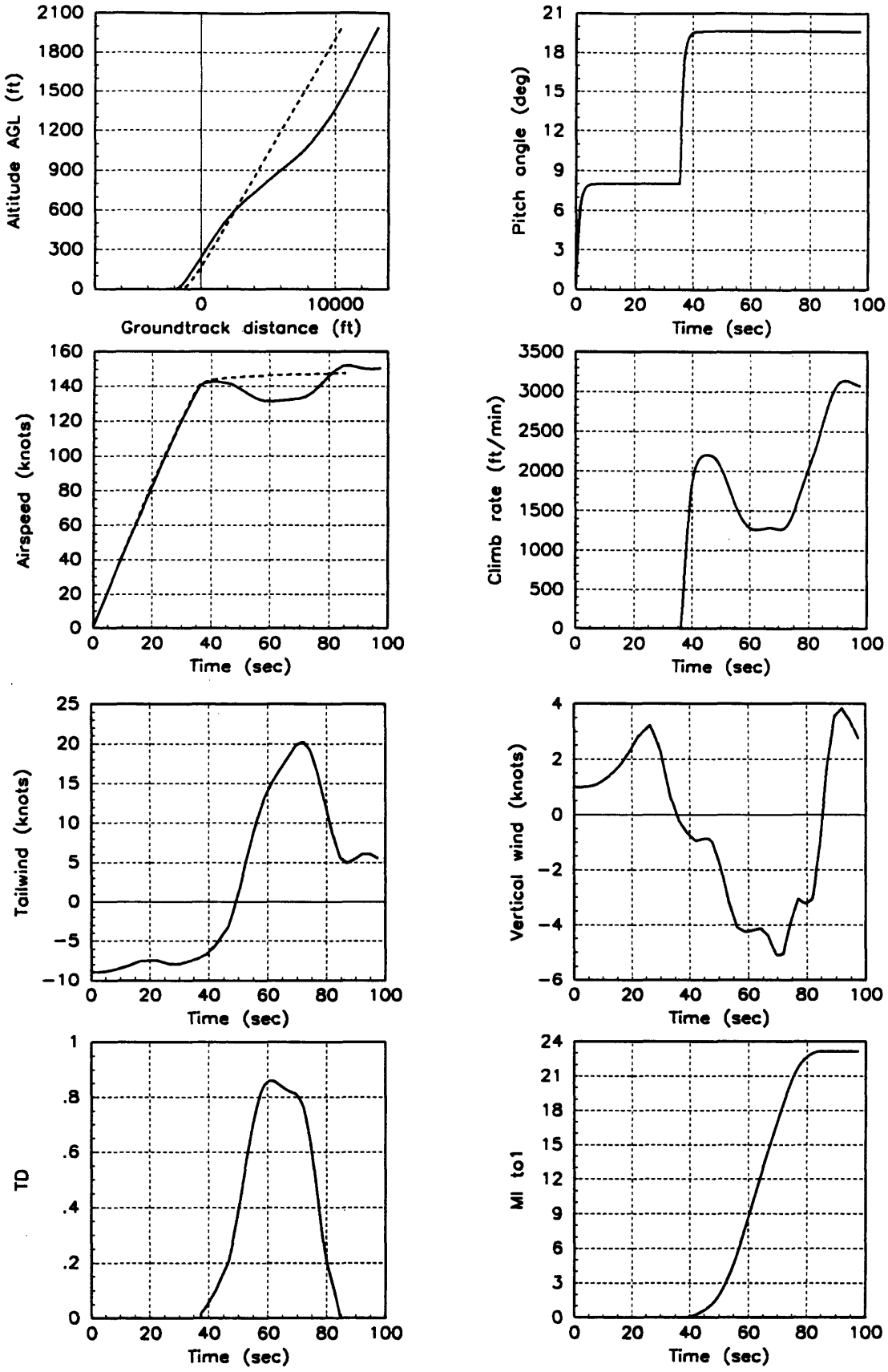

Figure 6.6. Sample results for a takeoff simulation run.

Implementation. The simulations were run on a Sun 3/80 workstation using $MATRIX_X$ SYSTEM_BUILD software by Integrated Systems, Inc. This package allowed simulation of non-linear systems through a graphical user interface based on block diagrams.

6.2.7 Results and Discussion

The primary result of each simulation run was the value of MI, the microburst impact parameter. The hazard criteria were then applied to each windfield. ΔV and mean shear were computed from a 300 foot AGL path through the windfield along the approach path, to simulate a TDWR-like measurement. F-factor criteria were computed from the F-factor history experienced by the simulated aircraft. A linear correlation analysis was then performed for each of the hazard criteria vs. MI.

Approach Results. Four sets were run in total, varying the glideslope controller (A, B) and the position of microburst core encounter (8000 feet and 15000 feet from touchdown). Scatter plots of the microburst impact parameter vs. several of the hazard criteria for one of the run sets are presented in Figure 6.7. The plot at upper left illustrates the poor correlation between ΔV and the microburst impact parameter, with a correlation coefficient of 0.484. Mean shear, however correlated quite well (upper right, coefficient = 0.880) as did F-factor averaged over 3000 feet (lower right, coefficient = 0.752). The peak F results appear generally good, but two points lie fairly far off the linear fit and produce a lower correlation coefficient (0.684).

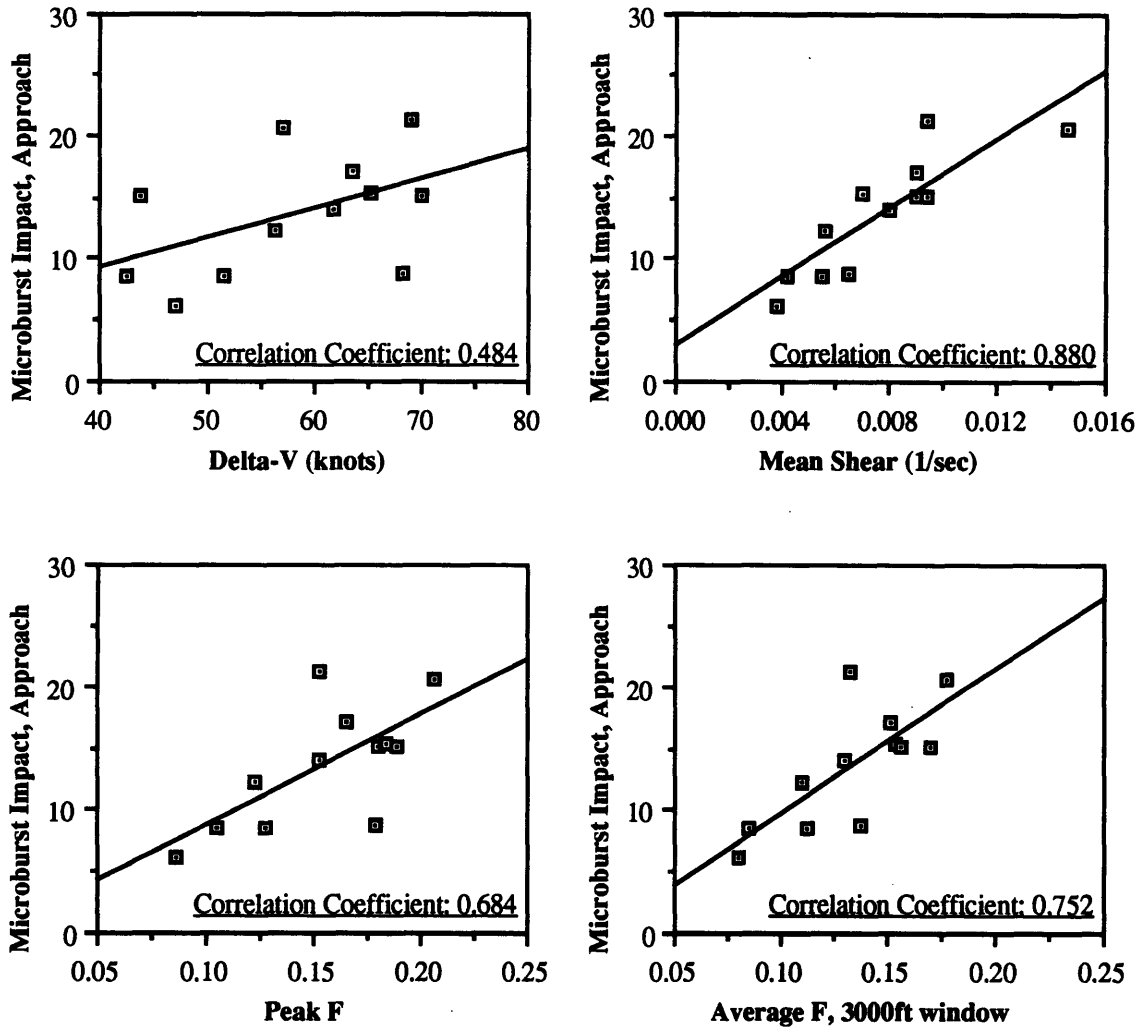

Figure 6.7. Approach cases: Microburst impact parameter vs. several hazard criteria. This set of runs used autopilot A and the microburst core was encountered at 8000 feet before touchdown.

Table 6.2 summarizes the correlation results for all four sets of approach runs. As shown above in the example plot, the delta-V criterion correlated poorly with the microburst impact parameter, yielding coefficients between 0.47 and 0.59. Mean shear correlated well, with coefficients as high an 0.88 for the 8000 ft runs. Peak F does not correlate as well, and results are inconsistent between run sets. This is due to localized high-F regions in the windfields which do not cause much performance degradation. F-factor averages provided reasonably good correlation in all cases, and the results were not strongly dependent on the averaging window length. The results for the low altitude

Table 6.2. Approach cases -- Linear correlation coefficients between the microburst impact parameter MI_{ap} and each of the candidate hazard criteria for 4 sets of runs. The heading of each column indicates autopilot used (A or B) and distance of the microburst core from the runway threshold.

Hazard Criterion	Linear Correlation Coefficient, ρ, with MI_{ap}			
	AP A, 8000 ft	AP B, 8000 ft	AP A,15000 ft	AP B, 15000 ft
Delta-V	0.484	0.472	0.520	0.583
Mean Shear	0.880	0.883	0.812	0.762
Peak F-factor	0.684	0.820	0.413	0.453
Max F averaged over:				
1500 feet	0.702	0.827	0.630	0.653
3000 feet	0.752	0.870	0.662	0.692
4500 feet	0.768	0.882	0.728	0.744
6000 feet	0.739	0.834	0.747	0.754

penetrations were slightly better than for the high altitude penetrations. Also, larger window lengths appeared to do better in the higher altitude penetrations.

The fact that mean shear had higher correlation with microburst impact than delta-V is not surprising, since the wind shear threat is due to loss of energy from both rapid change in horizontal wind velocity and from vertical wind velocity (downdraft). Both the magnitude of the headwind change and the time or distance over which it changes are important, and mean shear indicates the average *rate* of headwind to tailwind change. Also, due to mass continuity, the magnitude of the downdraft is related to the rate of headwind change. Therefore, the mean shear value in some sense also accounts for the downdraft hazard component.

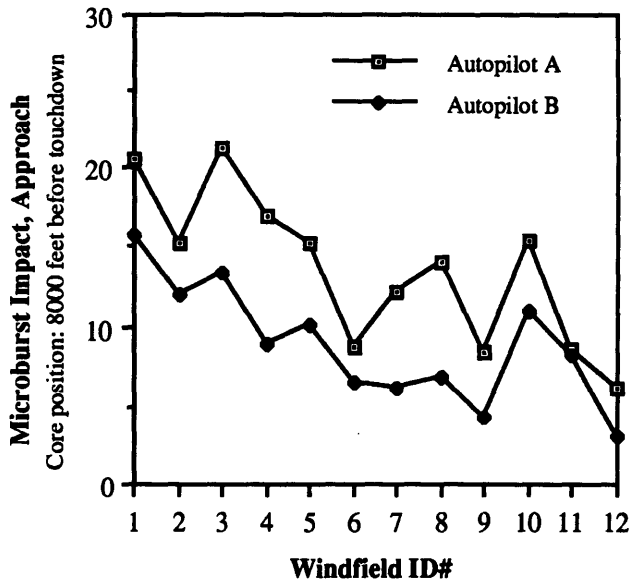

Figure 6.8. Microburst impact parameter MI_{ap} for each windfield, for the two glideslope controllers. The microburst core is located 8000 feet before the touchdown point. Note that autopilot A was the low bandwidth controller, and autopilot B was the high bandwidth controller.

The control strategy used did not have a strong impact on the correlation results, which can be seen by comparing the autopilot A columns with the autopilot B columns in Table 6.2. Correlations were slightly better with the higher bandwidth controller (B), since the aircraft spent less time in thrust or angle-of-attack limit conditions. The faster controller produced lower values of MI_{ap} for all of the approaches (Figure 6.8). These results indicate that the final magnitude of MI (and hence the hazard) depends on the control strategy employed, but hazard criteria which correlate well with the microburst impact parameter for one control strategy will still correlate well for another strategy. A similar effect would most likely be seen when comparing results for aircraft with differing performance capabilities, although this was not tested.

Takeoff Results. For the takeoff runs, the microburst core was positioned 6000 feet from the takeoff roll initiation point. In this situation, the aircraft encountered the shear region just after rotation. Scatter plots of MI_{to1} (integrated takeoff degradation) and

MI_{to2} (peak TD) vs. several hazard criteria are included in Figures 6.9 and 6.10, and Table 6.3 includes the correlation coefficients for both microburst impact criteria.

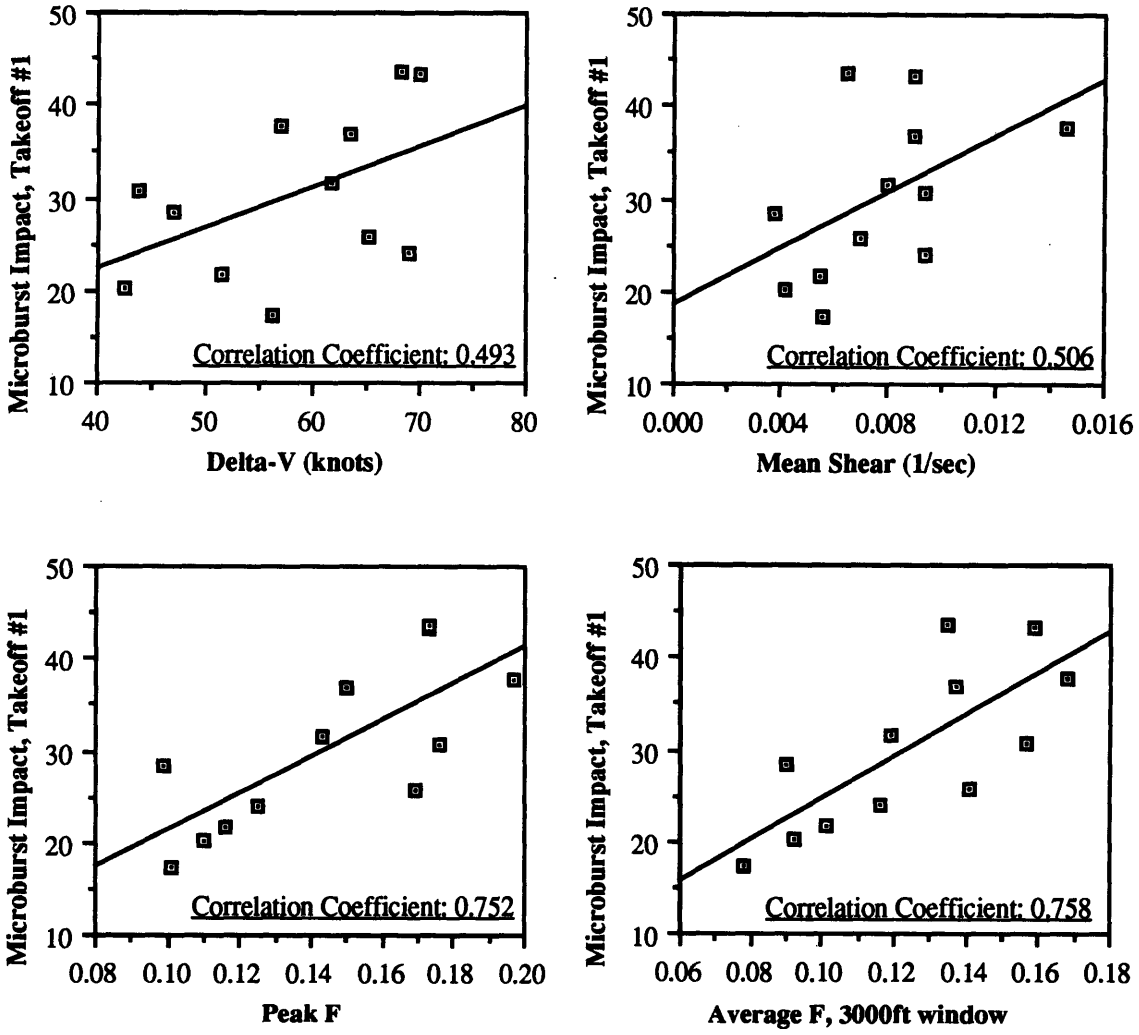

Figure 6.9. Takeoff cases: Microburst impact parameter MI_{to1} vs. several hazard criteria. The microburst core was encountered 6000 feet from the takeoff roll initiation point.

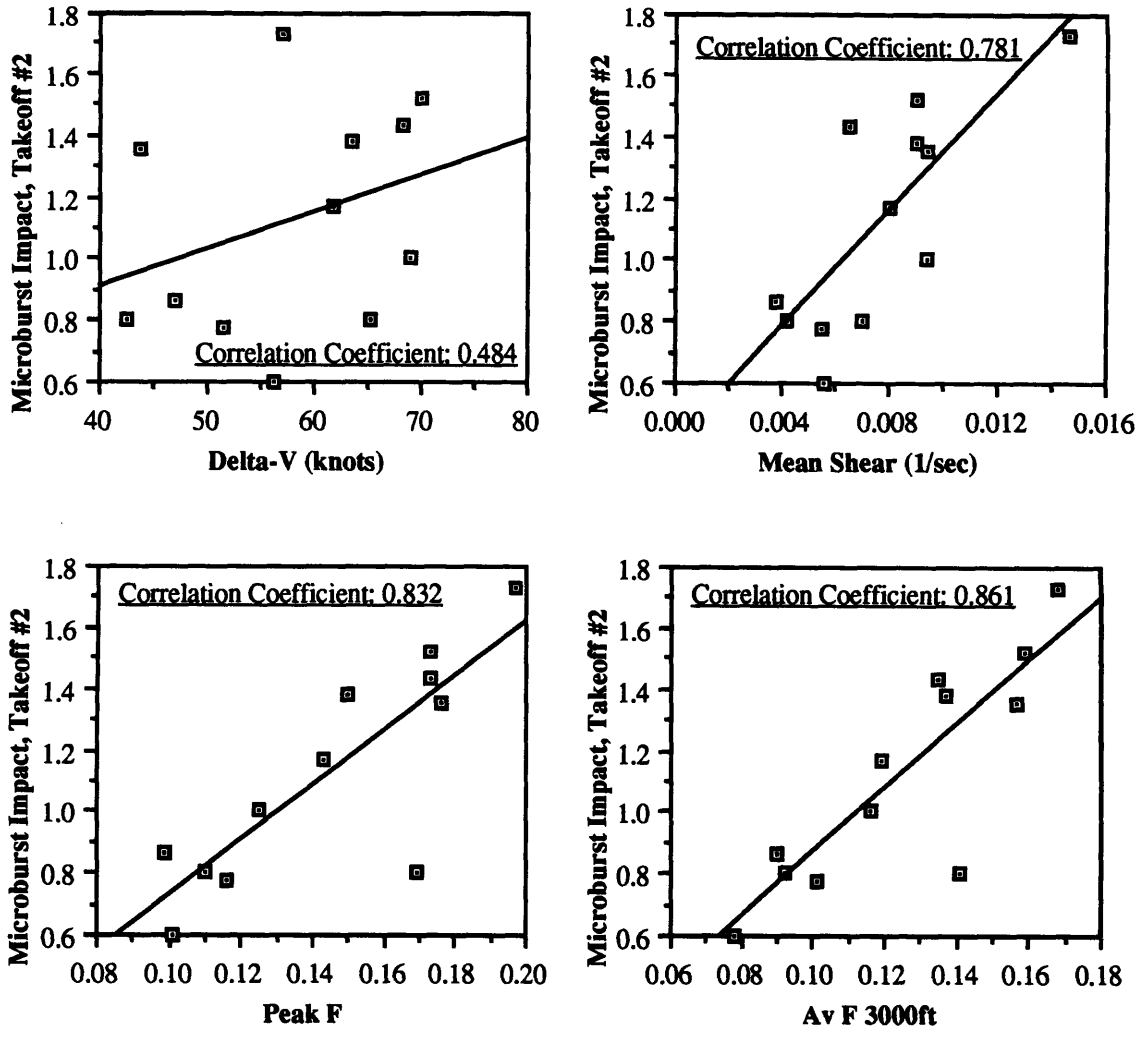

Figure 6.10. Takeoff cases: Microburst impact parameter MI_{to2} vs. several hazard criteria. The microburst core was encountered 6000 feet from the takeoff roll initiation point.

Table 6.3. Takeoff cases -- Linear correlation coefficients between the microburst impact parameters MI_{to1} and MI_{to2} for each of the candidate hazard criteria.

Hazard Criterion	Linear Correlation Coefficient, ρ, with: MI_{to1} (integrated TD)	MI_{to2} (maximum TD)
Delta-V	0.493	0.329
Mean Shear	0.506	0.781
Peak F-factor	0.752	0.832
Max F averaged over:		
1500 feet	0.772	0.855
3000 feet	0.758	0.861
4500 feet	0.801	0.895
6000 feet	0.850	0.938

As for the approach cases, delta-V correlated poorly and the F-factor criteria correlated fairly well. Once again, the F-factor averaging window size did not appreciably affect the results. Mean shear, however, did not correlate very well with the integrated TD parameter (MI_{to1}). It did correlate better with the peak TD parameter (MI_{to2}). Note that mean shear was evaluated from a *constant-altitude* path through the *entire* windfield. During climbout, the aircraft is changing altitude much more rapidly than during landing approach, and the mean shear through the windfield changes significantly with altitude. Also, F-factor, since it includes both horizontal shear and downdraft components, does *not* vary strongly with altitude. This altitude effect may account for the poor correlation of mean shear with integrated TD.

6.2.8 Analysis Limitations

Before drawing conclusions from the above analysis, some limitations should be discussed. The most important is that all the microburst windfields analyzed came from a single day (in fact, all within 10 minutes) due to the limited amount of high-resolution windfield model data available. Although a fairly well distributed set of microburst intensities and sizes were available in this data set, the results may be biased by some feature of the TASS model or by characteristics particular to the meteorological conditions on the day simulated.

A further limitation is that a single aircraft model of a fairly small transport aircraft was used. Use of a different transport aircraft model or a different pilot or autopilot model would clearly result in different values of the microburst impact parameter. The higher-bandwidth glideslope tracking strategy, for example, lowered the final MI_{ap} value for all approach runs. This did not, however, significantly alter the correlation results, since the difference in approach tracking due to the different control strategy was roughly the same for all microburst encounters. Using a different transport aircraft model would probably have a similar effect. It is interesting to note that the

major control tradeoff available from an energy standpoint is whether airspeed deviations or altitude deviations are weighted more heavily. The microburst impact parameters include both of these deviations.

Also, perfect measurement of the windfield was assumed, and the evaluation of the hazard criteria did not include any measurement limitations. For example, the measurement of delta-V and mean shear at 300 feet AGL was done to "simulate" a ground-based radar like TDWR, but did not account for measurement details such as averaging across the radar beamwidth. Similarly, F was taken from the aircraft state and wind history after the simulation run, and not from a simulation of an actual airborne sensing system.

Finally, it should be noted that in some past wind shear related accidents (the crash of Delta 191 at DFW in 1985, for example [Fujita, 1985]) there were short-scale pitching and rolling motions of large enough amplitudes to considerably affect the controllability and performance of the aircraft. These disturbances are not considered by any of the hazard criteria, and were not present in the modeled windfields.

6.2.9 Conclusion

A methodology for evaluating microburst hazard criteria has been developed, based on batch flight simulations of aircraft on approach or takeoff through microburst windfields. Measures of the impact of a microburst on an aircraft's trajectory have been defined, including both airspeed losses and altitude or climb rate deviations. Hazard criteria were evaluated by calculating the linear correlation coefficient between values of several hazard criteria and values of microburst impact parameters for a series of simulation runs through an ensemble of microburst windfields.

A preliminary evaluation of a selected set of hazard criteria has been performed. The results indicate that the total headwind change along the aircraft flight path ("delta-

V", the criterion currently used by TDWR) does not correlate well with the flight path degradation caused by microbursts. However, the "mean shear," computed by dividing the "delta-V" by the distance over which it occurs, correlates well with microburst impact for approach cases. It does not, however, correlate as well for the takeoff condition. Averaging the "F-factor" hazard criterion (a measure of the aircraft total energy loss caused by the windfield) over certain distances proved to be an effective predictor of microburst impact for *both* approach and takeoff encounters. The F-factor criterion, however, requires knowledge of both horizontal and vertical winds, which may be difficult for some sensors. Finally, it was found that the correlation results obtained from approach runs using two different autopilot models were not significantly different, although the absolute levels of microburst impact did differ.

6.3 Determination of Hazard Threshold Values

6.3.1 Methodology

The work in Section 6.2 identified hazard criteria which correlate well with aircraft trajectory degradation caused by microbursts. In this section, a technique for establishing alerting thresholds based on a microburst hazard criterion is presented. The case of jet transport aircraft encountering a microburst on approach is used as an example. The procedure uses the following steps:

1) Select a good hazard criterion. Based on the results presented in Section 6.2, F-factor averaged over 1 km (3281 feet) was chosen.

2) Define a trajectory degradation parameter. This measure is similar to the microburst impact parameters used in Section 6.2, but is related more directly to recommended crew procedures. For this case, landing approach, it is based on criteria for aborting the approach.

3) Establish a multi-level alert structure based directly on values of the trajectory degradation. Threshold values of trajectory degradation can be more directly related to recommended crew procedures than values of a microburst hazard criterion.

4) Establish a worst-case microburst encounter scenario. This involves positioning of the microburst relative to the aircraft's intended flight path.

5) Establish nominal aircraft characteristics. This includes both aircraft performance and flight control system characteristics.

6) Represent the microburst winds by a parametric analytical model. This allows simulation of microbursts with arbitrary size and strength.

7) Simulate the encounter for a wide range of representative microburst sizes and strengths. The microburst model parameters are varied to yield a large range of hazard criterion values.

8) Determine the relationship between values of the hazard criterion and values of the trajectory degradation parameter.

9) Select alert threshold values of the hazard criterion which correspond to the desired alert threshold values of trajectory degradation.

The result of the final step is a set of alert thresholds, based on a *measureable* microburst hazard criterion, for an alert structure based directly on a *non-measureable* trajectory degradation parameter. In this way, a practical alerting scheme tied *directly* to aircraft performance is developed. The above steps are further discussed below.

6.3.2 Selecting the Hazard Criterion

In Section 6.2, F-factor averaged over a distance was found to give good correlation with hazard for all cases tested. Therefore, the hazard thresholds in this study were based on F averaged over 1 km (approximately 3000 feet). The largest value obtained during the simulated microburst penetrations was used to define the strength of each microburst. This value will be henceforth referred to as F_{av}.

6.3.3 Trajectory Degradation Metric for Approach

For an approach under wind shear conditions, the primary flight crew decision is whether or not to abort the approach. According to the *Windshear Training Aid* [FAA, 1987], the following conditions are indicative of hazardous wind shear and necessitate a missed approach:

- ± 15 knots from reference airspeed
- ± 500 feet/minute deviation from nominal vertical speed

- ± 5° from nominal pitch attitude
- ± 1 dot of glideslope angular displacement
- unusual throttle position for a "significant length of time"

To reflect these guidelines, an "abort parameter" was established, similar to the approach degradation parameter used in the previous study:

$$AP \equiv \sqrt{\left(\frac{\eta}{0.35°}\right)^2 + \left(\frac{V_{ref} - V}{15 \text{ knots}}\right)^2} \tag{6.17}$$

where airspeed, V, is measured in knots. Angular glideslope deviation, η, was illustrated in Figure 6.1. One "dot" of deviation equals 0.35°. The abort parameter was based on glideslope and airspeed deviations in order to include both kinetic and potential energy-related components. This decreases the sensitivity of the simulation results to the nominal control strategy chosen. Also, it was not necessary to include the pitch, vertical speed, and throttle conditions explicitly. These were not violated in the simulations without also violating either the airspeed deviation or glideslope displacement conditions. For a given simulated approach, the maximum value of AP induced indicates the level of trajectory degradation due to the microburst, in terms of the need for initiation of a missed approach. Note that the only differences between AP and AD (used in Section 6.2) are the values used to normalize the glideslope and airspeed deviations.

6.3.4 Alert Structure

A three-level alert structure, as used in the graphical microburst alert display experiment (Section 5.4, "Display B") was assumed. In that experiment, the three-level alert display was preferred by the flight crews and found to be a good decision-making tool. A corresponding three-level alert structure, based directly on maximum values of AP that would be experienced during a standard approach, is shown in Table 6.4.

Table 6.4: Three-level alert structure based on the abort parameter, AP.

Alert Level	max AP during approach	Description
1	$0.5 \leq$ max AP < 1.0	"low intensity"
2	$1.0 \leq$ max AP < 1.41	"hazardous"
3	max AP ≥ 1.41	"critically hazardous"

The AP thresholds were chosen by the following rationale. As stated above, AP is based on the principle that either (a) airspeed change of 15 knots, or (b) glideslope error of 1 dot mandates a missed approach. When AP reaches 1.0 (the "hazardous" threshold), this indicates the *possibility* of either of these events occurring. Which event, if either, occurs depends on the control strategy employed, since airspeed can be traded for altitude rate and vice versa. When AP reaches 1.41 (the square root of 2) it is *guaranteed* that one of the missed approach criteria (a), (b) will be exceeded, and a missed approach will be *required.* Therefore, this was chosen as the "critically hazardous" threshold. The objective of this study is then to determine through simulation the hazard criterion values (F_{av}) which produce the AP thresholds in Table 6.4.

6.3.5 Approach Scenario Definition

The study was designed to produce threshold values of F_{av} for jet transport aircraft on final approach. Furthermore, the intent was to produce thresholds which were independent of the microburst position along the approach. Therefore, the microburst was placed to generate a "worst-case" scenario in which the aircraft encountered the hazardous portion of the microburst in the last mile of the approach (Figure 6.11). The microburst center was located 2.0 km from the runway threshold. This scenario is only "worst-case" for microbursts which impact the aircraft before the flare point, when AP is a sensible descriptor of trajectory degradation. It is clearly possible to place a microburst directly at the touchdown point, in which case even a weak microburst could cause an

accident. Therefore, the hazard thresholds which are produced in this analysis are limited to microbursts which occur on the approach but not over the runway.

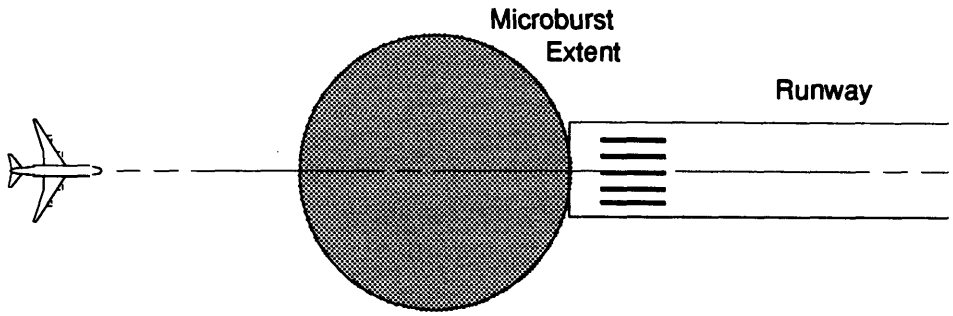

Figure 6.11. Microburst placement on final approach

6.3.6 Nominal Aircraft Characteristics

The aircraft model was designed to represent the primary characteristics of two, three, or four-engine commercial jet transport aircraft at maximum landing weight. The control system was designed to represent a typical autothrottle and glideslope tracking system for a modern transport aircraft. The aircraft model and controller are discussed in greater detail below.

Generic Jet Transport Model. The basic aircraft model used in Section 6.2 was extended to better represent jet transports in general. The same equations of motion and aerodynamic model were used in a normalized form. The normalized form eliminated specific aircraft characteristics (wing surface area, mass, thrust etc.) in favor of ratios such as wing loading and thrust-to-weight fraction. General characteristics of two, three, and four-engine transport aircraft at maximum landing weight were set as shown in Table 6.5.

Table 6.5. Generic jet transport model characteristics

No. of Engines	Wing Loading (lbf/sq. ft.)	Approach Speed (KIAS)	Excess Thrust-to-Weight Ratio
2	95.0	140	0.17
3	95.0	150	0.13
4	95.0	160	0.11

The data for typical approach speeds and excess thrust-to-weight ratio (at the trim condition) was provided by David Hinton of NASA Langley Research Center [1992]. A review of modern transport aircraft wing loading data [Taylor (ed.), 1989] determined that a wing loading of 95 lbf/sq. ft. is representative of all three aircraft classes at maximum landing weight.

Nominal Controller. The selection of a controller for this study was important, since controller characteristics (particularly bandwidth) can affect the magnitudes of airspeed and glideslope deviations. For this reason, a more formal controller design process was applied with the intent of reproducing realistic controller feedback structure and characteristics. The result is illustrated in Figure 6.12.

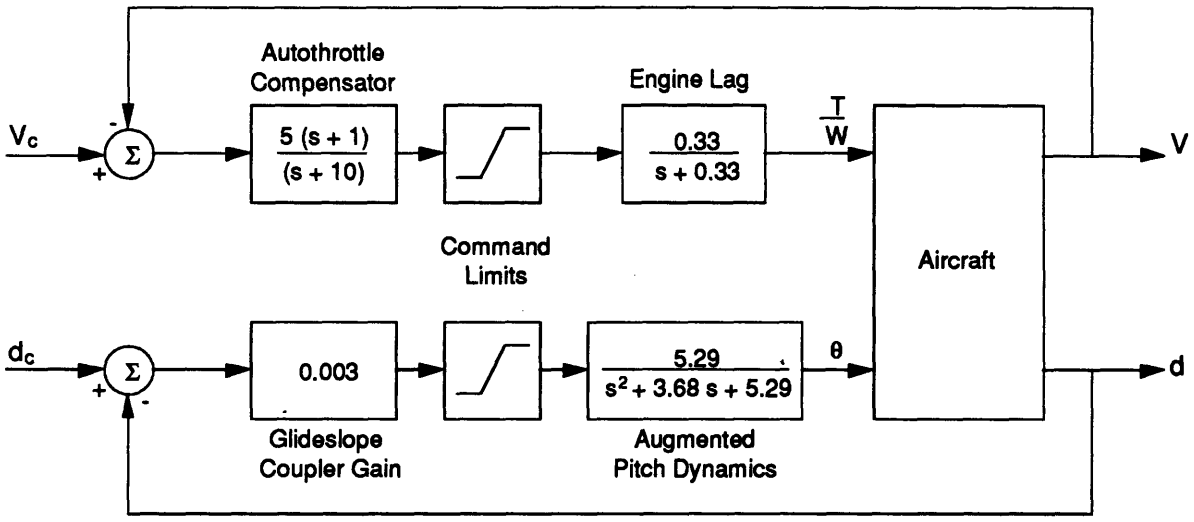

Figure 6.12. Airspeed and glideslope tracking system for the generic jet transport model. Transfer functions in the above diagram are expressed in terms of the Laplace transform frequency variable, s.

The system was designed by successive loop closures, and follows glideslope tracker design procedures as given by McRuer, et. al. [1973] and Stevens and Lewis [1992]. Typically, a pitch attitude command system would be designed first. In both references, the resulting closed loop systems have a second order pitch response with damping ratio of 0.7 to 0.8 and a frequency of approximately 2.5 rad/sec. For the model used here, which neglects pitching dynamics, this loop closure has been assumed and

pitch angle is a control input. Therefore, a second order pitch response to pitch command was added as effective actuator dynamics. Since the analytical model produces smooth wind functions, and the pitching rates are not high, there is little fidelity lost by using a point-mass longitudinal model for the simulations.

The second loop feeds back airspeed error to throttle. The thrust response dynamics were modeled by a first-order lag, with a time constant of 3 sec. Lead compensation was used to close this loop. The dominant mode of the speed loop had a damping ratio of 0.77 and a natural frequency of 1.43 rad/sec.

The third loop feeds back glideslope altitude deviation, d, to pitch command. In the examples given by McRuer, et. al. [1973] and Stevens and Lewis [1992], dynamic compensation is used to close this loop. For the simplified dynamics used here, pure gain feedback was sufficient. The dominant glideslope tracking mode had a damping ratio of 0.76 and a natural frequency of 0.41 rad/sec, which is consistent with the example cases given in both references. The responses to an initial glideslope offset of +50 meters are shown in Figure 6.13. Note that the airspeed variations are small, even for this large initial error.

The thrust command was limited to the available maximum thrust-to-weight ratio and pitch commands were limited by the stick-shaker angle-of-attack. Further details of the aircraft/control system simulation are available in Appendix B.

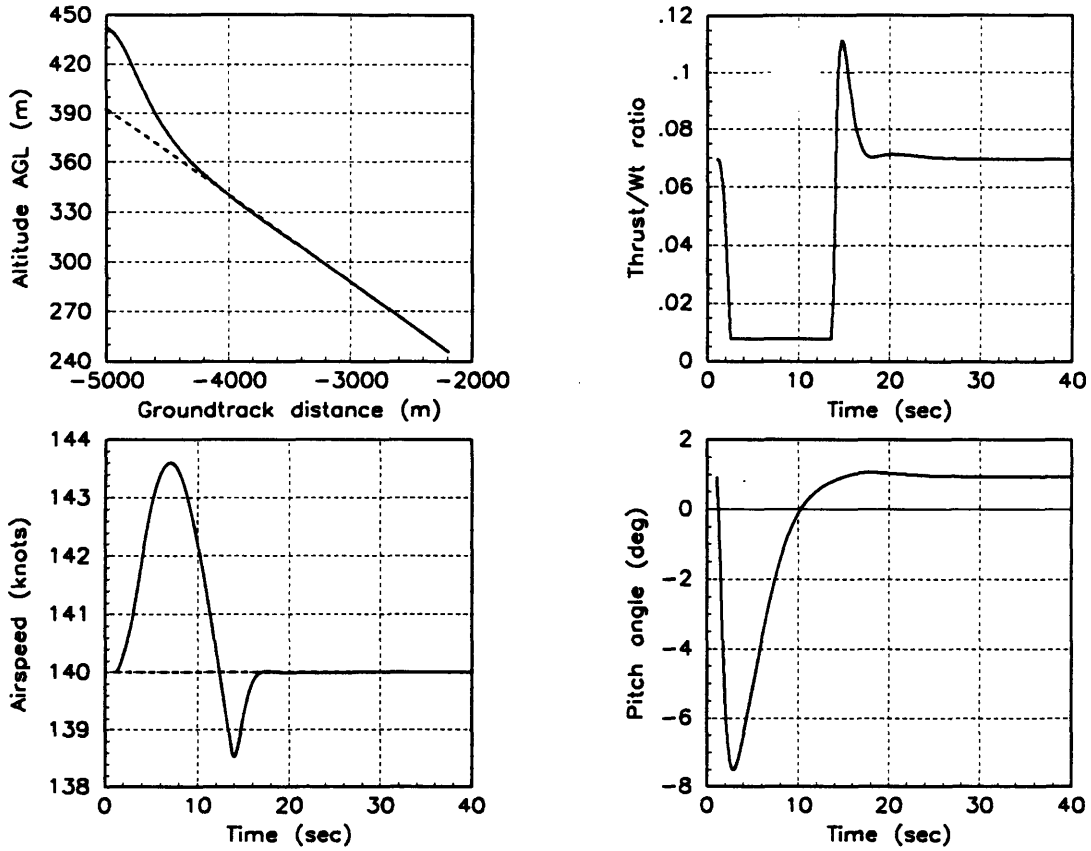

Figure 6.13. Responses to an initial glideslope error of +50 meters. These plots are for the 2-engine jet transport at an approach speed of 140 knots.

6.3.7 Microburst Wind Modeling

Parametric Analytical Model. The analytical microburst model used in this work was initially developed by Oseguera and Bowles [1988] and later improved by Vicroy [1991]. The Oseguera-Bowles-Vicroy (OBV) model uses shaping functions to generate an axisymmetric flowfield which satisfies the mass continuity equation and is representative of the major characteristics of measured microbursts. The windfield is a function of (x, y, h) position and three model parameters: maximum outflow velocity (U_m), microburst core radius (R_p) and the outflow height (Z_m). These variables relate directly to measureable microburst characteristics. The maximum horizontal velocity change across the model microburst is $2 \times U_m$, and the distance between the headwind and tailwind peaks is $2 \times R_p$. The maximum horizontal velocities occur at an altitude of

Z_m. The wind equations are included in Appendix C, and a full set of plots demonstrating the model windfield characteristics are given by Vicroy [1991].

Sample wind plots for a constant-altitude flight path through the microburst center are included in Figure 6.14. The classic microburst signature is evident in the horizontal wind plot, an increasing headwind followed by rapid shear to a tailwind. The downdraft is strongest at the microburst center, and small updrafts are visible at the edges of the outflow region.

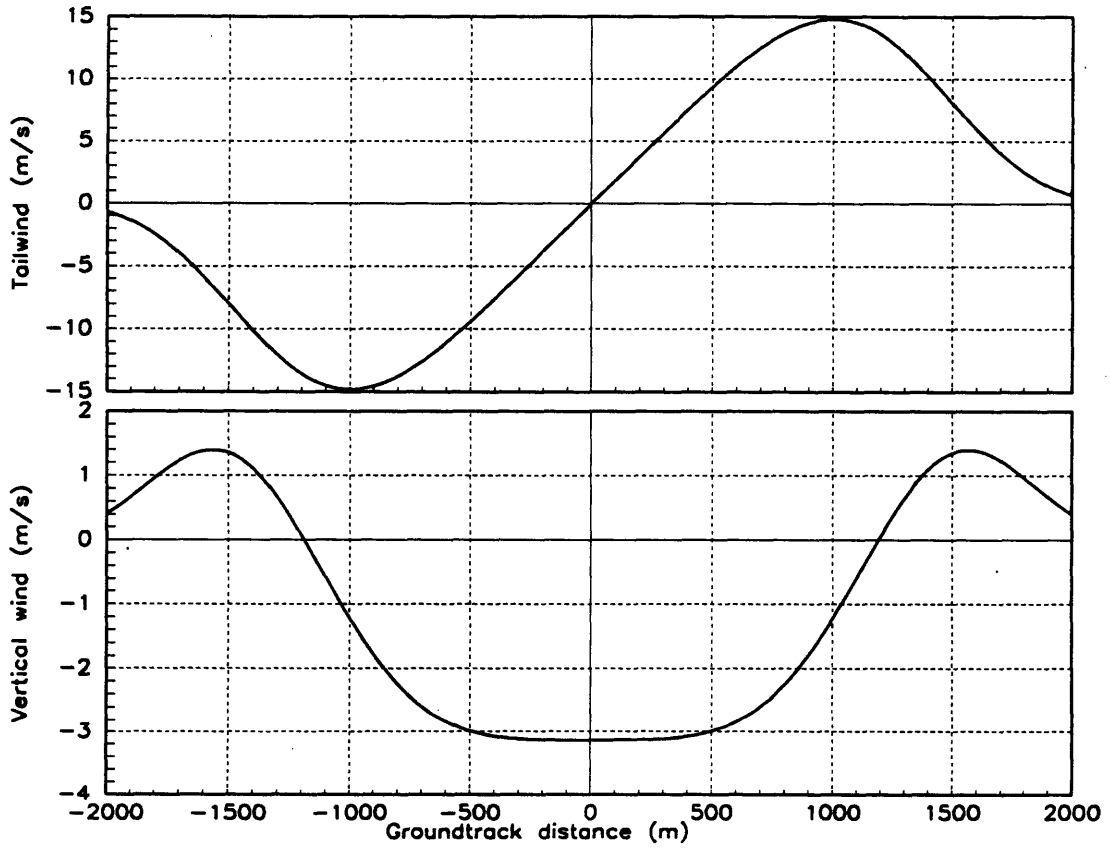

Figure 6.14. Oseguera-Bowles-Vicroy microburst model. Sample winds for a constant-altitude (80 m AGL) flight path through the center of the model microburst. The model parameters for this plot were: U_m = 15 m/s, R_p = 1000 m, Z_m = 80 m.

Microburst Parameter Test Matrix. The purpose of using a parametric model was to produce a set of microbursts with a wide range of F_{av}. For the OBV model, F_{av} can be increased either by increasing U_m or by decreasing R_p. To resolve this ambiguity, R_p

was set to a series of discrete values between 0.5 km and 2 km to represent reasonable microburst sizes. This corresponds to microburst diameters from 1 km to 4 km. Field studies have found that microbursts with diameters less than 1 km are rare [Hjelmfelt, 1988] and microbursts with diameters of greater than 4 km would have to be extremely strong to produce significant F-factors. For each radius, U_m was varied from 2 m/s to 25 m/s. Since U_m reflects one-half of the total delta-V, the delta-V range represented by this set was 4 m/s to 50 m/s (7.8 knots to 97 knots). The 1 km-averaged F-factors achieved ranged from 0.01 to.0.38. Since the outflow height parameter has little effect on F_{av}, Z_m was fixed at a representative value of 80 m AGL for all runs.

Implementation. As in the previous study, the simulation was mechanized on a Sun 3/80 workstation using MATRIX$_x$ SYSTEM_BUILD software by Integrated Systems, Inc.

6.3.8 Simulation Results and Discussion

Each set of microburst model parameters was used in one simulation run. For each run, F_{av} and the maximum value of AP were computed. The simulation results therefore consist of max AP vs. F_{av} curves, parameterized by microburst radius (R_p) and aircraft type (2, 3, or 4-engine).

Effect of Microburst Model Radius. Simulation results for the 2-engine aircraft parameterized by microburst radius are given in Figure 6.15. The 500-meter microburst radius produces higher max AP for a given F_{av}, while the results for all other radii lie essentially on the same curve. The 500-meter radius curves, therefore, will be used to set the alert thresholds. Note that the relationship between F_{av} and AP is nearly linear. This is consistent with the results in Section 6.2, which indicated a high linear correlation coefficient between F_{av} and trajectory degradation (using much more complex windfields).

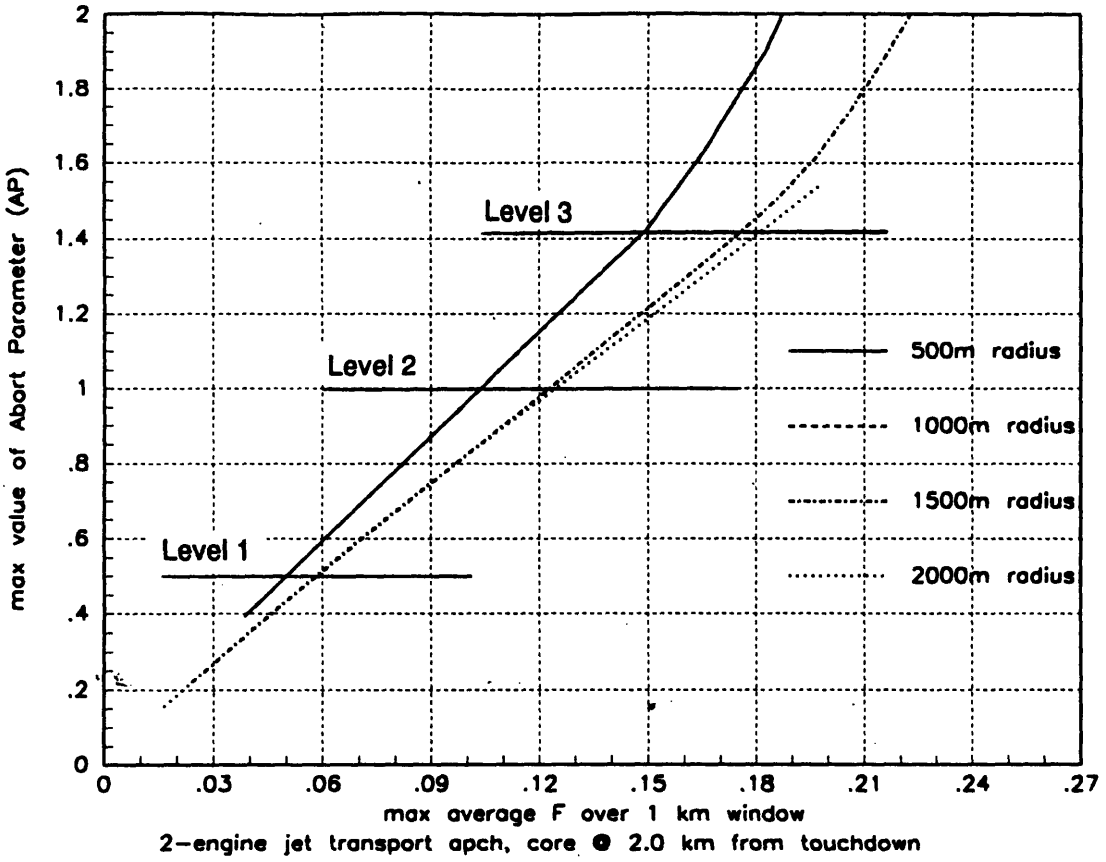

Figure 6.15. Abort Parameter vs. F-factor averaged over 1 km, 2-engine jet transport on approach. The OBV microburst was centered 2.0 km from the touchdown point. The heavy horizontal lines indicate AP threshold values for the three-level alert structure.

Effect of Aircraft Size. Simulation results for the 500-meter microburst radius, parameterized by aircraft size, are shown in Figure 6.16. The maximum AP value for a given $F_{av} < 0.15$ decreases with increasing aircraft size. This effect is due to the higher approach speeds used by the larger aircraft. However, when the hazard value becomes high enough that maximum thrust must be employed, the AP value increases rapidly for the larger aircraft with smaller thrust-to-weight ratios. This effect is apparent from the breakpoints on the plot at $F_{av} = 0.135$ for the three-engine aircraft (point A) and $F_{av} = 0.12$ for the four-engine aircraft (point B).

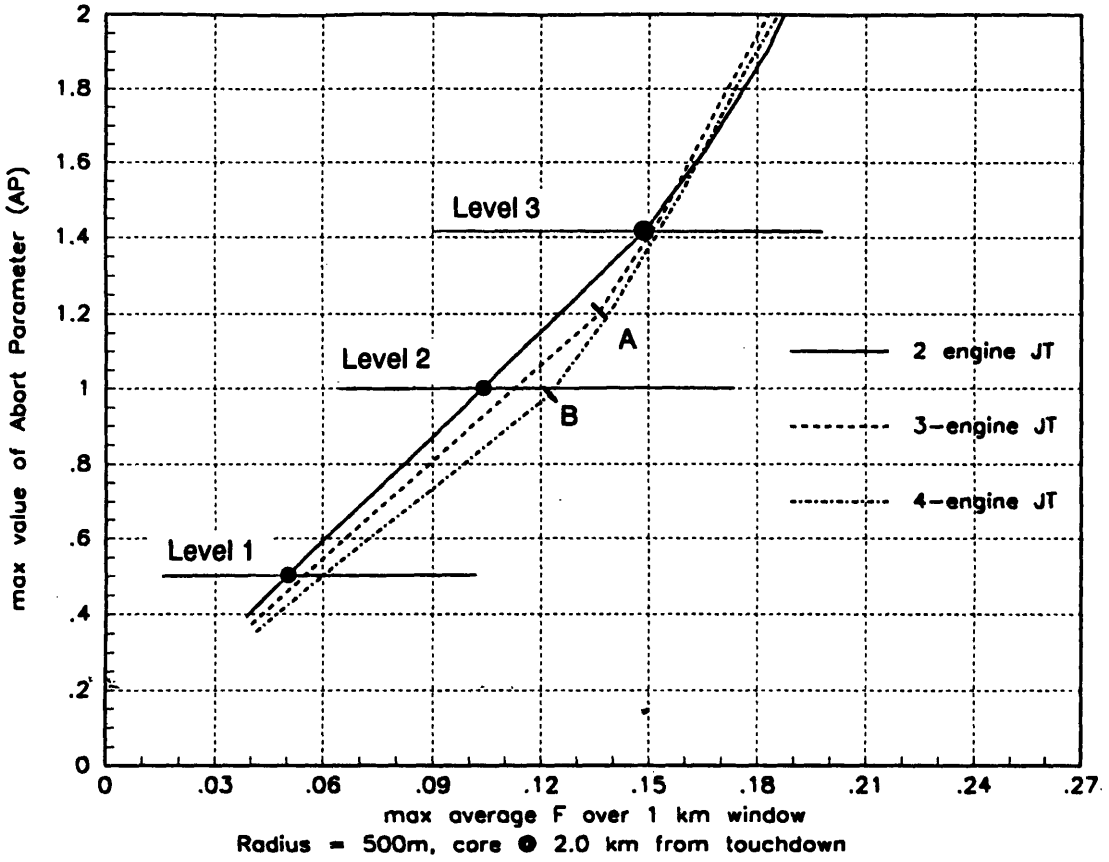

Figure 6.16. Abort Parameter vs. F-factor averaged over 1 km, for 2, 3, 4-engine jet transports. The OBV microburst was centered 2.0 km from the touchdown point, with a radius of 500m. The heavy horizontal lines indicate AP threshold values for the three-level alert structure, and the heavy dots indicate the intersection points used to select F_{av} threshold values.

6.3.9 Selection of Alert Thresholds

Since the 500-meter radius (1-kilometer diameter) microburst produced the highest AP values, the curves in Figure 6.16 were used to determine F_{av} hazard threshold values for the three-level alert structure (Table 6.6). This was done for each of the three aircraft models, and the lowest value for each level was selected as the overall threshold value (right hand column). The threshold was defined by the two-engine transport in all cases, although the results for all three aircraft types are very close at the level 3 threshold. This table represents an alert structure which is both based on a measureable hazard criterion and tied directly to aircraft performance. Note that these values are quite close to those selected for the graphical alert display study (Section 5.4).

Table 6.6. Three-level alert thresholds for jet transports on approach.

Alert Level	AP value to trigger level	F_{av} values to reach AP threshold 2-engine	3-engine	4-engine	Final F_{av} value for hazard threshold
1	0.50	0.050	0.055	0.060	**0.050**
2	1.00	0.104	0.113	0.124	**0.104**
3	1.41	0.148	0.151	0.152	**0.148**

6.3.10 Applicability Issues

The applicability of these results is constrained by the assumptions which were used. One critical assumption was the definition of a nominal controller. The maximum value of AP in a given microburst encounter is partially dependent on controller characteristics. Recall that in Section 6.2, simulations using the high-bandwidth approach controller resulted in less trajectory degradation than simulations with the low-bandwidth controller for all 12 runs (see Figure 6.8). The approach controller used here is intended to be representative of a "typical" automatic glideslope coupler for a transport aircraft. Actual autopilot characteristics vary among different aircraft models and manufacturers. In addition, many approaches are hand-flown by the pilot, and human pilots vary in skill and response time.

Another important assumption was the choice of wind model. The OBV model has been correlated with field studies and adjusted to produce generally representative horizontal and vertical wind profiles. It is difficult to determine exactly how representative it is for simulation purposes. However, since the windfield strength was calibrated by *distance-averaged* F-factor, the details of the wind model will not strongly affect the results. Ideally, a large number of field-measured microburst windfields with varying F_{av} could be used to validate the results. Also, as with the correlation analysis in Section 6.2, there was no attempt made at either simulating or evaluating the contributions of turbulence and vortices to the aircraft hazard.

The assumptions made in the aircraft dynamic model are less critical. The threshold values of AP for the alert levels was reached in the simulations generally without the aircraft reaching stick shaker or maximum thrust. Therefore, the assumptions made on maximum available thrust-to-weight ratio had essentially no impact on the analysis. Also, since the windfields were smooth, the approximation used for the pitching dynamics did not significantly affect the analysis.

Finally, the results in Table 6.8 are for jet transports on approach to landing. With minor modifications to the simulation procedure, a similar set of thresholds could be computed for takeoff cases or for other classes of aircraft (such as general aviation).

6.3.11 Conclusion

A technique has been presented for determining microburst alert hazard thresholds based on aircraft performance. In this method, alert levels are defined for specific levels of aircraft trajectory degradation. Simulations are performed to determine the relationship between measured values of a suitable hazard criterion and the aircraft trajectory degradation. The resulting relationship is then used to select threshold values of the measureable hazard criterion which correspond to the desired levels of aircraft trajectory degradation.

The technique was applied to the particular case of jet transports on final approach. A three-level alert structure was established, based on a trajectory degradation criterion which indicated whether or not the approach should be aborted. Simulations were run using a simple parametric microburst model to determine the values of a hazard criterion (averaged F-factor) required to trigger the three alerting levels. Table 6.8 lists these values. Finally, the applicability of the results was discussed.

7. Multi-Sensor Measurement of Microburst Characteristics

7.1 Overview

The alert generation techniques described in the previous chapter are based on values of a suitable microburst hazard criterion, which are computed from measured or estimated microburst characteristics. The measurement of microburst characteristics is a complex task. As discussed in Chapters 2 and 3, microburst data can come from a large pool of sources. These include sensors of many different types located on several different platforms, as shown in Figure 7.1. Accurate estimation of microburst characteristics depends not only on the available data sources, but on the method used to assimilate the available data.

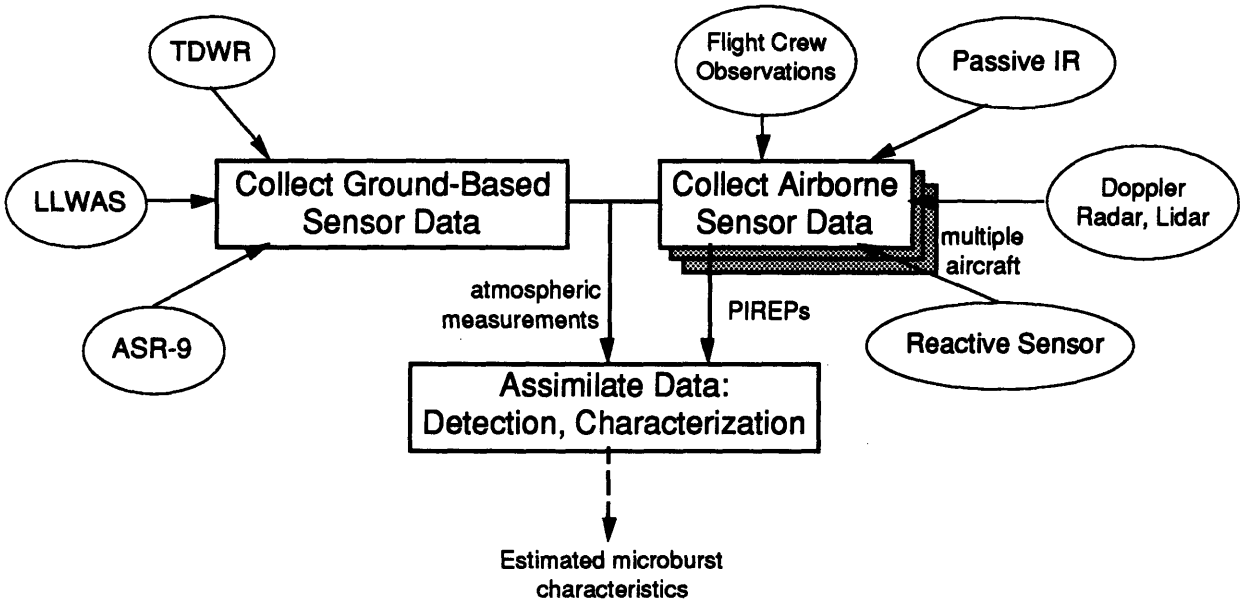

Figure 7.1. The Measurement and Assimilation Task

In this chapter, a computational technique for assimilating multi-sensor, multi-platform atmospheric measurements to produce estimates of microburst characteristics will be presented.

7.2 The Multi-Sensor Data Assimilation Problem

Many microburst detection systems have geometrical observability problems. For example, Doppler sensors can only measure wind velocities radial to the sensor, not vertical winds. However, the microburst aviation hazard is partially due to vertical winds. The F-factor based hazard criteria analyzed in the previous chapter require both horizontal shear and downdraft information. Limits on sensor resolution and range also complicate estimation of microburst characteristics.

However, as more and more of the sensor systems illustrated above become operational, it will become increasingly likely that more than one sensor system will be available in a given situation. Combining data from different systems with different measurement characteristics can compensate for individual sensor deficiencies and produce more accurate estimates. Another possible benefit of using multiple sensors is that conflicting data from different sensor systems could be resolved, and faulty sensors could be identified.

This "data fusion" process can be done on a number of levels. One approach is to merge the final products of the sensor systems to produce improved alerts. For example, product-level techniques have been used to integrate TDWR and LLWAS information [Cornman and Mahoney, 1991] and to determine the probability of hazardous wind shear given a wide range of evidence [Stratton and Stengel, 1992]. Another approach is to integrate sensors on the data level. The data-level approach is more complex, due to the large volumes of data produced by several of the wind shear sensor systems. However, if successfully implemented, observability problems due to poor sensor geometry can be alleviated. Data from multiple sources can be combined to form a "super sensor" with improved sensing geometry. The technique presented here is a model-based data-level approach which attempts to gain this observability benefit without prohibitively large computational or data transmission requirements.

7.3 Model-Based Approach

Basic Concept. In the model-based approach, the actual microburst windfield is approximated by an analytical model. The model-based data assimilation process involves selection of the model parameters which best make the model winds approximate the actual winds. Once the best parameters have been estimated, microburst characteristics for alert generation can be easily derived from the analytical windfield model.

Why Use a Model-Based Approach? The model-based approach has several desirable characteristics. If the model represents the true windfield well enough, then a large number of atmospheric measurements can be encapsulated in a small set of "best-fit" model parameters. This is useful if data is to be transmitted between sensors or sensor platforms. Another important advantage is that the model-based approach allows estimation of quantities which cannot be directly measured. For example, vertical velocities can be inferred from model parameters which were computed based only on Doppler-measured radial velocities. This is possible because analytical models can take advantage of basic fluid dynamic relationships such as mass continuity, and can incorporate knowledge and data from past microburst observational studies.

Analytical Microburst Model Description. The analytical microburst model used in this work was initially developed by Oseguera and Bowles [1988] and later improved by Vicroy [1991]. The Oseguera-Bowles-Vicroy (OBV) model uses shaping functions to generate an axisymmetric flowfield which satisfies the mass continuity equation and is representative of the major characteristics of measured microbursts. The same model was used in the hazard threshold study (Section 6.3). Sample winds for a constant-altitude path through the model windfield are shown in Figure 7.2. The horizontal winds exhibit the classic microburst characteristic of a headwind increase followed by rapid shearing to

a tailwind. The vertical wind plot shows a downdraft in the microburst center and smaller updrafts at the edges.

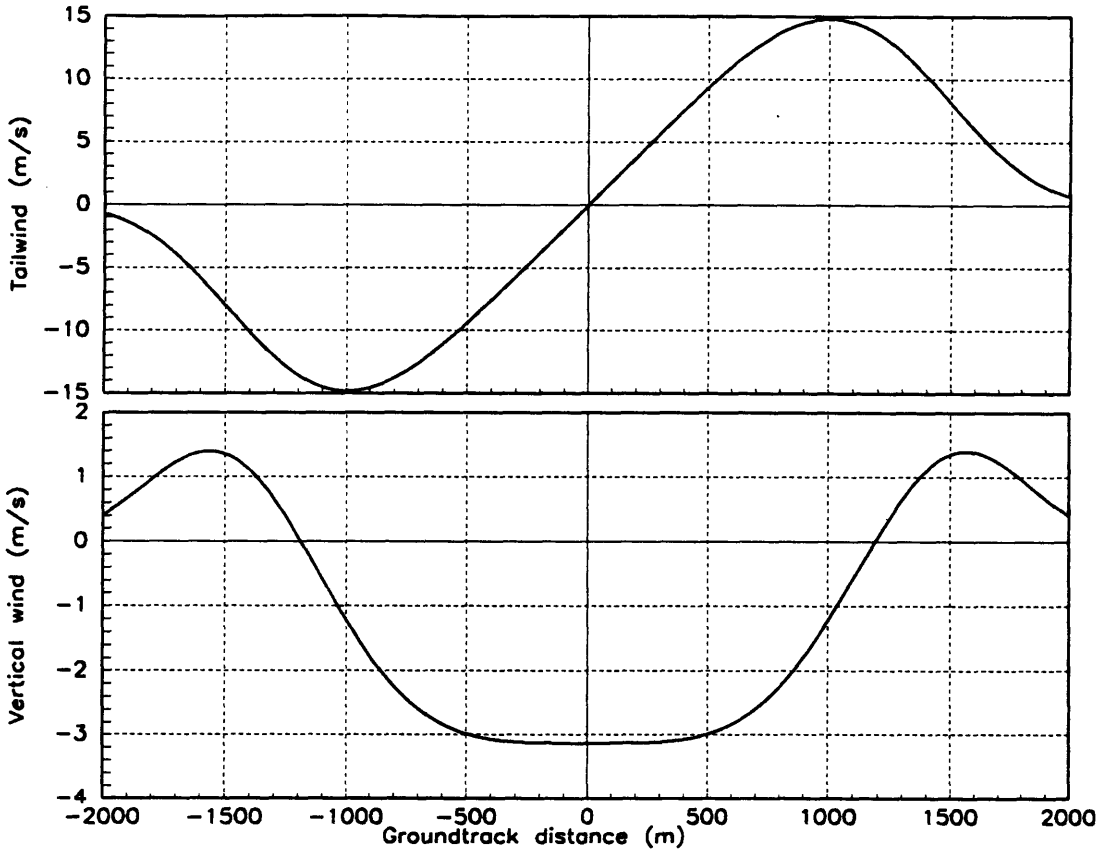

Figure 7.2. OBV Microburst Model Windfield. Sample winds for a constant-altitude (80 m AGL) flight path through the microburst center. Model parameters for this plot: $U_m = 15$ m/s, $R_p = 1000$ m, $Z_m = 80$ m, $x_0 = y_0 = U_0 = U_h = V_0 = V_h = 0$.

The microburst winds are uniquely defined by a set of five parameters and three empirically-adjusted constants. For this study, a simple ambient wind (4 additional parameters) was added to the microburst windfield. The model parameters are summarized in Table 1. The total winds are given by non-linear, smooth, differentiable functions of the parameters and a given (x,y,h) position as follows:

$$W_{xE} = W_{xE,\,mb}\,(x - x_0,\, y - y_0,\, h,\, U_m,\, R_p,\, Z_m) + U_0 + U_h h \tag{7.1}$$

$$W_{yE} = W_{yE,\,mb}\,(x - x_0,\, y - y_0,\, h,\, U_m,\, R_p,\, Z_m) + V_0 + V_h h \tag{7.2}$$

$$W_h = W_{h,\,mb}\,(x - x_0,\ y - y_0,\ h,\ U_m,\ R_p,\ Z_m) \qquad (7.3)$$

W_{xE}, W_{yE}, and W_h are the earth-referenced eastward, northward, and vertical wind velocities respectively, and h is the altitude above ground level (AGL). Quantities with "mb" subscripts are functions of position and the first five parameters in Table 7.1. These functions are summarized in Appendix C.

Table 7.1. Modified Oseguera-Bowles-Vicroy Microburst Model Parameters. The type column indicates a microburst (MB) or ambient wind (AW) parameter.

Parameter	Type	Description
x_0	MB	X-coordinate (East) of microburst center (m)
y_0	MB	Y-coordinate (North) of microburst center (m)
U_m	MB	Maximum horizontal outflow speed (m/s)
R_p	MB	Radius of maximum outflow (meters)
Z_m	MB	Altitude AGL of maximum outflow (meters)
U_0	AW	Eastward ambient wind constant component (m/s)
U_h	AW	Eastward ambient wind altitude gradient (m/s/m)
V_0	AW	Northward ambient wind const. component (m/s)
V_h	AW	Northward ambient wind altitude gradient (m/s/m)

The OBV model is axisymmetric, but naturally occurring microbursts are often asymmetric [Hallowell, 1990]. In addition, multiple microbursts have been observed to occur close together and interact. To handle these cases, the model was extended to allow multiple interacting microbursts. For each microburst, another set of five microburst model parameters (the first five in Table 1) can be added. It is assumed that the ambient wind will be roughly constant throughout the x-y space of interest, i.e. near the airport, and so only one set of ambient wind parameters is required. The winds from each model microburst are superimposed to get the overall model windfield. Mass continuity is still preserved. In the simulation study described below, when a "two-microburst" model is discussed it does not indicate that there are two microbursts being detected. It indicates that two superimposed model microbursts are being used to simulate a complex microburst windfield with more than one area of high downdraft speed.

7.4 Estimation Performance Metrics

The results in Chapters 4, 5, and 6 indicated that the important alerting quantities are position, extent, and intensity as quantified by a microburst hazard criterion. The "effectiveness" of the proposed algorithm is defined by its capability to produce these quantities. Therefore, two figures of merit were defined.

The first concerns position and extent. Given a center point, an "extent polygon" can be drawn for a microburst windfield [Hallowell, 1990]. An example is shown in Figure 7.3. The vertices of the polygon correspond to the points of maximum radial outflow speed, measured radially outward from the center point. This polygon encloses the entire performance-decreasing portion of the microburst. The ability of the model-based algorithm to define this hazardous region can then be evaluated by comparing the extent polygon A of the truth windfield to the extent polygon B of the analytical model windfield corresponding to the estimated parameters:

$$M_{extent} = \frac{A \cap B}{A \cup B} \tag{7.4}$$

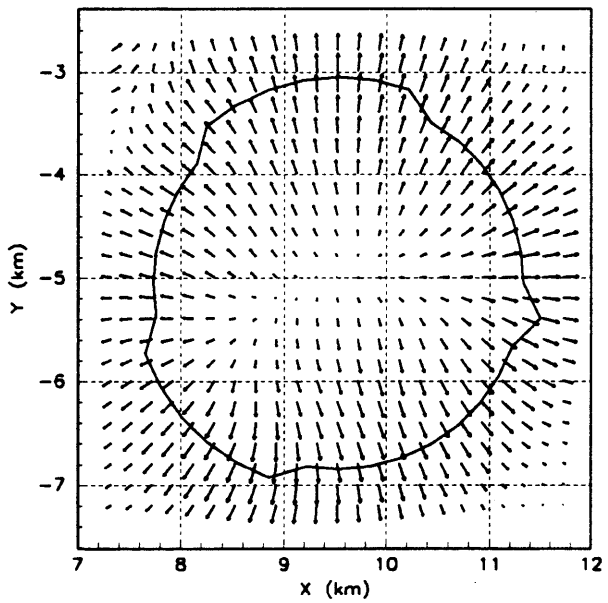

Figure 7.3. Microburst extent polygon. Horizontal wind vectors with the outflow extent polygon superimposed.

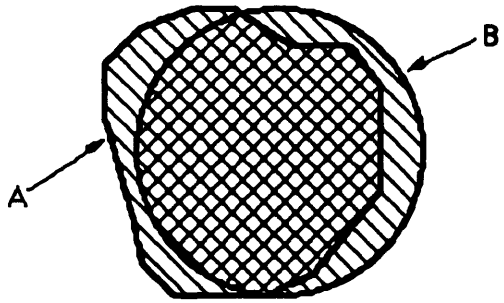

Figure 7.4. Extent Figure-of-Merit. Pictorial representation of Eqn. 7.4. The cross-hatched area is $A \cap B$ and the sum of the cross-hatched and striped areas is $A \cup B$. Note that the model "polygon" B is a circle for the single-microburst axisymmetric OBV model.

This quantity has a maximum value of 1 (for an exact match) and falls off for both underestimation and overestimation of the extent boundaries (Figure 7.4). Core position errors are also reflected, since the model extent polygon is then laterally translated with respect to the true extent polygon. This quantity is a function of altitude, but the dependence was found to be very weak and only results for a single altitude are presented in this report.

Microburst intensity was defined by the F-factor criterion:

$$F \equiv \frac{\dot{W}_x}{g} - \frac{W_h}{V} \tag{7.5}$$

W_x in equation 7.5 indicates tailwind-positive horizontal windspeed along the aircraft track direction, and is not to be confused with W_{xE}, the eastbound horizontal windspeed. The study documented in Section 6.2 concluded that F averaged over 3000 feet (approx. 1 km) of the aircraft flight path yields a good hazard estimate for several different situations. This criterion was adopted in a modified form for this study. Microburst hazard values were calculated as follows: (1) compute 1 km average F-factors for a large number of parallel constant-altitude paths through the microburst, (2) average the resulting values 500 m laterally across flight paths, and (3) pick the largest averaged F-factor as the hazard value.

This value still depends on the direction and altitude of the parallel flight paths along which F is evaluated, because (1) microbursts can be asymmetrical in shear strength, and (2) microburst winds vary with altitude. In the simulation results presented below, averaged F-factors will be presented for either eastbound or northbound flight paths. Results will also be presented for several altitudes.

7.5 Model Acceptability Evaluation

Before development of a real-time algorithm, the feasibility of matching microburst winds with this analytical model was examined using a deterministic least-squares technique. Note that the least-squares technique would not be a practical *real-time* technique. Requirements for a real-time algorithm and a possible real-time algorithm based on Kalman filtering will be presented in Section 7.6.

7.5.1 Least-Squares Wind Matching Technique

The technique was an improved version of that used by Schultz [1990] to develop a vortex ring model of the Dallas-Fort Worth airport microburst [Fujita, 1986]. The algorithm computes the values of the model parameters, **x**, which minimize the total mean squared error between a set of "truth" winds and the analytical model winds:

$$\text{Cost} = \frac{1}{N} \sum_{j=1}^{N} e_j^2(\mathbf{x}) \; ; \quad \mathbf{e}(\mathbf{x}) = \mathbf{W}_{\text{model}}(\mathbf{x}) - \mathbf{W}_{\text{truth}} \tag{7.6}$$

where N is the total number of wind data points and **W** is a column vector of all east (W_{xE}), north (W_{yE}), and vertical (W_h) wind components at all (x, y, h) locations. **e** is the vector of errors between the truth winds and the analytical model winds for the current model parameters, **x**. The minimization algorithm was based on a non-linear Gauss-Newton method with linear constraints. The technique is described in detail in Appendix D.

7.5.2 Simulated Truth Windfield

The windfield data used for algorithm testing was generated by the Terminal Area Simulation System (TASS) developed by Proctor [1987]. It is a highly detailed computational simulation of a complex multiple microburst event which occurred at Denver-Stapelton airport on July 11, 1988. This event caused one near accident and a total of five aircraft to make missed approaches (see Section 2.5.2). Windfield data from five times during this event was available, with a horizontal spacing of 200m and a vertical spacing of approximately 80m. For the following analyses the largest microburst in the event was selected (Figure 7.5). The horizontal windfield has a classic microburst outflow pattern. However, the vertical wind contours show a complex structure as indicated by two separate regions of high downdraft, neither of which correspond to the apparent horizontal windfield center (marked with an ×). This rather complex event was chosen to test the estimation algorithm in a challenging but realistic situation.

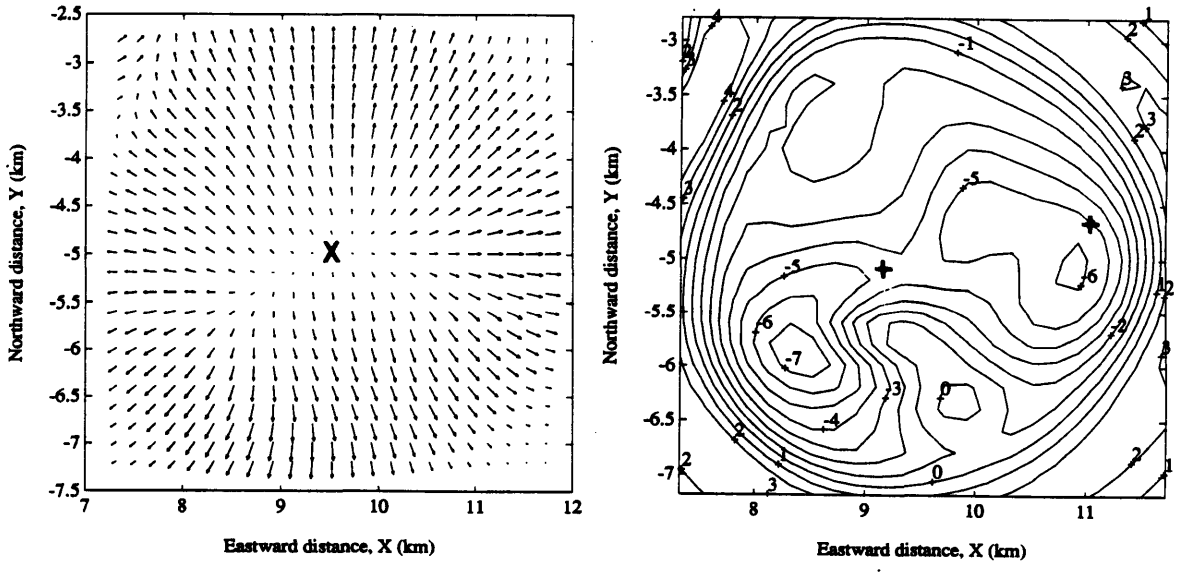

Figure 7.5. TASS-simulated windfield for 11 July 1988 microburst event at DEN. At left is a vector plot of horizontal winds: maximum velocity shown is 18.7 m/s. At right: vertical windspeed contours. Data is shown for an altitude of 177m AGL.

7.5.3 Least-Squares Matching Results

The deterministic least-squares procedure was done with a single-microburst model (9 parameters) and with a two-microburst model (14 parameters). The resulting parameters for the single-microburst case are given in Table 7.2. Note that the approximate radius of this microburst is 1700 meters, and the maximum outflow speed is approximately 18 m/s. The ambient wind magnitude is small in this case.

Table 7.2. Single-microburst least-squares parameter fit results.

Parameter	Value	Parameter	Value
x_0 (m)	9528	U_0 (m/s)	0.9
y_0 (m)	-5047	U_h (m/s/m)	-0.001
U_m (m/s)	17.8	V_0 (m/s)	0.5
R_p (m)	1717	V_h (m/s/m)	-0.002
Z_m (m)	68.2		

Results for the two-microburst model are given in Table 7.3. The first microburst (MB #1) has similar parameters to the one-microburst fit result. The second microburst is positioned 2 km east of the first, and is smaller and weaker (outflow speed of 7 m/s). The resulting windfield has two areas of high downdraft speed, similar to the TASS windfield. The model microburst core positions have been marked by + symbols on the vertical wind contour plot in Figure 7.5.

Table 7.3. Two-microburst least-squares parameter fit results.

Parameter	MB #1	MB #2	Parameter	Value
x_0 (m)	9328	11161	U_0 (m/s)	1.3
y_0 (m)	-5115	-4615	U_h (m/s/m)	-0.001
U_m (m/s)	17.5	6.71	V_0 (m/s)	0.4
R_p (m)	1665	1268	V_h (m/s/m)	-0.002
Z_m (m)	68.3	70.4		

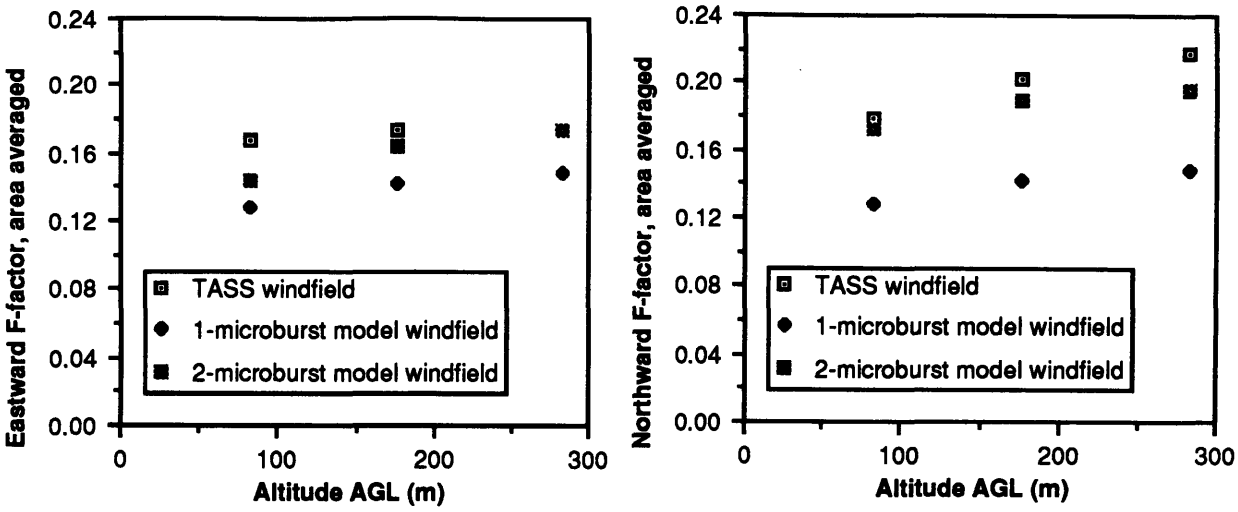

Figure 7.6. Microburst intensity matching performance for least-squares fit.

The single-microburst fit produced an extent figure of merit of 0.92. The two-microburst fit result was slightly lower, at 0.85. As seen in Figure 7.5, this microburst was fairly axisymmetric in extent, so these good results are not surprising. However, plots of area-averaged F-factor looking Eastward and Northward for three altitudes (Figure 7.6) reveal that the microburst is not symmetric in intensity. As indicated by the "TASS windfield" points in Figure 7.6, the F-factors are larger when looking northward through the microburst than when looking eastward. This is due to the vertical wind distribution (Figure 7.5, righthand plot) which has multiple regions of high vertical windspeeds. For this reason, the single-microburst fit produces a single broad region of somewhat weak vertical winds in an attempt to globally match the windfield, producing intensity underestimates in both directions. The two-microburst fit, however, succeeds in matching the vertical windfield well and duplicates the intensity of the TASS windfield well in both directions.

For alerting purposes, both model windfields adequately represent the actual extent. However, the single-microburst model underestimates the intensity somewhat. Since the alert generation procedure (Section 6.3) classifies microbursts into relatively

few intensity levels, very accurate intensity is probably not required. Based on these results, and similar results obtained using a TASS windfield from another microburst event, the model was judged to be acceptable for estimation purposes.

7.6 Real-Time Iterated Extended Kalman Filter Algorithm

7.6.1 Real-Time Algorithm Requirements

The real-time estimation algorithm must satisfy several constraints to be practical. It must be *recursive*, to handle new measurements as they become available. It must also *account for time variation* in the model parameters since microbursts are short-lived, dynamic phenomena and sensor measurements will be taken at different times. In addition, the algorithm should take advantage of microburst statistical characteristics from past field studies. This implies a *probabilistic* approach. A Kalman filtering technique was developed to satisfy these requirements.

7.6.2 Algorithm Description

Estimation Problem Structure. Kalman filtering techniques require a state-space dynamic model of the system and a relationship between system parameters and measured quantities. In this case, analytical model parameters which best describe the microburst are to be estimated from measurements of the winds. The analytical microburst model parameters were therefore used as the filter state variables $\mathbf{x}(t)$. It was assumed that the time evolution of the microburst parameters can be adequately modeled by a linear, time-invariant, continuous-time system:

$$\dot{\mathbf{x}}(t) = \mathbf{A}\,\mathbf{x}(t) + \mathbf{B}\,\mathbf{u}(t) + \mathbf{L}\,\mathbf{w}(t) \tag{7.7}$$

Deterministic inputs to the system are represented by $\mathbf{u}(t)$, and $\mathbf{w}(t)$ is a white Gaussian process noise input. The **A**, **B**, and **L** matrices define the dynamic model; they will be discussed below. Since the state variables $\mathbf{x}(t)$ are the analytical model

parameters, they are related to the wind measurements through the analytical model wind equations. The resulting non-linear discrete-time measurement equation, at measurement time t_k, is:

$$\mathbf{z}_k = \mathbf{h}_k(\mathbf{x}(t_k)) + \mathbf{v}_k \tag{7.8}$$

where the measurement equations $\mathbf{h}$ are the wind equations from the analytical model, and $\mathbf{v}_k$ represents measurement noise. The state vector, $\mathbf{x}$, and error covariance matrix, $\mathbf{P}$, for a single downdraft case are defined as follows:

$$\mathbf{x} = [x_0 \; y_0 \; U_m \; R_p \; Z_m \; U_0 \; U_h \; V_0 \; V_h]^T \tag{7.9}$$

$$\mathbf{P} = E\left[(\mathbf{x} - \hat{\mathbf{x}})(\mathbf{x} - \hat{\mathbf{x}})^T\right] \tag{7.10}$$

where $\hat{\mathbf{x}}$ is the current parameter estimate. The microburst eastward core location, x_0, should not be confused with $\mathbf{x}$, the state vector. Process noise, $\mathbf{w}(t)$, and measurement noise, $\mathbf{v}_k$, are white and gaussian with the following characteristics:

$$E\left[(\mathbf{L}\,\mathbf{w}(t))(\mathbf{L}\,\mathbf{w}(\tau))^T\right] = \mathbf{L}\,\mathbf{Q}(t)\,\mathbf{L}^T\,\delta(t - \tau) \tag{7.11}$$

$$E\left[\mathbf{v}_k\,\mathbf{v}_k^T\right] = \mathbf{R}_k \tag{7.12}$$

The aim of the filter is to produce the state estimate $\hat{\mathbf{x}}$ which minimizes the error covariance $\mathbf{P}$. Since the measurement equation is non-linear, this cannot be accomplished with a standard Kalman filter algorithm. An extended Kalman filter (EKF) approach was chosen. The structure and principal equations for the EKF are briefly described below, based on the formulation given by Gelb [1974]. The filtering algorithm for discrete-time measurements is a two step process: (1) apply the system dynamic model to propagate the state estimate and state estimation error covariance between measurements, and (2) update the estimate when new measurements arrive.

Estimate Propagation: Microburst Dynamic Modeling. For linear, time-invariant, continuous-time system dynamics the propagation of the state estimate and estimation error covariance between measurements is governed by:

$$\dot{\hat{\mathbf{x}}}(t) = \mathbf{A}\,\hat{\mathbf{x}}(t) + \mathbf{B}\,\mathbf{u}(t) \tag{7.13}$$

$$\dot{\mathbf{P}}(t) = \mathbf{A}\,\mathbf{P}(t) + \mathbf{P}(t)\,\mathbf{A}^T + \mathbf{L}\,\mathbf{Q}(t)\,\mathbf{L}^T \tag{7.14}$$

The **A**, **B**, **L**, and **Q** matrices define the microburst time-evolution dynamics. Since the analytical model is time-invariant, these parameters must come from another source. Unfortunately, there is no simple time-varying analytical model currently available. However, measured microburst statistics can be used to approximate some dynamics. For example, microburst radial extent tends to increase steadily throughout the microburst lifecycle. Analysis of data from Colorado microburst measurements [Wilson, et. al., 1984; Hjelmfelt, 1988] indicates that the change in radial extent vs. time can be approximated by a constant bias (a) with additive white zero-mean gaussian noise (n):

$$\dot{R}_p = a + n(t) \tag{7.15}$$

where a = 0.102 km/min and the noise term has a standard deviation of 0.15 km/min. The constant bias is treated as a deterministic input, and the noise term leads to an value for one element in the **Q** matrix. Similar modeling may be possible for some of the other state variables. For example, motion of the microburst core ($\dot{x}_o$,$\dot{y}_o$) may be related to the ambient wind parameters, which would produce non-zero entries in the **A** matrix. No conclusive data on microburst motion has yet been published. In the simulations discussed below, the **A** matrix was assumed to contain all zeros. The **B** and **Q** matrix elements were set based on statistical information where possible, and from engineering judgement when no statistical information was available.

Since the time behavior of the microburst parameters is not well modeled, significant process noise is required. The use of process noise to compensate for modeling deficiencies is similar to the well-known technique of applying a "forgetting factor" to older data in a batch least-squares formulation. In any case, these simple dynamics lead to sparse **A**, **B**, **L**, and **Q** matrices, and the propagation step in the filter requires little computation.

Incorporating Measurements. When new measurements are taken, the estimate is updated. The non-linear measurement equation, however, complicates the update process. The formulation presented here is based on the extended Kalman filter update with the addition of a local iteration procedure to reduce the effects of the measurement non-linearities [Jazwinski, 1970; Gelb, 1974]. At the k^{th} measurement time t_k, a local iteration (over i) is performed. The i^{th} parameter estimate at time t_k, $\hat{\mathbf{x}}_{k,i}$, is updated with the following expression:

$$\hat{\mathbf{x}}^+_{k,i+1} = \hat{\mathbf{x}}^-_k + \mathbf{K}_{k,i}\left[\mathbf{z}_k - \mathbf{h}_k(\hat{\mathbf{x}}^+_{k,i}) - \mathbf{H}_k(\hat{\mathbf{x}}^+_{k,i})(\hat{\mathbf{x}}^-_k - \hat{\mathbf{x}}^+_{k,i})\right] \tag{7.16}$$

$$\hat{\mathbf{x}}_{k,0} \equiv \hat{\mathbf{x}}^-_k, \quad i = 0,1,... \tag{7.17}$$

The Kalman gain **K** is ordinarily computed from:

$$\mathbf{K}_{k,i} = \mathbf{P}^-_k \mathbf{H}^T_k(\hat{\mathbf{x}}^+_{k,i})\left[\mathbf{H}_k(\hat{\mathbf{x}}^+_{k,i})\mathbf{P}^-_k \mathbf{H}_k(\hat{\mathbf{x}}^+_{k,i}) + \mathbf{R}_k\right]^{-1} \tag{7.18}$$

and $\mathbf{H}_k$ is the locally linearized measurement matrix:

$$\mathbf{H}_k(\hat{\mathbf{x}}) = \left[\frac{\partial \mathbf{h}_k(\mathbf{x})}{\partial \mathbf{x}}\right]_{\mathbf{x}=\hat{\mathbf{x}}} \tag{7.19}$$

Computation of $\mathbf{H}_{k,i}$ requires evaluation of the partial derivatives of the analytical model wind equations with respect to the current parameter estimate vector $\hat{\mathbf{x}}_{k,i}$ for each of the measurements $\mathbf{z}_k$. In the above expressions, $\hat{\mathbf{x}}^-_k$ and $\mathbf{P}^-_k$ indicate the propagated estimate and error covariance at time t_k (prior to updating), while $\hat{\mathbf{x}}^+_k$ and $\mathbf{P}^+_k$ indicate the

updated estimate and covariance based on the measurement $\mathbf{z}_k$. The local iteration is repeated until the scaled norm of the parameter estimate does not change significantly. After the new estimate has been produced, the updated error covariance matrix is computed using values from the final iteration step:

$$\mathbf{P}_k^+ = \left[\mathbf{I} - \mathbf{K}_{k,i}\, \mathbf{H}_k\left(\hat{\mathbf{x}}_{k,i}^+\right)\right] \mathbf{P}_k^- \tag{7.20}$$

Testing indicated that the iterated filter results in significantly better estimates than the standard EKF. This is consistent with findings by other investigators [Wishner, et. al., 1969]. A probabilistic interpretation of this iteration based on Bayesian maximum likelihood estimation is given by Jazwinski [1970]. Jazwinski demonstrates that the iteration process is actually a Newton-Raphson iteration for the conditional *mode* of the (non-Gaussian) posterior state probability density. This is then used as the conditional mean would be in a standard linear Kalman filter. Since the conditional mode is used rather than the conditional mean, the resulting estimate is biased. The bias in the estimate becomes small as the error covariance becomes small.

One difficulty with the above updating algorithm is that there may be large numbers of measurements available at a single time step (as with TDWR data, for example), and the computation of the Kalman gain requires inversion of an r-by-r matrix, where r is the number of measurements. The number of computations required to do this scales as r^3. In a linear filter, a large batch of measurements can be treated as a series of sequential scalar measurements (occurring at infinitesmal time spacing) without loss of information, thereby avoiding this problem. When the measurement equation is non-linear, the measurements cannot be incorporated sequentially without losing a significant amount of information. Therefore, an alternate form of the gain computation is required. When the number of measurements is large, and the measurement noises are independent (diagonal $\mathbf{R}_k$) it is more efficient to use the "information form" of the gain computation:

$$\left(\mathbf{P}_k^{-1}\right)^+ = \left(\mathbf{P}_k^{-1}\right)^- + \mathbf{H}_k^T \mathbf{R}_k^{-1} \mathbf{H}_k \tag{18}$$

$$\mathbf{K}_k = \left(\mathbf{P}_k^{-1}\right)^+ \mathbf{H}_k^T \mathbf{R}_k^{-1} \tag{19}$$

This form can be readily applied to the iterated EKF update described above. Although the covariance update must now be done inside the loop, the required matrix inversion is only n-by-n, where n is the number of states (model parameters). The number of floating-point operations required now scales linearly with r and cubically with n. Section 7.6.5 presents an analysis of the filter computational requirements.

Multiple-Microburst Form. As discussed above, several model microbursts can be superimposed to simulate a more complex windfield. In this case, 5 new states are added for each additional model microburst. For i microbursts, the full state vector, **x**, is defined as:

$$\mathbf{x} = \left[\mathbf{x}_{mb,1}^T \;\; \mathbf{x}_{mb,2}^T \cdots \mathbf{x}_{mb,i}^T \; U_0 \; U_h \; V_0 \; V_h\right]^T \tag{20}$$

where:

$$\mathbf{x}_{mb,i} = \left[x_{0,i} \;\; y_{0,i} \;\; U_{m,i} \;\; R_{p,i} \;\; Z_{m,i}\right]^T \tag{21}$$

In the simulations discussed below, one- and two-microburst forms are used.

Initialization. This algorithm can incorporate multi-sensor data, given that the microburst has previously been detected. The assumption is made that a single sensor has detected the event and produced an initial parameter estimate with the associated error covariance. The initialization algorithm therefore depends on the measurement characteristics of the initial sensor. The general process, however, is the same for all sensors. Quantities that can be directly measured are estimated from the initial data set, and quantities which are unobservable are initialized using statistics derived from microburst field studies.

For example, if a TDWR initially detects a microburst, estimates of maximum outflow speed (U_m), outflow radius (R_p), and core position (x_0,y_0) can be derived from the measured radial flowfield. The outflow depth Z_m is an unobservable parameter, and must be initialized from statistics. Outflow depth statistics have been tabulated by Biron and Isaminger [1991] for 26 Colorado microbursts, and the mean altitude of maximum outflow velocity was found to be 109 meters. This value was used to initialize the filter for the simulations discussed below, in which TDWR was always assumed to make the initial detection. The initial covariance matrix was diagonal, and values were chosen based on sensor resolution criteria or statistics where possible.

7.6.3 IEKF Update Simulation

The first step in algorithm evaluation was to determine if the iterated EKF update procedure was capable of incorporating sensor data (as modeled by small subsets of the complete windfield) and producing reasonable extent and intensity estimates. The TASS simulated winds were considered to be the "truth" winds, and simulated sensor data subsets were taken from them. Assuming that the windfield was frozen in time (or alternatively, no time has lapsed between measurement sets), different combinations of sensor data were used sequentially to update the current estimate. Three sensors were considered in this way: (1) TDWR data, (2) winds measured from the aircraft by differencing inertial and air data measurements (referred to henceforth as INS data), and (3) airborne Doppler radar (ABDR) data.

For TDWR and ABDR data, it was assumed that the sensor was far enough from the microburst that radial wind measurements could be considered parallel to each other, and that the antenna tilt angle was horizontal so that all data was taken at the same altitude. For example, for an eastward-looking radar, the W_{xE} components of the TASS windfield at a single altitude comprised the working data set (Figure 7.7). TDWR measurements were taken at an altitude of 82 m AGL (the lowest TASS data altitude) for

both eastward- and northward-looking cases, and ABDR measurements were taken from 177 m and 283 m AGL TASS data. In all cases, gaussian zero-mean white noise with a standard deviation of 1 m/s was added to the "truth" data to simulate measurement noise based on TDWR accuracy specifications [Campbell, 1992]. All radar data sets were taken at 400 m range and azimuth resolution. Note that the approximation of parallel measurements was made for numerical simplicity here. The algorithm can be used with radial measurements of arbitrary elevation and azimuth angles also (see Appendix C.2).

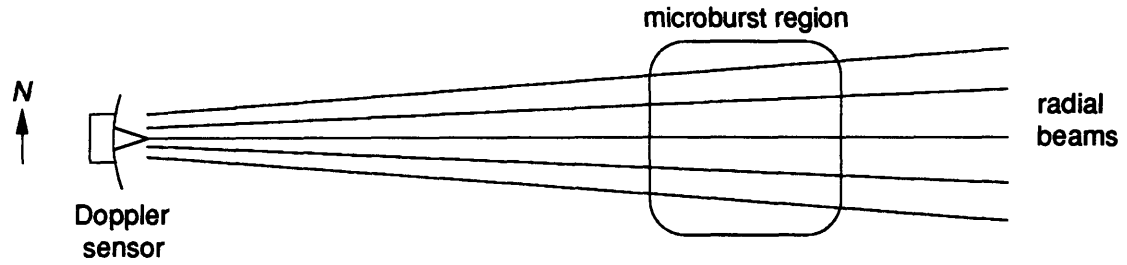

Figure 7.7. Measurement geometry for simulated Doppler measurements. Eastward-looking sensor shown. Radial measurements are approximately parallel and constant-altitude inside the microburst region.

Aircraft winds (INS data sets) consisted of 3-component winds (W_{xE}, W_{yE}, W_h) along a straight, constant-altitude flight path. Four 200m resolution INS data sets were defined, including eastward and northward flight paths at 177 m and 283 m AGL. All paths passed through the center of the windfield, as marked by the × on the left-hand plot in Figure 7.5. The measurement noise standard deviation used for aircraft wind measurements was 1.4 m/s.

For simulation purposes, it was assumed that TDWR made the initial microburst detection. Therefore, the first step was to initialize the filter as previously described, and then apply the iterated EKF update to incorporate the TDWR measurement. The resultant parameter estimate and error covariance was saved. Then the estimate was updated by incorporating either an INS data set or an ABDR data set, starting with the saved parameter estimate and covariance matrix. Twelve total sensor fusion cases were tested with both one-microburst and two-microburst versions of the filter.

Single-Microburst Filter. For all cases tested, the iteration procedure used in the update converged in 3 to 5 iterations. Results for four representative cases are presented here:

(1) Initialization only: Eastward-looking TDWR measurements alone (denoted TDWR-E)

(2) The results of (1) were updated using a sequence of eastbound aircraft-measured winds taken at an altitude of 177 m AGL (denoted INS-E)

(3) The results of (1) were updated using a sequence of northbound aircraft-measured winds taken at an altitude of 177 m AGL (denoted INS-N)

(4) The results of (1) were updated using northward-looking airborne Doppler radar data at 177 m AGL (denoted ABDR-N)

The extent results are good (Table 7.4), and illustrate the effect of fusing data from sensors with different measurement geometries. The extent figure-of-merit for TDWR-East is 0.85, and does not improve when an eastward path of INS data is incorporated. However, when northbound INS data or northward-looking airborne radar data is incorporated, the extent figure-of-merit increases to the .91 to .92 range. Since the microburst is not exactly symmetric in extent (it is slightly larger in the north-south direction), incorporation of northward-looking data increases the radius parameter in the OBV model to cover more area. This is equal to the performance achieved by the least-squares fit computation.

Table 7.4. Extent figures-of-merit: 1-microburst time-invariant data fusion.

TDWR-E alone	TDWR-E + INS-E	TDWR-E + INS-N	TDWR-E + ABDR-N
0.853	0.853	0.911	0.917

The effect of multi-directional data is also visible in the intensity results (Figure 7.8). As with the least-squares results, it is clear that the single-microburst model cannot match intensity with the complex windfield of this microburst. The TDWR-alone result is low, and incorporating an eastbound path of INS data actually lowers the estimate; this is because the path does not cross both regions of high vertical windspeed. Incorporating

a northbound path of INS data or the ABDR data improves the estimate significantly at the higher altitudes (at which the INS and ABDR measurements are taken). The low-altitude intensity estimates remain low, probably due to two factors: (1) no further low-altitude data has been incorporated, and (2) the one-microburst model does not have enough degrees of freedom to fit the intensity well at all altitudes.

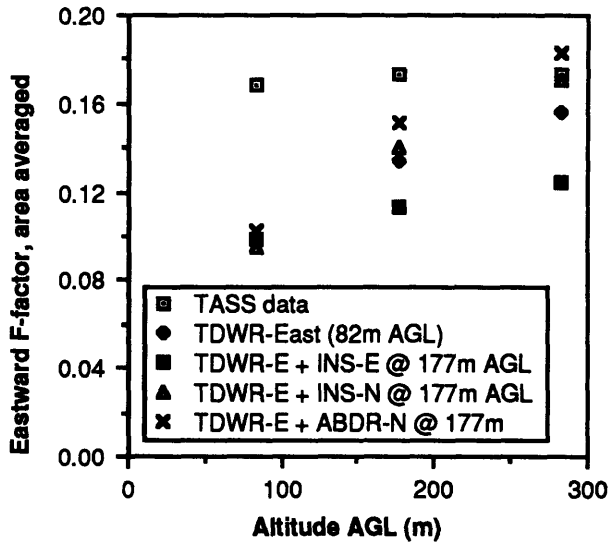

Figure 7.8. Intensity estimation - 1-microburst time-invariant data fusion

Two-Microburst Filter. The two-microburst version of the filter involved significantly more computation, since in general more iterations were required than for the single-microburst filter. Also, some cases did not converge consistently and required adjustment of the initial parameters. However, when the two-microburst filter did converge, the results were good. Extent figures-of-merit were between 0.85 and 0.90 for all cases. Figure 7.9 shows eastward intensity values for the algorithm applied to three cases:

(1) northward-looking TDWR data alone (TDWR-N)

(2) TDWR-N updated with eastward aircraft-measured winds taken at 177 m AGL (INS-E)

(3) TDWR-N fused northward-looking airborne radar data at 283 m AGL (ABDR-N).

Although the TDWR is looking north and the intensity values shown are for eastbound paths, the results for TDWR data alone are fairly good. There is some overestimation at high altitudes. Inclusion of ABDR data with the same look angle as the TDWR (northward) improves the results slightly. As expected, inclusion of the eastbound INS data provides a second measurement direction and produces the best intensity estimates.

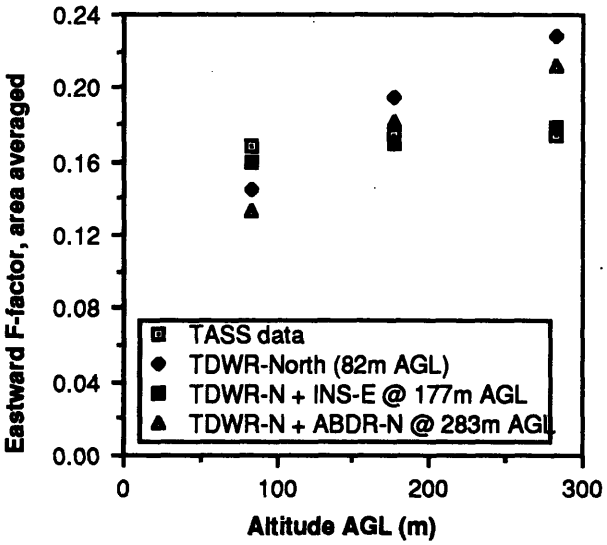

Figure 7.9. Intensity estimation - 2-microburst time-invariant data fusion

7.6.4 Full Iterated EKF Simulation

The third part of the algorithm evaluation was to include the microburst dynamic model (the propagation part of the filter) and apply the technique to time-varying data. For this analysis, data was taken from three different times in the evolution of the 7/11/88 microburst event. The three data sets were spaced two minutes apart, where the middle data set corresponds to the time-invariant data set used in the previous section and represents the time at which the microburst was strongest.

The time spacing for this data was larger than desired, since TDWR data is updated at one minute intervals and airborne radar data would be available even more

frequently. However, it was still possible to construct illustrative examples. The following three sample cases assume that initial detection is made with northward-looking TDWR. Two minutes later, three different events are postulated:

Case 1. A sequence of eastbound aircraft-measured winds is downlinked to the ground and incorporated along with a second set of TDWR data.

Case 2. An aircraft traveling northbound receives the previous TDWR estimate and updates using an airborne Doppler radar.

Case 3. An aircraft traveling eastbound receives the previous TDWR estimate and updates using an airborne Doppler radar.

At the third time step (+4 minutes), the parameter set is passed to the ground and an updated with another set of TDWR data. The data sets were derived in the same way as for the time-invariant cases, and the estimate and error covariance were propagated between measurements as described above. These cases were run for both one and two-microburst versions of the filter.

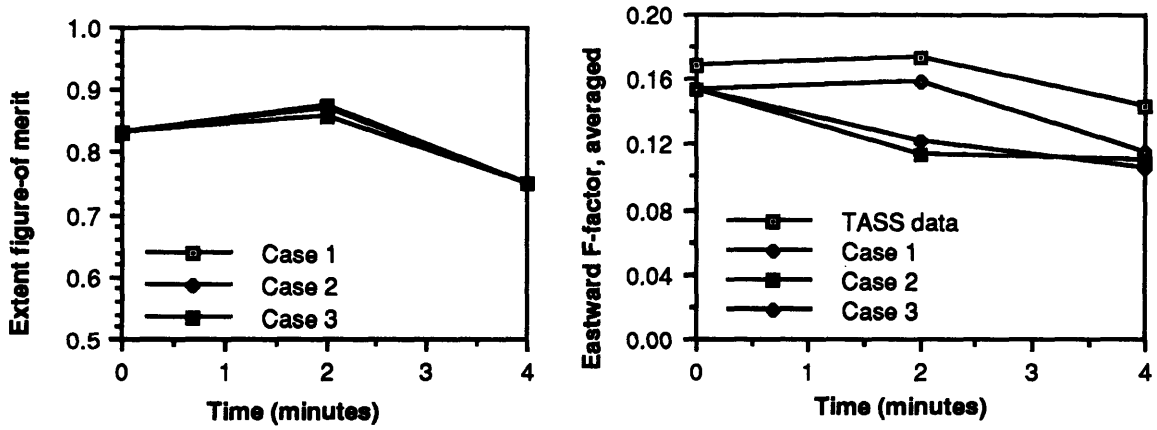

Figure 7.10. Extent figures-of-merit and eastbound intensity estimates for one-microburst filter

One-microburst filter. The extent figures-of-merit (Figure 7.10, left) are fairly good (> 0.82) through the first two times, but are slightly lower (0.76) in the third time step. This is due to the distorting effect of an adjacent, weaker microburst on the shape of the primary microburst. The axisymmetric model used in the filter cannot represent this situation very accurately. There is little difference between the three sample cases.

The intensity results (Figure 7.10, right) are similar to those from the single-microburst time-invariant runs, in that all of the estimates are low. As evident from the "TASS data" curve, the actual microburst increases in strength in the first two minute span and then decreases in the last two minutes. Only in case 3, in which northbound TDWR measurements were combined with eastbound ABDR measurements, was the filter able to follow this trend. The low estimates are most likely due to difficulties matching this complex microburst with the single-microburst filter. However, the intensity results were somewhat sensitive to the choice of process noise strength, which indicates a need for further study of microburst time dynamics.

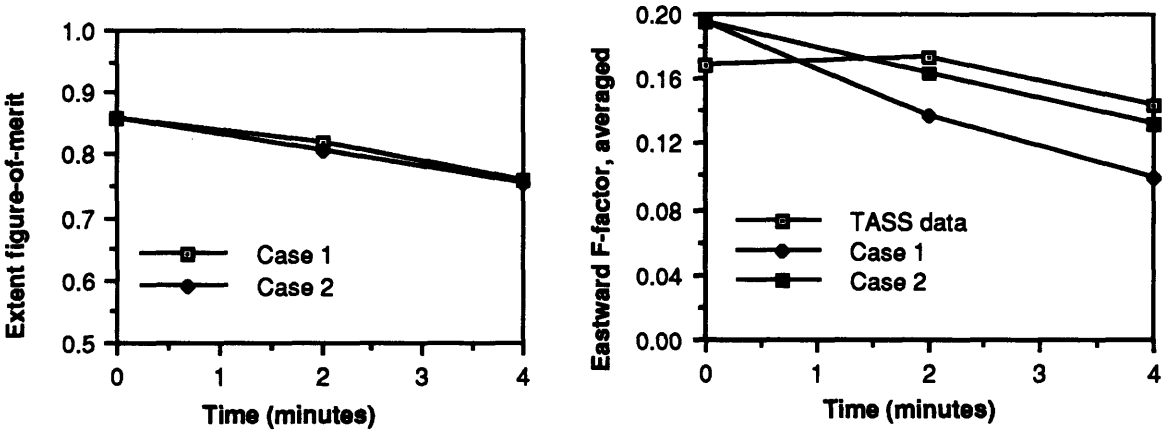

Figure 7.11. Extent figures-of-merit and eastbound intensity estimates for two-microburst filter

Two-microburst filter. The two-microburst algorithm produced mixed results (Figure 7.11). In the first time step (which was the same for all cases) the estimate was good in both intensity and extent. At the second time step, the case 1 intensity estimate was low as in the one-microburst case. The case 2 estimate, however, was significantly better than for the one-microburst case, and this continued at the third time step. For both cases, the extent estimates were roughly the same as for the one-microburst runs.

The case 3 data produced the best estimates for the one-microburst filter. When processed with the two-microburst filter, the update iterations at the second time-step did

not converge. Instead, the estimate cycled between two possible solutions. This is indicative of numerical robustness problems in the two-microburst filter, and will be further discussed later.

7.6.5 Computational Requirements

The computational requirements for the IEKF algorithm were tabulated in terms of floating point operation count. Figures 7.12 and 7.13 demonstrate the advantage gained by using the information form of the filter update rather than the standard form. The floating point operation count is for one filter step (propagation and update) with 5 iterations. For the one-microburst filter (9 states), it requires less computation to use the information form when the number of measurements (r) is 8 or greater. For the two-microburst filter (14 states) the information form is better when $r \geq 11$. For all of the simulation cases, the number of measurements was sufficiently large that the information form was used.

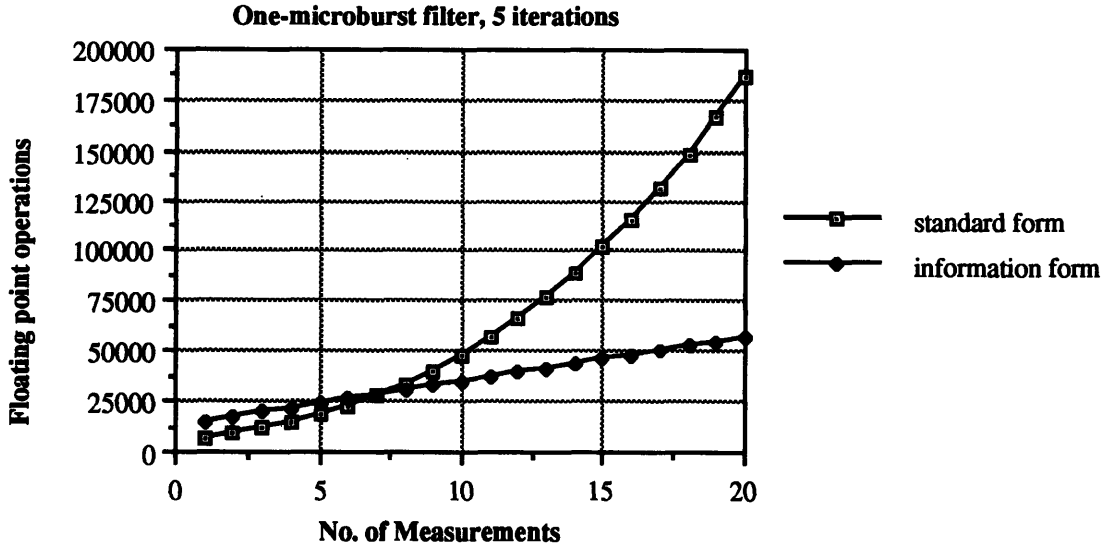

Figure 7.12. Computational burden for the standard and information forms of the IEKF update, applied to the one-microburst (9-state) filter.

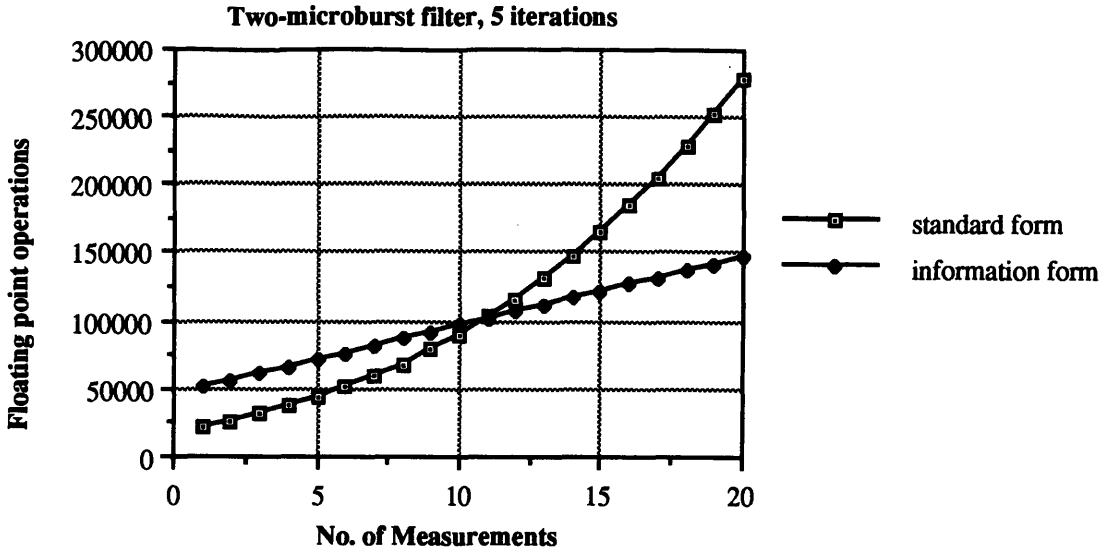

Figure 7.13. Computational burden for the standard and information forms of the IEKF update, applied to the two-microburst (14-state) filter.

The total computational burden scales approximately linearly with the number of measurements when the information form is used. In either form, the burden also increases linearly with the number of iterations. Figures 7.14 and 7.15 are plots of the floating point operations (FLOPS) count for large numbers of measurements. For 100 measurements, the counts range from 142,000 FLOPS for a one-microburst, three iteration filter up to 764,000 for a two-microburst, seven-iteration filter.

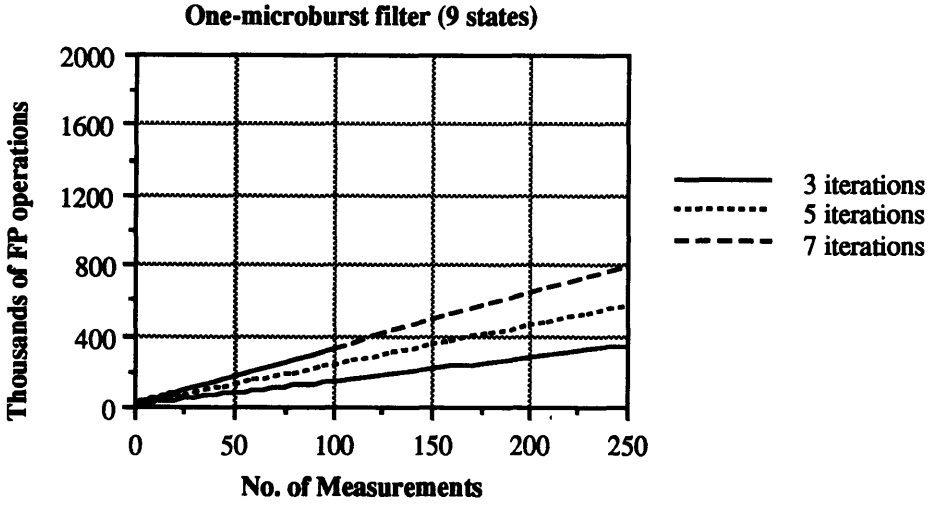

Figure 7.14. Computational burden for large numbers of measurements - one-microburst filter. Floating point operation counts for 3, 5, and 7 iteration update procedures are shown. The information form of the update is used.

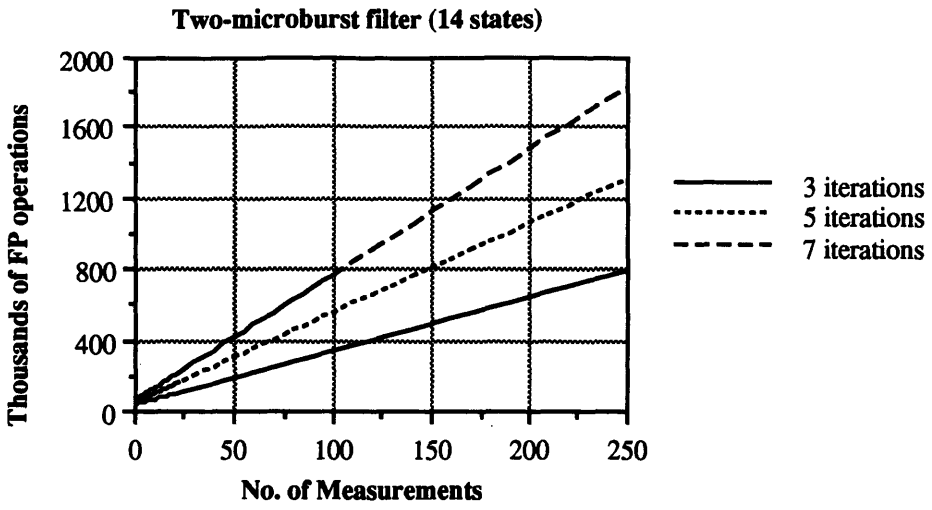

Figure 7.15. Computational burden for large numbers of measurements - two-microburst filter. Floating point operation counts for 3, 5, and 7 iteration update procedures are shown. The information form of the update is used.

7.6.6 Computation of Alerting Parameters

The model-based algorithm is well suited for producing the graphical iconic multi-level displays that were found effective in the part-task simulator experiments (Chapter 5). The extent polygons used here to evaluate estimation efficiency would be used directly as icon shapes. For the one-microburst filter, this is especially straightforward as the extent "polygon" is actually a circle centered on (x_0, y_0) with radius R_p.

For intensity, the averaged F factor is an effective hazard criterion (Section 6.2). Although F-factors for several altitude and directions were tabulated to look at estimation accuracy, it would be necessary to assign a *single* hazard value to a given microburst. A practical approach would be to select the largest hazard value, over all directions and altitudes, below a specified maximum altitude.

7.6.7 Discussion of Algorithm Characteristics

The simulations demonstrate the potential usefulness of the IEKF technique, particularly for estimating the size and position of the microburst hazard region. Several other characteristics of the algorithm were also observed during the simulation runs, although it should be noted that the use of computational data for a single historical microburst event limits the scope of the conclusions that can be drawn.

The single-microburst algorithm appeared to be numerically robust. Errors in initial conditions and reasonable variations in choice of filter parameters did not produce filter instability in either the time-invariant or the time-varying simulations. The two-microburst form, however, was numerically sensitive. In several cases the filter diverged during the update iteration, and choice of parameters such as the initial covariance matrix appeared to have a large impact on the convergence properties of the filter. In cases where convergence was reached the results tended to be dependent on the actual windfield shape. When the windfield had two clear downdraft centers, the convergence was steady and the results for both intensity and extent were good. In cases where there was only one region of high downdraft (such as the first time-step of TASS model data) then the two sets of microburst parameters either became coincident, or one microburst became very weak. In addition, the covariance matrix elements corresponding to the unnecessary microburst parameters grew very large.

Possible solutions to this problem include more intelligent initialization based on recognized windfield features, or running multiple filters of different types in parallel. In any case, the improved intensity estimation possible with the two-microburst filter must be weighed against the associated numerical difficulties. It should also be noted that the wind data used to evaluate the algorithm was more widely spaced in time than for any planned or operational sensor system, which had an adverse effect on estimation accuracy.

Aside from numerical robustness, there are other implementation issues to be considered. The computational requirements of the filter were assessed, and can be quite large when large numbers of measurements are incorporated. Computational load can be decreased by thinning large data sets, at the expense of estimation accuracy. Also, datalink bandwidth needs to be considered. A model parameter list of 9 elements, for example, has an associated 81 element covariance matrix (of which only 45 are unique). It is likely that the entire covariance matrix is not necessary to initialize the next update step, and that some elements could be omitted without appreciable loss of performance.

Although the algorithm has been presented in the context of multi-sensor data assimilation, it does not require multiple sensors. Benefits would still be gained if it were used with a single sensor due to the additional information incorporated in the analytical model (correct fluid dynamics, empirical microburst data). A possible single sensor application would be estimation of vertical winds from Doppler sensor data.

7.6.8 Adapting the Algorithm to Other Measurement Problems

Although the IEKF algorithm was implemented for measurement of microburst characteristics, it can be readily generalized to other atmospheric phenomena. The fundamental estimation procedure is unchanged. The system model equations (7.7), (7.8), and (7.9) must be rewritten for the new problem. The following elements are required:

- A parametric analytical model of the phenomenon of interest, which satisfies essential physical relationships (such as fluid dynamic mass continuity). The model must include once-differentiable equations relating the available measurements to the model parameters:

  -> used to determine $\mathbf{x}$, $\mathbf{u}$, $\mathbf{A}$, $\mathbf{B}$, $\mathbf{h}_k$, $\mathbf{H}_k$

- Statistical data on characteristics of the phenomenon which can be used to establish process noise parameters and initial conditions:

  -> used to determine $\mathbf{L}$, $\mathbf{Q}$, $\mathbf{u}$, $\mathbf{x}(t_0)$, $\mathbf{P}(t_0)$

- Statistical characteristics of the measurement process:

  -> used to determine $\mathbf{R}_k$

From this point forward, the equations in Section 7.6.2 can be applied in the same fashion as for microburst estimation. The choice of filter computation form (i.e. standard gain computation vs. information form) would have to be reevaluated for the specific application.

7.7 Conclusions

A recursive model-based data assimilation technique for multi-sensor microburst hazard assessment was presented. A simple analytical microburst model is used to approximate the actual windfield, and a "best" set of model parameters are estimated from measured winds using an extended Kalman filtering technique. The resulting parameter estimate and associated error covariance encapsulate the current state of knowledge about the actual windfield, and can be used to compute estimates of microburst position, extent, and intensity for alert generation. The technique takes advantage of fluid dynamic relationships and statistical data from past microburst field studies to aid the estimation process.

Simulated measurements for three types of sensors were derived from a time-varying computational model of a historical microburst event. Two forms of the data assimilation algorithm were then tested, one using a single-microburst model and one using superposition of two model microbursts to represent the windfield. It was found through both time-invariant and time-varying simulations that both forms of the algorithm were able to estimate the position and extent of the simulated microburst well. The single-microburst model tended to underestimate microburst intensities. The two-microburst model produced better intensity estimates, but suffered from numerical robustness problems. Computational requirements for the algorithm were also assessed as functions of filter complexity and number of wind measurements.

8. System-Level Implementation Issues

8.1 Overview

In this work, the microburst alerting process was examined as three major subtasks: Measurement, Alert Generation, and Alert Application (Figure 8.1). A user-centered approach was taken to identify and study critical system design issues for each of these subtasks.

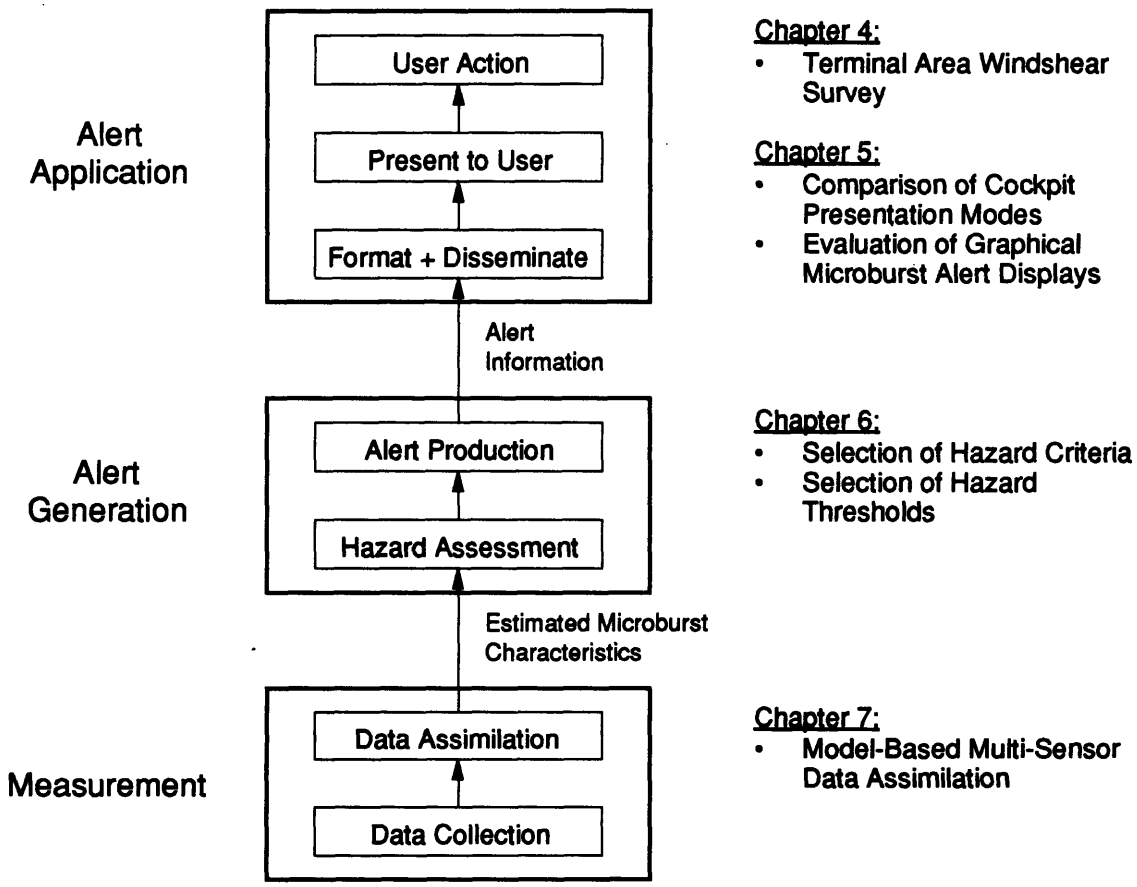

Figure 8.1. Microburst alerting task and research breakdown. The studies related to each subtask are listed at right.

Section 8.2 reviews the user-centered research approach, and examines the relationship between user-centered design and overall system performance. The implications of the research in this report for existing and future systems is then examined on a system-by-system basis in Sections 8.3, 8.4, and 8.5.

8.2 User-Centered Application of the Research

8.2.1 Requirements Flow-down between Design Studies

The end users for microburst alerts are flight crews and ATC personnel; in this work, flight crew alerting was emphasized. In keeping with a user-centered, top-down approach, the alert application task was addressed first. The results of the alert generation work produced functional requirements and objectives for the alert generation studies, and the multi-sensor data assimilation study was driven by results from both the alert application and the alert generation studies. In this way, the decision-making needs of the flight crew, at the logical end of the alerting process, ultimately affected the requirements for *all* of the microburst alerting subtasks.

The result of this research approach, therefore, is to provide useful design data for the alerting subtasks with the overall goal of optimizing crew decision-making efficiency. This result is directly related to microburst alerting system operational performance, and will be discussed below.

8.2.2 Relationship of User-Centered Design to Operational Efficiency

A critical design tradeoff for microburst alerting systems is the conflict between airport operational efficiency and safety. At one extreme, a microburst alerting system can be designed to maximize safety by halting all airport operations whenever microbursts are detected in the airport vicinity. For a busy airport with high incidence of microburst activity, this would have an unacceptably large impact on operational efficiency. For example, during the 1989 TDWR Operational Evaluation at Denver's Stapleton Airport, wind shear events were detected within 5 nm of the airport during 19 of the 32 days of TDWR operation [Weber, et. al., 1991]. Clearly, the potential safety improvements provided by a microburst alerting system must be balanced against operational needs and constraints.

This can be stated as a system goal; the system should be designed to achieve the best airport operational efficiency possible while maintaining a high level of safety. Operational efficiency is improved for a given level of safety by improving alerting efficiency, which can be defined as the capability of the alerting system to usefully convey the required alert information to end users. When end users, either ATC or flight crews, are alerted inefficiently, then decision-making performance is poor. This limits the achievable airport operational efficiency for a given level of safety, since a large degree of conservatism must be built into alert response procedures, and unnecessary missed approaches or delayed takeoffs will occur. Good alerting efficiency, therefore, is directly related to achievable operational efficiency. Good alerting efficiency is also a direct consequence of the user-centered design approach, which is based on enhancing user decision-making performance.

8.2.3 Applying the Research

Application of the research results to real alerting systems should therefore be done with the intent of improving the usefulness and timeliness of the information given to users, in order to improve alerting efficiency and hence operational efficiency. For existing systems, where the system architecture is fixed, modifications must be made on the subtask level with an eye toward improving user decision-making performance and thus alerting efficiency. For new microburst alerting systems, however, the user-centered design approach can be applied from the start. In this case, the desired alerting system operational efficiency can be specified in terms of requirements for alerting accuracy, presentation, and timeliness. Subsystems can then be designed in top-down fashion, in which the requirements flow down task-by-task from alert application to measurement.

In the following three sections, the implications of the research are discussed for an existing system (TDWR/LLWAS), a near-term system (Airborne predictive) and future integrated microburst alerting systems.

8.3 Implications of the Research for the TDWR/LLWAS Alerting System

The development of Terminal Doppler Weather Radar and enhanced LLWAS has greatly improved ground-based microburst detection capabilities. Both of these systems have demonstrated good performance in detecting microbursts. However, field experiences and other studies have indicated a number of system implementation problems including overwarning and inefficient alert dissemination (see Section 2.5.2). Application of the research documented in this report could help alleviate these problems.

8.3.1 Potential TDWR/LLWAS Improvements

Graphical Cockpit Presentation of Microburst Alerts. The ground-based TDWR and LLWAS systems currently rely on verbal flight crew alerting (although ATC is alerted with multi-level graphic displays). The work in this report indicates that there would be several potential benefits to changing to graphical flight crew alerting. The presentation mode simulator experiment (Section 5.3) indicated that graphical alerts are preferred by pilots, and lead to better decision-making and lower workload than verbal or textual alert presentations. The windshear survey and part-task simulator experiments also provided recommendations about graphical alert content and format to aid the alert design process.

Furthermore, graphical alerts could help alleviate the overwarning problem due to laterally offset microbursts (see Figure 2.7). The position of the alert icon would inform the crew when microbursts are actually displaced from the flight path, and therefore eliminate the perception of these situations as false alarms. Finally, graphical alerts which have been disseminated by datalink would be less likely to be missed or misinterpreted, as were the verbal alerts issued during the July 11, 1988 microburst event (see Section 2.5.2).

F-Factor Based Alert Generation. The work in Chapter 6 indicates that changing to an F-factor based alerting strategy would improve alerting efficiency. The hazard criterion for current ground-based systems is "delta-V," the peak measured headwind-to-tailwind change through the microburst. This quantity was shown in Chapter 6 to be a poor predictor of aircraft performance degradation and may therefore be partly responsible for the TDWR perceived overwarning problem. Averaged F-factor was best correlated with aircraft performance, and would be a better choice. However, F is not directly measureable since TDWR and LLWAS do not measure vertical winds. In addition, the airspeed (required for computation of the horizontal component of F-factor) of a given aircraft is not necessarily known by ground-based systems and must be assumed. This could be overcome either by inferring downdraft speed from shear measurements [Vicroy, 1992], advanced data assimilation techniques (such as the one proposed in Chapter 7), or simply by using mean shear as the hazard criterion. Although mean shear was not as effective as averaged F-factor, it showed significantly better performance than "delta-V" and can be directly computed from TDWR radial wind measurements.

Redefinition of the Alert Structure. The TDWR alert structure has two primary levels (see Section 2.5.2), "wind shear with loss" for low-intensity microbursts and "microburst alert" for hazardous microbursts. In addition, the measured "delta-V" is directly reported as a numerical value, rounded to the nearest 5 knots. The two primary levels can be interpreted in terms of recommended procedures. On approach to landing, for example, the primary decision is whether or not to abort the approach. A less drastic response to reported wind shear is to make the approach with increased airspeed. In the TDWR alert structure, "wind shear with loss" is an advisory alert (increase airspeed, stay alert), and a "microburst alert" should force a missed approach.

Recall that a three-level structure was found useful for decision-making purposes in the second part-task simulator experiment (Section 5.4). Although the three different levels did *not* necessarily correspond to different recommended response procedures, the implicit intensity trends available from the changing alert levels were found useful by the subjects. Some subjects wanted *more* than three levels due to this effect. The horizontal wind change ("delta-V") numbers would appear to accomplish this, but are ineffective because "delta-V" correlates poorly with aircraft trajectory degradation (see Section 6.2) and therefore is not very useful for comparing relative strengths of microbursts as aircraft hazards.

The alert structure could therefore be improved by using a better hazard criterion and defining an alert structure, including three (or possibly more) levels, which is related better to aircraft performance and thus provides good intensity trends. Also, the two-level *procedural* structure currently used could be preserved by grouping alert levels into "advisory" levels indicating that caution is required, and "executive" levels which require evasive actions. The technique developed in Section 6.3 for threshold evaluation could be applied to establish this structure, and gain the accuracy benefits of basing alert thresholds directly on aircraft performance.

Model-Based Data Assimilation. If the TDWR hazard criterion was changed to F-factor, vertical wind velocities would need to be estimated. In theory, the model-based data assimilation technique (Chapter 7) could be used accomplish this. The technique could also be used for TDWR/LLWAS data fusion, to take advantage of the improved measurement geometry produced by combining the radial TDWR measurements with the two-dimensional LLWAS wind measurements. However, the TDWR system is currently in the deployment phase, and the amount of work required to develop a robust, proven model-based data assimilation algorithm is clearly prohibitive. The model-based

technique will therefore be discussed later in the context of future integrated microburst alerting systems (Section 8.5).

8.3.2 TDWR/LLWAS Implementation Issues

The possible improvements discussed above are subject to technical and economic constraints. Implementation issues associated with each of these possible improvements are considered below.

Equipment Issues for Graphical Alerting. Implementation of graphical microburst alerting is dependent primarily on the availability of a digital datalink and suitable electronic displays in the cockpit. Digital datalink technology advances are being driven by several factors in addition to microburst alerting (see Section 2.3) and will continue to rapidly develop. New generations of transport aircraft will almost certainly have electronic flight instrumentation. However, many currently flying transport aircraft do not have EFIS and will not be retro-fitted for economic reasons. Alerts for these aircraft must either continue to be verbally delivered or displayed by dedicated datalink hardware. Even on currently operational EFIS-equipped aircraft, significant software modifications would be required to allow display of datalinked alerts on an installed EHSI. While technically feasible, this may be prohibitively expensive for some aircraft types.

Impact of Graphical Alerting on Procedures. In addition, the procedural implications of graphical alerting observed in the part-task simulator experiments (Section 5.4) indicate that current microburst alert procedures would need to be reevaluated in order to use graphical alerting. Currently, TDWR alerts are only issued for microbursts which are less than one-half mile from the approach or takeoff courses. If pilots are given a graphical microburst display, and refuse to pass within several miles of any icon, then this procedure would have to be reevaluated. Microbursts which lie more

than one-half mile from the approach or takeoff courses would begin to cause additional missed approaches and delayed takeoffs, degrading airport operational efficiency. Similarly, it was found that pilots were unwilling to pass through a microburst icon even while climbing out on the missed approach. This may place a difficult burden on ATC to maintain safe separation when microbursts occur, since aircraft will be more likely to initiate lateral avoidance maneuvers.

This problem may be reduced by improved training and experience. At altitudes of more than 2000 feet, especially if the aircraft is climbing in a go-around configuration, microbursts are not a strong threat. Therefore, when a missed approach is initiated several miles prior to microburst penetration, the aircraft can cross the microburst region with little difficulty. Guidelines for when a straight-ahead missed approach is acceptable should be clearly defined and justified to flight crews. Guidelines for when a lateral maneuver is acceptable should also be defined, and rules for initiation of lateral microburst avoidance maneuvers should be part of both ATC and flight crew procedures and training.

F-Factor Based Alerting Issues. The barrier to changing the TDWR/LLWAS system to an F-factor based hazard criterion is primarily economic. TDWR systems are currently in the production phase, and major software changes would be expensive. Improving hazard assessment, however, could produce significant benefits. More accurate hazard assessment would enhance airport operational efficiency, since it would allow a finer line to be drawn between hazardous and non-hazardous microbursts. Poor hazard assessment requires a larger safety margin since insignificant microbursts will be misidentified as hazardous ones, and unnecessarily interfere with flight operations. A cost-benefit analysis of conversion to F-based alerting is required to resolve this issue.

Establishing Alerting Thresholds. If a new alerting structure based on a better hazard criterion were adopted, the alert threshold determination technique developed in

Section 6.3 could be directly applied. Ground-based systems do not have complete knowledge of the aircraft characteristics, so alert thresholds would have to be defined by aircraft *class*. This implies a conservative alerting strategy, since the lowest-performance aircraft of a given class will define the alert thresholds. The design tradeoff is in segmenting aircraft into classes. Choosing fewer aircraft classes implies a simpler, but more conservative alerting process. A reasonable approach would be to define three major classes: (1) jet transports, (2) commuter-class aircraft (multi-engine turboprop) and (3) general aviation aircraft. Note that the hazard threshold computation technique would also work for "delta-V", but the results would be less useful due to the poor correlation of "delta-V" with aircraft performance.

8.4 Implications of the Research for Airborne Predictive Alerting Systems

Airborne microburst alerting systems based on forward-look (predictive) sensors will be feasible in the next few years, as these sensors complete the FAA certification process. Since alerting systems based on these sensors are still under development, implementation of the research presented here would be easier than for ground-based systems.

8.4.1 Research Applications

The benefits of applying the research to airborne predictive alerting systems are mostly identical to the ones cited in Section 8.3.1 for TDWR and LLWAS, since the research was not done in the context of a specific sensor system. Graphical multi-level alerting is also recommended for airborne predictive systems, and the procedural and training issues discussed in Section 8.3.2 also apply. The alert threshold computation procedure can be used to produce an alert structure tied closely to aircraft performance. The model-based data assimilation technique could potentially be used for multi-sensor fusion and to infer vertical windspeeds for Doppler sensors, although, as for TDWR,

near-term implementation is unlikely. Although the research applications are similar, the implementation issues for airborne systems are different than for TDWR and LLWAS.

8.4.2 Airborne Predictive System Implementation Issues

Graphical Alerting Displays. Graphical alerting is a natural choice for airborne systems, since alerts are generated onboard the aircraft and can be routed directly to electronic cockpit instrumentation without resorting to a datalink. Standard airborne weather radar systems, for example, already include a plan view color electronic display for precipitation information. These could be adapted to display Doppler wind shear information, and NASA and several manufacturers are currently exploring graphical display options. The advantages of graphical alert presentation discussed for TDWR/LLWAS systems (Section 8.3.1) are equally applicable to airborne predictive systems, especially the desirability of alerting with multiple intensity levels. Airborne sensors can update faster than TDWR, and therefore should produce better intensity trend information.

F-Factor Based Hazard Assessment. Airborne Doppler forward-look sensors, like TDWR, are unable to measure vertical winds. Current plans, however, are to compute F-factor by inferring the vertical winds from horizontal shear measurements [Bowles, 1990; Vicroy, 1992]. This technique is undergoing field evaluation. Also, airborne systems can obtain the current airspeed and use it for F-factor computation.

Alert Structure. Again, the research in this report indicates that multiple-level alerts are desirable. Establishing alert thresholds for airborne systems based on the procedure presented in Section 6.3 is simpler than for ground systems, since the aircraft type and even the immediate configuration and performance characteristics are known. In addition, the accuracy of the results would be increased since the autopilot characteristics of specific aircraft could be taken into account when simulating. Defining

different threshold values for every aircraft type, however, may be excessively complex, since aircraft dynamic characteristics also change with weight, configuration, and pilot skill.

8.5 Implications of the Research for Advanced Integrated Microburst Alerting Systems

8.5.1 The Need for Integrated Microburst Alerting

The demand for air travel worldwide is increasing, and the number of operational jet transport aircraft flying will increase as well. Air Traffic Management (ATM) systems of the future will handle larger numbers of aircraft, including higher aircraft densities in terminal area airspace. The cost of issuing false microburst alerts will also increase, since more aircraft will be affected. Also, effective alert dissemination, presentation and response procedures will be even more important, since higher aircraft densities will place a limit on the evasive actions which can be taken. In summary, there will be strong motivation for improvements in microburst alerting.

Along with airspace crowding will come technological improvements in sensors, ground-air datalinks, computational capabilities, and cockpit instrumentation. The combination of technological improvements with the need for improved alerting leads to the possibility of developing a truly *integrated* microburst alerting system, in which data is continuously exchanged between airborne and ground-based systems in order to optimize performance. Possible advanced microburst alerting system elements and routes of information flow are illustrated in Figure 8.2.

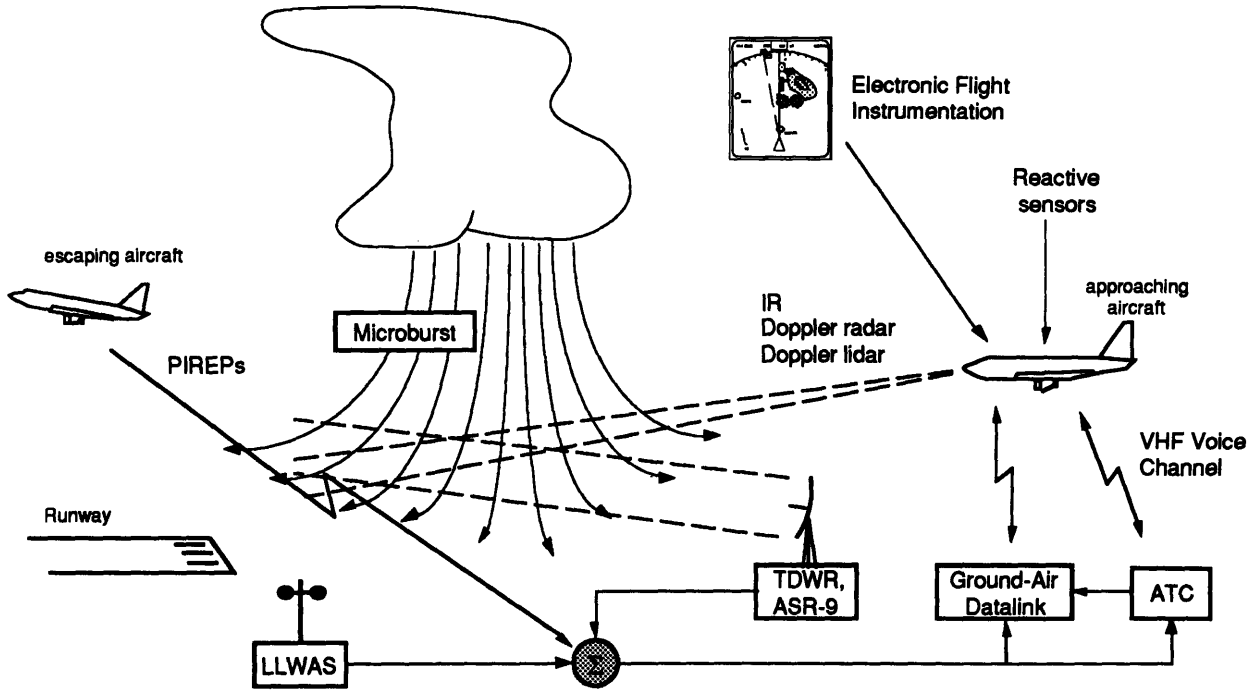

Figure 8.2. Advanced microburst detection and alerting system elements

8.5.2 Applicability of the Research

Since many of the technologies depicted in Figure 8.2 are not yet operational, the configuration of future integrated alerting systems is still flexible. In fact, it is almost certain that different subsets of sensor and datalink technologies will be available at different airports, so the operational configuration of future systems should *remain* flexible to take advantage of available measurement, computational, and dissemination capabilities.

The research presented here is directly applicable to this configuration design problem. Most of the work documented in the previous four chapters was in fact done based on the assumption that the capabilities illustrated in Figure 8.2 would become available. Results from these studies which are applicable to future integrated system design are listed below:

- A graphical, multi-level, iconic alert presentation was found to be an effective decision-making tool for flight crews.
- Implications of graphical alerting for crew response procedures and training were identified.
- The averaged F-factor hazard criterion correlates best with aircraft trajectory degradation, and therefore should be the basis for multi-level alerting.
- A technique for establishing alerting hazard thresholds based on aircraft performance was developed.
- A model-based estimation technique for multi-sensor, multi-platform data assimilation was developed.

For design of an operational microburst alerting system, these results would be applied with consideration of the capabilities and limitations of the sensors, data communication systems, computers, and cockpit instrumentation available.

8.5.3 Integrated Alerting System Features

The exact configuration of future systems will depend heavily on the availability and capabilities of new datalink and sensor technologies. However, it is possible to identify in advance some areas in which there are potentially large gains in alerting efficiency to be made.

Multi-Sensor, Multi-Platform Data Fusion. The hazard assessment accuracy of TDWR, LLWAS, and planned airborne Doppler forward-look systems is fundamentally limited by their inability to observe vertical winds. As demonstrated in Chapter 7, this deficiency can be compensated by combining data from multiple sensors with complementary measurement geometries. This may require frequent exchange of data across between platforms, most likely between aircraft and ground-based sensors.

The model-based data assimilation algorithm presented here would facilitate this process, since it effectively encapsulates large amounts of data in a much shorter list of model parameters. This is a strong advantage for information exchange between platforms. Another advantage of the model-based technique is its ability to fit microburst shapes (extent polygons) to measurements, which allows direct generation of iconic graphical alerts.

The most important consideration for implementation of the data assimilation technique is that the algorithm simulation results in Chapter 7 are not sufficient to establish the performance and numerical robustness characteristics of the algorithm for implementation on real systems. A significant amount of parameter adjustment and simulations using real sensor data would be required. Before such a complex algorithm could be approved for field use, its robustness would have to be conclusively demonstrated.

The relatively high computational requirement of the algorithm is another consideration. This would not be a critical issue for ground-based systems. The TDWR system, for example, already uses several advanced computer workstations for data processing, and the computation power of commercially available equipment continues to rapidly increase. The computational requirements issue is more important for airborne systems, since airborne computational capabilities are limited by volume and electrical power constraints and are currently inferior to ground capabilities. It is reasonable, however, to assume that future generations of aircraft will have significantly more advanced computational hardware and that model-based data assimilation will become a practical possibility.

Automated PIREPs. Pilot comments from the survey and during the part-task simulations indicated that PIREPs are very important. With current equipment and procedures, there are significant delays in the PIREP process. Pilots may not issue a

report until after the completion of evasive action or wind shear recovery procedures, and there is an additional delay incurred as the controller receives and verbally disseminates the PIREP. With the advent of airborne microburst sensors and digital datalinks, it would become possible for airborne systems to automatically broadcast a report when a hazardous microburst is detected. These messages could be relayed to trailing aircraft through a ground station (as in the Mode-S system) or broadcast directly to other aircraft. Such a system would produce more timely PIREPs that could be displayed on the same cockpit instrumentation as other sensor-based microburst alerts.

9. Conclusion

9.1 User-Centered Microburst Alerting System Design

Microbursts have been a major cause of fatal air carrier accidents in the United States. New developments in microburst sensing, ground-air digital data transmission, and electronic cockpit instrumentation provide a plethora of options for design of an effective microburst alerting system. The goal of a microburst alerting system is to prevent microburst-related accidents while having a minimal effect on airport operational efficiency and on flight crew and air traffic controller workload. In this work, a user-centered approach was applied to identify and analyze critical system design issues in a series of multidisciplinary studies.

The primary end users of microburst alerts are flight crews. Therefore, the first task was to determine which information is required by the crew for effective microburst alerting and the most effective presentation techniques for this information. This was done with the Terminal Area Windshear Survey (Chapter 4) and with two piloted part-task simulator experiments (Chapter 5). In Chapter 6, the issue of producing this required alert information - the alert generation task - was addressed, given that microbursts could be detected and their characteristics accurately measured. Next, a data assimilation technique for estimating microburst characteristics from multi-sensor measurements was developed (Chapter 7). Note that in this user-centered, top-down approach, the results of each study formed objectives for following studies. Finally, application of the results of these studies to current and future microburst alerting systems was discussed in Chapter 8.

The major results of this work are summarized in section 9.2. In addition, several of the methods and techniques which were developed in the context of microburst alerting also have potential applications to other problems. These methods are highlighted in Section 9.3.

9.2 Summary of Major Results

9.2.1 Cockpit Presentation of Microburst Alerts

The results from the Terminal Area Windshear Survey and the two piloted part-task simulator studies relate to the alert application task, and can be categorized into several groups. The first group concerns microburst alert presentation format:

- Iconic graphical presentation of alerts is more effective than either alphanumeric or verbal presentation. Alphanumeric alert presentation, in particular, is to be avoided. The EHSI was found to be an effective display for graphical alerts.

- Microburst alerts must contain at a minimum intensity and position information. Microburst motion and intensity trends may also be useful.

- Display of multiple microburst intensity levels appears to aid crew decision-making, and contains implicit intensity trend information.

Several procedural implications of using graphical microburst alerts in the cockpit were observed during the piloted simulations:

- The positional information contained in graphical alerts allowed crews to plan and request lateral avoidance maneuvers for missed approaches in advance.

- When faced with an iconic graphical microburst alert on the approach course, pilots made their decision to execute a missed approach approximately 4 nm from the identified microburst region.

- Pilots appear to be unwilling to penetrate or pass within several miles of an identified microburst region of *any* strength, and may make emergency deviations to avoid such regions. This may complicate ATC's task of maintaining safe aircraft separation.

One final point was apparent from survey results and pilot comments during simulator runs, and has been reinforced by operational experiences:

- PIREPs of wind shear are critically important. A reliable system for PIREP collection and distribution would improve alerting effectiveness.

It should be noted that ATC personnel did not take part in any of the studies, so the above conclusions apply only to flight crew alerting.

9.2.2 Microburst Alert Generation

Two studies were related to the alert generation task. The goal of these studies was to provide multi-level alert information which can be formatted, disseminated, and presented as iconic graphical microburst alerts.

Comparison of Microburst Hazard Criteria. As described in Chapter 3, the alert generation process requires a microburst "hazard criterion," a measureable quantity which provides an indication of the microburst aviation hazard. A good hazard criterion should correlate well with the impact of a microburst on an aircraft trajectory. A batch simulation technique was developed to compare several candidate hazard criteria, with the following results:

- Total headwind-to-tailwind change ("delta-V"), used by the TDWR and LLWAS systems, was not the best hazard criterion since it correlated poorly with aircraft trajectory degradation.

- The "F-factor" hazard criterion, when averaged over 3000 feet (approx. 1 km) along the flight path, is a good indication of microburst hazard and the best overall criterion of those considered.

- "Mean shear", the total headwind-to-tailwind change divided by the distance over which it occurs, is better than "delta-V" for the approach and landing phase fo flight, but did not correlate as well with aircraft trajectory degradation for the takeoff phase of flight.

A Technique for Establishing Multi-Level Alert Thresholds. Once a suitable hazard criterion has been selected, an alert structure must be defined which is based on threshold

values of the hazard criterion. A technique has been developed for determining microburst alert hazard thresholds based on predicted aircraft performance loss. In this method, alert levels are defined for specific levels of aircraft trajectory degradation. The relationship between measured values of the hazard criterion and the level of aircraft trajectory degradation is determined through flight simulation. The resulting relationship is then used to select threshold values of the measureable hazard criterion which correspond to the desired levels of aircraft trajectory degradation. The technique was demonstrated for the specific case of jet transports on final approach. A three-level alert structure was established, based on a trajectory degradation parameter which indicated whether or not the approach should be aborted.

9.2.3 Model-Based Estimation of Microburst Characteristics

The above techniques for alert generation require good information about the microburst windfield. A recursive model-based data fusion algorithm for multi-sensor estimation of microburst hazard characteristics was developed to accomplish this. Its capabilities were demonstrated via simulation. The algorithm approximates the actual windfield with a simple analytical microburst model, and a "best" set of model parameters are estimated from measured winds using an extended Kalman filtering technique. The resulting parameter estimate and associated error covariance encapsulate the current state of knowledge about the actual windfield, and can be used to compute estimates of microburst position, extent, and intensity (hazard criterion values) for alert generation. The algorithm takes advantage of fluid dynamic relationships and statistical data from past microburst field studies to aid the estimation process. The technique has the following advantages:

- Quantities which cannot be directly measured can be inferred from the fluid dynamic and statistical information in the model.
- Data from multiple sensors can be "fused" to alleviate problems due to poor sensor geometry.

- Large amounts of information are encapsulated by a small number of model parameters, which is desirable for data transmission.

- Microburst extent and hazard criteria for iconic graphical alerts can be easily computed from the estimated model parameters.

9.3 Extension of Methods and Techniques

Two techniques developed in the course of this microburst alerting research have useful applications to other problems.

9.3.1 Evaluating Prototype Cockpit Systems Via Piloted Part-Task Simulation

The part-task piloted flight simulation approach developed to evaluate candidate microburst alert formats has also been successfully used to study several other prototype advanced cockpit information systems. The main features of the approach are summarized below:

- The area of interest is the impact of advanced cockpit information systems on pilot decision-making performance, workload, and situational awareness. This allows a part-task approach in which outer-loop command and guidance tasks are accurately simulated at the expense of realism in the inner-loop flying task.

- The part-task approach brings a simplicity which greatly reduces experiment development and setup time.

- The use of a workstation-class computer with advanced graphics capabilities allows rapid prototyping of new systems and displays.

Other advanced cockpit information system concepts which have been studied using this simulator include electronic instrument approach plates [Mykityshyn and Hansman, 1990], terrain awareness and alerting displays [Kuchar and Hansman, 1991], and ATC routing amendment delivery via digital datalinks [Hahn and Hansman, 1992].

9.3.2 Applying the Data Assimilation Algorithm to Other Measurement Problems

The model-based data assimilation algorithm discussed in Chapter 7 is a novel application of estimation theory to meteorological measurement problems. Although it was implemented for measurement of microburst characteristics, the essential structure of the algorithm is quite general and can easily be adapted to other multi-sensor measurement problems. The following elements are required:

- A parametric analytical model of the phenomenon of interest, which satisfies essential physical relationships (such as fluid dynamic mass continuity). The model must include once-differentiable equations relating the available measurements to the model parameters.
- Statistical data on characteristics of the phenomenon which can be used to establish filter initial conditions and process noise parameters.
- Statistical characteristics of the measurement process.

The advantages of the model-based technique, notably the benefits of sensor fusion, the ability to infer quantities that cannot be directly measured, and the encapsulation of large amounts of data in a short parameter list, are also general and would apply to the new application also.

References

Adamson, H.P., 1988: Airborne Passive Infrared System for the Advance Warning of Low-Level Windshear and Clear Air Turbulence: 1988 In-Service and Theoretical Work. *AIAA Conference on Sensors and Measurement Techniques for Aeronautical Applications,* AIAA-88-4659, Atlanta, GA.

Andry, A. N., Shapiro, E. Y., and Chung, J. C., 1983: Eigenstructure Assignment for Linear Systems. *IEEE Transactions on Aerospace and Electronic Systems,* Vol. AES-19, No. 5, September.

Biron, P. J., and Isaminger, M. A., 1991: *High Resolution Microburst Outflow Vertical Profile Data from Huntsville, Alabama, and Denver, Colorado,* Project Report ATC-163, Lincoln Laboratory, Massachusetts Institute of Technology, Lexington, MA.

Bowles, Roland L., 1990: Reducing Windshear Risk Through Airborne Systems Technology. *17th Congress of the International Council of the Aeronautical Sciences,* Stockholm, Sweden.

Bracalente, E., 1992: Doppler Radar Results. NASA CP-10105, *Airborne Wind Shear Detection and Warning Systems: Fourth Combined Manufacturers' and Technologists' Conference,* Williamsburg, VA.

Campbell, Steven D., Merritt, Mark W., and DiStefano, John T., 1989: Microburst Recognition Performance of TDWR Operational Testbed. *Preprints, 3th International Conference on Aviation Weather Systems,* Anaheim, CA.

Campbell, Steven D., 1991: Performance Results and Potential Operational Uses for the Prototype TDWR Microburst Prediction Product. *Preprints, 4th International Conference on Aviation Weather Systems,* Paris, France.

Campbell, Steven, Lincoln Laboratory, 1992: Personal Communication.

Chandra, Divya, 1989: *An Evaluation of Automation for Flight Path Management in Transport Category Aircraft.* SM Thesis, Department of Aeronautics and Astronautics, Massachusetts Institute of Technology, Cambridge, MA.

Cornman, Larry B., and Mahoney, William P. III, 1991: Integration of the TDWR and LLWAS Wind Shear Detection Systems. *Preprints, 4th International Conference on Aviation Weather Systems,* Paris, France.

Evans, James E., 1991: Status of the Terminal Doppler Weather Radar One Year Before Deployment. *Preprints, 4th International Conference on Aviation Weather Systems,* Paris, France.

Federal Aviation Administration (FAA), 1987: *Windshear Training Aid.*

Federal Aviation Administration (FAA), 1990: *Airborne Windshear Warning and Escape Guidance Systems For Transport Airplanes.* Technical Standard Order C117.

Federal Aviation Administration (FAA), 1991: *Microburst Shear Integration Algorithm Description; Attachment A, TDWR Microburst Alert Generation Issues.* Federal Specification ER-500-92/02

Fletcher, R., 1970: A New Approach to Variable Metric Algorithms. *The Computer Journal,* Vol. 3, No. 3, August.

Fujita, T. T. and Byers, H. R., 1977: Spearhead Echo and Downbursts in the Crash of an Airliner. *Monthly Weather Review,* 105, 129-146.

Fujita, T. T., 1985: *The Downburst: Microburst and Macroburst.* Satellite and Mesometeorology Research Project, Department of the Geological Sciences, University of Chicago.

Fujita, T. T., 1986: *DFW Microburst on August 2, 1985.* The University of Chicago.

Gelb, A., ed., 1974: *Applied Optimal Estimation.* MIT Press, Cambridge, MA.

Hallowell, Robert, G., 1990: Aspect Angle Dependence of Outflow Strength in Denver Microbursts: Spatial and Temporal Variations. *16th Conference on Severe Local Storms,* Kananaskis Park, Alberta, Canada.

Hart, S.G., and Staveland, L.E., 1986: Development of NASA-TLX (Task Load Index): Results of Empirical and Theoretical Research, in P.A. Hancock and N. Meshkati (Eds.), *Human Mental Workload.* Elsevier Science Publishers, Amsterdam.

Hahn, E., and Hansman, R. J., 1992: Experimental Studies on the Effect of Automation on PilotSituational Awareness in the Datalink ATC Environment. *SAE Aerospace Technology Conference and Exposition '92,* Anaheim, CA.

Hinton, David A., 1989: *Piloted-Simulation Evaluation of Recovery Guidance for Microburst Wind Shear Encounters.* NASA Langley Research Center, NASA TP-2886, DOT/FAA/DS-89/06.

Hinton, David A., 1990: *Relative Merits of Reactive and Forward-Look Detection for Wind-Shear Encounters During Landing Approach for Various Microburst Escape Strategies.* NASA TM-4158, DOT/FAA/DS-89/35.

Hinton, David A., NASA Langley Research Center, 1992: Personal Communication.\

Hjelmfelt, Mark. R., 1988: Structure and Life Cycle of Microburst Outflows Observed in Colorado. *Journal of Applied Meteorology,* Vol. 27, August.

Jazwinski, A. H., 1970: *Stochastic Processes and Filtering Theory.* Academic Press, New York.

Kuchar, J. K., 1990: *'MAP' - Electronic Approach Plate Prototyping Software Documentation.* MIT Aeronautical Systems Laboratory Report ASL-90-6.

Kuchar, J. K. and Hansman, R. J., 1991: *Advanced Terrain Displays for Transport Category Aircraft.* MIT Aeronautical Systems Laboratory Report ASL-91-3.

Layton, Donald, 1988: *Aircraft Performance.* Matrix Publishers, Inc., Chesterland, OH.

Lewis, Michael S., 1993: Sensing a Change in the Wind. *Aerospace America,* Vol. 31, No. 1, January.

McCarthy, J., Blick, E. F., and Bensch, R. R., 1979: *Jet Transport Performance in Thunderstorm Wind Shear Conditions.* NASA CR-3207.

McCarthy, John, and Sand, Wayne, 1990: Controller and Pilot Decision Making in Transmitting and Receiving Microburst Wind Shear Alerts from an Advanced Terminal Wind Shear Detection System. *Preprints, ICAO Human Factors Seminar,* Leningrad, U.S.S.R., April 3-7, 1990.

McKissick, B., 1992: Flight Test of an Infrared Wind Shear Detector. NASA CP-10105, *Airborne Wind Shear Detection and Warning Systems: Fourth Combined Manufacturers' and Technologists' Conference,* Williamsburg, VA.

McRuer, D., Askkenas, I., and Graham, D., 1973: *Aircraft Dynamics and Automatic Control.* Princeton University Press, Princeton, NJ.

Midkiff, A. H. and Hansman, R. J., 1992: *Identification of Important "Party Line" Informational Elements and the Implications for Situational Awareness in the Datalink Environment.* Aeronautical Systems Lab Report 92-2, Department of Aeronautics and Astronautics, Massachusetts Institute of Technology, Cambridge, MA.

Moore, J. A., Cornman, L., and Biter, C., 1991: Terminal Doppler Weather Radar Program at Denver's Stapleton International Airport during 1989 and 1990. *Preprints, 4th International Conference on the Aviation Weather System,* Paris, France.

Merritt, M. W., Klingle-Wilson, D., and Campbell, S. D., 1989: Wind Shear Detection with Pencil-Beam Radars. *The Lincoln Laboratory Journal,* Vol. 2, No. 3.

Mulgund, S.S., and Stengel, R.F., 1992: Target Pitch Angle for the Microburst Escape Maneuver. AIAA 92-0730, *30th Aerospace Sciences Meeting and Exhibit,* Reno, NV.

Mykityshyn, M., and Hansman, R. J., 1990: *An Exploratory Survey of Information Requirements for Instrument Approach Charts.* MIT Aeronautical Systems Laboratory Report ASL-90-1-2.

Nadkarni, Arun, Boeing Commercial Airplane Company, 1988: Personal Communication.

National Center for Atmospheric Research (NCAR), 1988: *Terminal Doppler Weather Radar (TDWR): A Briefing Paper.*

National Research Council, 1983: *Low Altitude Wind Shear and Its Hazard to Aviation.* National Academy Press.

Oseguera, Rosa M. and Bowles, Roland L., 1988: *A Simple Analytic 3-Dimensional Model Based on Boundary Layer Stagnation Flow.* NASA TM-100632, NASA Langley Research Center, Hampton, VA,.

Proctor, F. H., 1987: *The Terminal Area Simulation System - Volume I: Thearetical Formulation; Volume II: Verification Cases.* NASA CR-4046 and CR-4047, DOT/FAA/PM-86/50.

Proctor, F.H., 1988: Numerical Simulations of an Isolated Microburst. Part I: Dynamics and Structure. *Journal of Atmospheric Science,* No. 45, pp. 3137-3160.

Proctor, F.H., 1989: Numerical Simulations of an Isolated Microburst. Part II: Sensitivity Experiments. *Journal of Atmospheric Science,* No. 46, pp. 2143-2165.

Rucker, R. A., and Flathers, G. W., 1988: The Future for Aeromobile Digital Communications. *IEEE/AIAA 8th Digital Avionics Systems Conference.*

Sand, W., and Biter, C., 1989: TDWR Display Experiences. AIAA 89-0807, *27th Aerospace Sciences Meeting,* Reno NV.

Scales, L. E., 1985: *Introduction to Non-Linear Optimization.* Springer-Verlag, New York.

Schlickenmaier, Herbert W., 1989: *Windshear Case Study: Denver, Colorado, July 11, 1988.* Federal Aviation Administration, DOT/FAA/DS-89/19.

Stevens, Brian L. and Lewis, Frank L., 1992: *Aircraft Control and Simulation.* John Wiley and Sons, New York.

Stevenson, Lloyd, 1989: *A PIREP-Based Analysis of the Candidate TDWR-Based Products and Services Evaluated at Stapelton International Airport During the Summer of 1988 (Draft Copy).* Federal Aviation Administration Project Memorandum DOT-TSC-FA9E 1-89, May 1989.

Stratton, D. Alexander, and Stengel, Robert F., 1992: Probabilistic Reasoning for Intelligent Wind Shear Avoidance. *Journal of Guidance, Control, and Dynamics,* Vol. 15, No. 1, Jan.-Feb.

Taylor, John W. R. (ed.), 1989: *Jane's All The World's Aircraft 1989-1990.* Jane's Information Group, Inc., Alexandria, VA.

Turkel, B. S., Kessel, P. A., and Frost, W., 1981: *Feasibility Study of a Procedure to Detect and Warn of Low-Level Wind Shear.* NASA CR-3480.

Vicroy, Dan. D., 1991: *A Simple, Analytical, Axisymmetric Microburst Model for Downdraft Estimation.* NASA Technical Memorandum 104053.

Vicroy, Dan D., 1992: Vertical Wind Estimation From Horizontal Wind Measurements. NASA CP-10105, *Airborne Wind Shear Detection and Warning Systems: Fourth Combined Manufacturers' and Technologists' Conference,* Williamsburg, VA.

Wanke, C., Chandra, D., Hansman, R.J., and Bussolari, S.R., 1990: A Comparison of Voice and Datalink for ATC Amendments and Hazardous Wind Shear Alerts. *4th International Symposium on Aviation and Space Safety,* Toulouse, France.

Wanke, C., and Hansman, R.J., 1989: Cockpit Display of Hazardous Weather Information. AIAA 89-0808, *27th Aerospace Sciences Meeting,* Reno NV.

Wanke, C., and Hansman, R.J., 1990: *Operational Cockpit Display of Ground-Measured Hazardous Windshear Information.* Aeronautical Systems Lab Report 90-4 (SM Thesis), Department of Aeronautics and Astronautics, Massachusetts Institute of Technology, Cambridge, MA.

Wanke, C., and Hansman, R.J., 1991: Alert Generation and Cockpit Presentation for an Integrated Microburst Alerting System. AIAA 91-0260, *29th Aerospace Sciences Meeting,* Reno NV.

Wanke, C., and Hansman, R.J., 1992b: Hazard Evaluation and Operational Cockpit Display of Ground-Measured Windshear Data. *Journal of Aircraft,* Vol. 29, No. 3.

Weber, M., Stone, M., Primeggia, C., and Anderson, J., 1991: Airport Surveillance Radar Based Wind Shear Detection. *Preprints, 4th International Conference on the Aviation Weather System,* Paris, France.

Wolfson, M.M. 1988: Characteristics of Microbursts in the Continental United States. *The Lincoln Laboratory Journal,* Vol. 1, No. 1, pp. 49-74.

Wilson, F. W. and Gramzow, R. H., 1990: An Intense Microburst at Denver's Stapleton International Airport. *Proceedings of the Air Traffic Control Association,* Boston.

Wilson, F. W., and Gramzow, R. H., 1991: The Redesigned Low Level Wind Shear Alert System. *Preprints, 4th International Conference on the Aviation Weather System,* Paris, France.

Wilson, J. W., Roberts, R. D., Kessinger, C., and McCarthy, J., 1984: Microburst Wind Structure and Evaluation of Doppler Radar for Airport Wind Shear Detection. *Journal of Climate and Applied Meteorology,* Vol. 29.

Hjelmfelt, Mark. R., 1988: Structure and Life Cycle of Microburst Outflows Observed in Colorado. *Journal of Applied Meteorology,* Vol. 27.

Wishner, R. P., Tabaczynski, J. A., and Athans, M., 1969: A Comparison of Three Non-Linear Filters. *Automatica,* Vol. 5.

Appendix A. Terminal Area Windshear Survey

The Department of Aeronautics and Astronautics at the Massachusetts Institute of Technology is currently doing research in low-level windshear detection and warning procedures, specifically the transmission of windshear data from ground sensors to the flight crew. The first step in this research is to conduct a survey of pilot opinions regarding current and possible future terminal area windshear alert procedures.

Participation in this survey is completely voluntary. It is not necessary to give your name at any point, and you may decline to answer any of the questions. All information obtained from any individual survey will remain confidential. If you have any questions, feel free to contact :

Prof. R. John Hansman
Aeronautical Systems Laboratory
MIT Rm. 33-115
77 Massachusetts Ave.
Cambridge, MA 02139
(617) 253-2271

Please return this survey in the enclosed stamped envelope. Thank you for your time and cooperation.

Transport Category Aircraft Flight Experience

Aircraft Type	Position	Apprx. Flight Hours

Approximate Total Flight Hours Over the Last Year _____

A. Current Procedures

1) Terminal area windshear/microburst events pose a major safety hazard to transport category aircraft.

1	2	3	4	5
disagree strongly	disagree	neither agree nor disagree	agree	agree strongly

2) How much confidence do you have in current ATIS-distributed microburst cautions and forecasts?

1	2	3	4	5
no confidence		moderate confidence		total confidence

3) Listed below are four currently available sources of information about windshear in the terminal area. Please rank them in order of usefulness, from 1 (most useful) to 4 (least useful).

_____ Low Level Windshear Alert System (LLWAS)
_____ Pilot Reports (PIREPS)
_____ Airborne Weather Radar
_____ Visual Clues (Thunderstorms, Virga etc.)

4) Here is a sample Low Level Windshear Alert (LLWAS) alert message:

Windshear alert. Centerfield wind 270 at 10. East boundary wind 180 at 25.

a) How useful to you is the data content of LLWAS messages?

1	2	3	4	5
useless		moderately useful		very useful

b) Is the data presented in a clear and understandable format?

1	2	3	4	5
very confusing				very clear

c) How often does the data get to you in time to be of use?

1	2	3	4	5
never		about half of the time		always

d) LLWAS is an effective method of preventing hazardous windshear encounters in the terminal area.

1	2	3	4	5
disagree strongly	disagree	neither agree nor disagree	agree	agree strongly

5) a) How effective is airborne weather radar for detection and avoidance of microbursts?

1	2	3	4	5
ineffective				very effective

b) How often do you use your weather radar in the terminal area?

1	2	3	4	5
never		about half of the time		always

c) What are your reasons for using or not using weather radar in the terminal area?

6) How much confidence do you have in pilot reports (PIREPS) of windshear?

1	2	3	4	5
no confidence		moderate confidence		total confidence

7) Currently available windshear alert data is sufficient for safe operation in the terminal area.

1	2	3	4	5
disagree strongly	disagree	neither agree nor disagree	agree	agree strongly

8) Given that new ground-based doppler weather radars can produce reliable windshear information, a system to provide aircrews with better and more timely windshear alerts is necessary.

1	2	3	4	5
disagree strongly	disagree	neither agree nor disagree	agree	agree strongly

B. Future Windshear Warning Systems

1) Assuming windshear is detected by reliable ground-based sensors, how should this information be relayed to the flight deck? Please rank in order of preference. (1 = most preferable, 5 = least preferable)

_____ Voice (ATIS)

_____ Voice (ATC)

_____ Alphanumeric/Text uplink (similar to ACARS)

_____ Graphical display of windshear location on EFIS display

_____ Graphical display of windshear location on separate graphic device

2) Assume a microburst has been detected which conflicts with your flight path in the vicinity of the runway threshold. When should you be alerted? Please rank the following in order of preference. (1 = most preferable, 5 = least preferable)

_____ On ATIS

_____ When entering terminal area (approx. 10000 ft. AGL)

_____ When cleared for approach

_____ At outer marker (approx. 2000 ft. AGL)

_____ As soon as detected, whatever the aircraft location

3) Listed below are possible microburst locations. How important is it to be alerted for each condition? Please rate each condition individually (i.e. don't rank them) on a scale of 1 to 4, where 1 indicates unimportant and 4 indicates critically important.

_____ Anywhere within 5 nm of destination airport

_____ Anywhere within 10 nm of destination airport

_____ Anywhere within 25 nm of destination airport

_____ Within 2 nm laterally of final approach path (inside marker) and runway

_____ Within 2 nm laterally of final approach path (inside marker) and runway and on published missed approach path

4) For the equipment that you most often fly (Type: _____), what do you consider to be the minimum head-to-tailwind component (i.e. airspeed loss) which requires a windshear advisory? _____ kts. What minimum component is required for a windshear warning? _____ kts.

5) A windshear alert could contain the following items of information. Please rank them in order of importance. (1 = most important, 6 = least important)

_____ Location

_____ Intensity

_____ Size

_____ Shape

_____ Intensity Trends

_____ Movement

6) Improved ground-based systems can reliably detect windshear events and provide useful real-time data. The responsibility for judging the threat due to a particular windshear event from the available data should lie with; (choose one)

a) the controller

b) the pilot

Please comment briefly on your decision.

7) Have you ever had a potentially hazardous windshear encounter? If so, please describe it briefly.

8) Please add any comments or suggestions you have.

Appendix B. Jet Transport Simulation Model

B.1 Longitudinal Point-Mass Aircraft Model

The aircraft model used in the Chapter 6 simulation work was based on data provided by David Hinton of NASA Langley Research Center. The model is for a Boeing 737-100 aircraft. Since short-scale aircraft motions were not of interest in this work, a two degree-of-freedom point-mass aircraft dynamic model was used in which pitching motions were neglected. The equations of motion (see Nomenclature for symbol definitions) were written as follows:

$$\dot{V} = \frac{T}{m}\cos\alpha - \frac{D}{m} - g\sin\gamma_a - \dot{W}_x\cos\gamma_a - \dot{W}_h\sin\gamma_a \tag{B.1}$$

$$\dot{\gamma}_a = \frac{1}{V}\left[\frac{T}{m}\sin\alpha + \frac{L}{m} - g\cos\gamma_a + \dot{W}_x\sin\gamma_a - \dot{W}_h\cos\gamma_a\right] \tag{B.2}$$

$$\dot{x} = V\cos\gamma_a + W_x \tag{B.3}$$

$$\dot{h} = V\sin\gamma_a + W_h \tag{B.4}$$

$$\alpha = \theta - \gamma_a \tag{B.5}$$

Lift and drag coefficients were given as functions of angle of attack, flap position, and gear position. C_L and C_D for a given flap position were given by:

$$C_L = A_0 + A_1\,\alpha + A_2\,\alpha^2 \tag{B.6}$$

$$C_D = B_0 + B_1\,\alpha + B_2\,\alpha^2 + B_3\,\alpha^3 \tag{B.7}$$

where the angle of attack, α, is given in degrees. The A and B coefficients were tabulated for the possible flap positions. For the lift coefficient, two sets of values were given; one for α below a breakpoint value, and one for α above that value. This data is given in Table B.1.

Table B.1. Lift and drag coefficient data, Boeing 737-100 aircraft. Provided by David Hinton of NASA Langley Research Center. AOA = angle of attack. Note that B values hold for all AOA. Flap settings are in degrees.

Flaps	AOA range	A_0	A_1	A_2	B_0	B_1	B_2	B_3
1	< 15° ≥ 15°	0.06 -2.03	0.1121 0.4	-0.0001 -0.01	0.03648	0.0006548	9.2532E-5	2.2186E-5
5	< 14° ≥ 14°	0.19 0.50	0.1136 0.09	-0.0001 0	0.039	0.0028167	4.1667E-5	2.5E-5
10	< 14° ≥ 14°	0.26 -2.32	0.1170 0.4867	-0.00009 -0.01333	0.05194	-0.00149	7.6563E-4	-2.6042E-6
15	< 12° ≥ 12°	0.384 -1.02	0.135 0.36	-0.0010 -0.01	0.0516	0.006135	-1.5625E-5	2.8646E-5
25	< 9° ≥ 9°	0.50 0.5025	0.1518 0.16	-0.00156 -0.0025	0.075	0.001764	9.01E-3	-7.3718E-6
30	< 11° ≥ 11°	0.9064 0.275	0.1452 0.2675	-0.0016 -0.0075	0.119	0.00759	4.57E-4	5.075E-6

If the landing gear is extended, the following incremental drag coefficient is added:

if $\delta_f < 25$,

$$C_{D_{GEAR}} = 0.0349 - 0.00069\delta_f - 0.0006\alpha \tag{B.8}$$

else,

$$C_{D_{GEAR}} = 0.059 - 0.0012\delta_f - 0.00126\alpha \tag{B.9}$$

where δ_f is the flap position. The "stick-shaker" angle-of-attack was given by the following relation:

if $\delta_f < 2$,

$$\alpha_{SS} = 12.0 + 4.95\delta_f - 1.55\delta_f^2 \tag{B.10}$$

else if $\delta_f < 25$,

$$\alpha_{SS} = 16.12 - 0.2186\delta_f + 0.00472\delta_f^2 \tag{B.11}$$

else,

$$\alpha_{SS} = 28.85 - 0.935\delta_f + 0.013\delta_f^2 \tag{B.12}$$

For final approach simulation, the glideslope altitude deviation, d, was computed from:

$$\dot{d} = V\sin(\gamma_i - \gamma_{GS}) \qquad \text{where } \gamma_{GS} = 3° \tag{B.13}$$

B.2 Control Laws for Correlation Studies

For the correlation studies, control laws were designed for both final approach and takeoff/climbout.

Approach Tracking. The final approach controller was a two-loop system. The inner loop was a two-input, two-output controller with proportional-plus-integral (PI) compensation for direct airspeed and flight path angle command-following. The inner loop structure is shown in Figure B.1. First-order lags were used to simulate the throttle and pitch command responses.

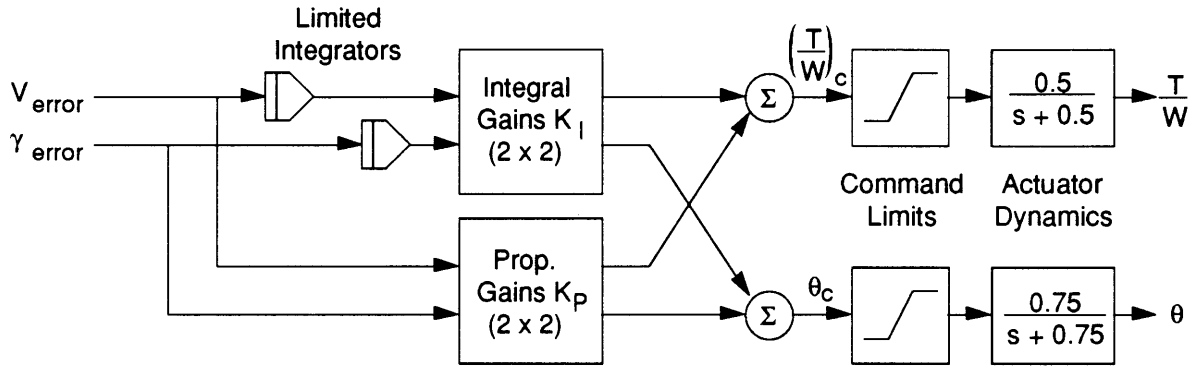

Figure B.1. Inner loop airspeed and flight path angle controller.

The gains for this loop were selected by an eigenstructure assignment technique. The equations of motion B.1 and B.2 were linearized about a stabilized 3° glideslope approach condition. Note that this linearization requires a non-linear iteration to compute the trim conditions, α_0 and T_0, for a specified reference airspeed, V_0, and flight path angle, γ_0. For control design, winds are neglected and the wind-relative flight path angle, γ_a, is identically equal to the inertial flight path angle, γ_i. The linearized aircraft system was written in state space form:

$$\begin{bmatrix} \dot{V} \\ \dot{\gamma} \end{bmatrix} = \mathbf{A}\begin{bmatrix} V \\ \gamma \end{bmatrix} + \mathbf{B}\begin{bmatrix} T/W \\ \theta \end{bmatrix} \tag{B.14}$$

$$A = \begin{bmatrix} \dfrac{-\rho S V_0 C_{D_0}}{m} & \dfrac{\rho S V_0^2 C_{D_\alpha}}{2m} - g\cos\gamma_0 \\ \dfrac{-T_0\alpha_0}{mV_0^2} + \dfrac{\rho S C_{L_0}}{2m} + \dfrac{g\cos\gamma_0}{V_0^2} & \dfrac{-T_0}{mV_0} - \dfrac{\rho S V_0 C_{L_\alpha}}{2m} \end{bmatrix} \tag{B.15}$$

$$\mathbf{B} = \begin{bmatrix} g & \dfrac{-\rho S V_0^2 C_{D_\alpha}}{2m} \\ \dfrac{\alpha_0 g}{V_0} & \dfrac{T_0}{mV_0} + \dfrac{\rho S V_0 C_{L_\alpha}}{2m} \end{bmatrix} \tag{B.16}$$

Note that the polynomial expressions for C_D and C_L were also linearized about the trim angle of attack, such that:

$$C_L \cong C_{L_0} + C_{L_\alpha}\alpha \tag{B.17}$$

$$C_D \cong C_{D_0} + C_{D_\alpha}\alpha \tag{B.18}$$

The linearized aircraft model (B.10) was augmented by the integrator channels in the compensator to form a 4-state linear system for design:

$$\begin{bmatrix} \dot{V} \\ \dot{\gamma} \\ \dot{z}_1 \\ \dot{z}_2 \end{bmatrix} = \begin{bmatrix} \mathbf{A} & \mathbf{0} \\ \mathbf{0} & \mathbf{I} \end{bmatrix} \begin{bmatrix} V \\ \gamma \\ z_1 \\ z_2 \end{bmatrix} + \begin{bmatrix} \mathbf{B} \\ \mathbf{0} \end{bmatrix} \begin{bmatrix} T/W \\ \theta \end{bmatrix} \tag{B.19}$$

The actuator dynamics were neglected in the design process. A full-state feedback eigenstructure assignment technique as described by Andry, et. al. [1983] was applied to compute the feedback gains. When full-state feedback is used on a system with n states and m inputs: (1) all n poles can be arbitrarily specified, and (2) m entries of each eigenvector can be arbitrarily chosen. For the system in B.18, all four poles can be placed, and two elements of each eigenvector can be specified. This latter property was used to *decouple* the airspeed and flight path angle channels, such that an airspeed change command would not change the flight path angle and vice-versa. The dominant airspeed

pole was chosen at (s = -0.2), and the dominant flight path pole was chosen at (s = -0.3). The values in the feedback gain matrix were computed by solving a generalized eigenvalue problem [Andry, et. al., 1983]. The final control law is shown below, with definitions as used in Figure B.1:

$$\begin{bmatrix} (T/W)_c \\ \theta_c \end{bmatrix} = \mathbf{K}_I \begin{bmatrix} z_1 \\ z_2 \end{bmatrix} + \mathbf{K}_P \begin{bmatrix} V_{error} \\ \gamma_{error} \end{bmatrix} \tag{B.20}$$

$$\mathbf{K}_I = \begin{bmatrix} 0.0020 & 0.088 \\ -3.45\times10^5 & 0.183 \end{bmatrix} \qquad \mathbf{K}_P = \begin{bmatrix} 0.018 & -0.525 \\ 0.0010 & -0.012 \end{bmatrix} \tag{B.21}$$

An outer loop was then designed which fed back glideslope deviations to commanded flight path angle (Figure B.2). Two different glideslope autopilots were designed. Autopilot A used pure gain feedback, and autopilot B used a dynamic compensator. The closed-loop characteristics for both autopilots are summarized in Table B.2.

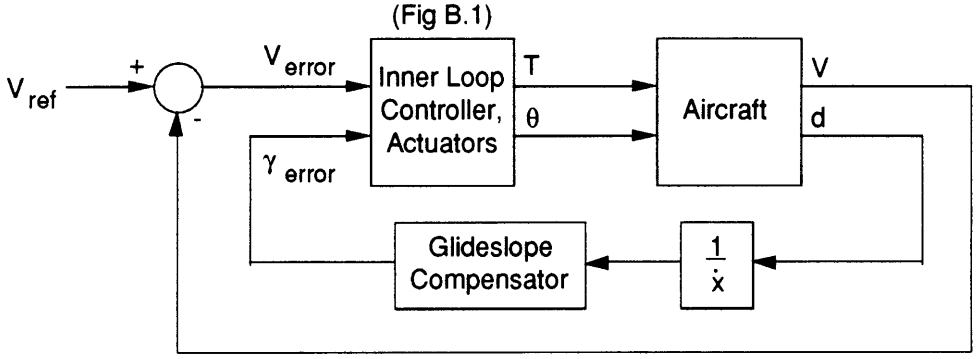

Figure B.2. Glideslope tracking controller for hazard correlation study.

Table B.2. Glideslope tracking controller characteristics.

Autopilot	Glideslope Compensator (see Fig. B.2)	Dominant mode characteristics Damping Ratio	Frequency, rad/sec
A	0.1	0.65	0.16
B	$\frac{1.35(s+0.3)(s+0.5)}{(s+1)^2}$	0.78	0.38

Takeoff Control Strategy. In the takeoff and climbout runs, the aircraft was under open-loop control. Maximum available thrust was applied at all times. During takeoff

roll, the pitch angle was set to 8°. The equation for airspeed (B.1) was augmented by a friction term, and with zero flight path angle during the takeoff roll becomes:

$$\dot{V} = \frac{T}{m}\cos\alpha - \frac{D}{m} - \dot{W}_x - \mu\left(g - \frac{L}{m}\right) \tag{B.22}$$

where $\mu = 0.02$ for rolling tires on a concrete runway [Layton, 1988]. When rotation airspeed V_r was reached, the climbout trim pitch angle was commanded. The trim pitch angle was chosen to achieve an airspeed of V_r + 15 knots. This pitch angle was maintained during the climbout, unless the angle-of-attack fell to the stick shaker angle-of-attack. In this case, the pitch angle was lowered to prevent stick shaker onset. Rotation airspeed was given by the following table as a function of takeoff weight and flaps:

Table B.3. Rotation airspeeds (KIAS) for Boeing 737-100 aircraft.

	Takeoff Weight (thousands of pounds)				
Flaps	70	80	90	100	110
1	116	125	133	142	151
5	110	119	128	138	147
15	104	114	123	132	140

B.3 Generalized Equations of Motion

For the hazard threshold study (Section 6.3) the primary equations of motion were rewritten as follows:

$$\dot{V} = g\left[\left(\frac{T}{W}\right)\cos\alpha - \frac{\rho V^2 C_D}{2\left(W/S\right)} - \sin\gamma_a\right] - \dot{W}_x\cos\gamma_a - \dot{W}_h\sin\gamma_a \tag{B.23}$$

$$\dot{\gamma}_a = \frac{g}{V}\left[\left(\frac{T}{W}\right)\sin\alpha + \frac{\rho V^2 C_L}{2\left(W/S\right)} - \cos\gamma_a\right] + \dot{W}_x\sin\gamma_a - \dot{W}_h\cos\gamma_a \tag{B.24}$$

In this form the aircraft wing loading (W/S) is specified rather than aircraft mass. The linearized equations (B.14 - B.16) were also converted to this form. The

approximate characteristics of 2, 3, and 4 engine jet transport aircraft, given in Table B.4, were used with the above equations. Note that the wing loading at maximum landing weight was assumed to be the same for all three aircraft types.

Table B.4. Generic jet transport model characteristics

No. of Engines	Wing Loading (lbf/sq. ft.)	Approach Speed (KIAS)	Excess Thrust-to-Weight Ratio
2	95.0	140	0.17
3	95.0	150	0.13
4	95.0	160	0.11

B.4 Approach Controller for Hazard Threshold Study

For computation of hazard threshold values, a more "typical" transport aircraft controller was designed by classical multiloop techniques as described by Stevens and Lewis [1992] and McRuer, Ashkenas, and Graham [1973]. The model equations were linearized about a 3° glideslope approach, as before, and transfer functions were computed from the control inputs (thrust-to-weight ratio, pitch angle) to the desired controlled variables (airspeed, glideslope altitude error). The 3-engine transport approach speed (150 knots) was used to trim the model for controller design.

Actuator dynamics were assumed to be first order for thrust and second order for pitch angle. The pitch angle dynamics were chosen to be representative of a pitch angle command system for a transport aircraft as described in the references [Stevens and Lewis, 1992; McRuer, et. al., 1973]. The overall control structure is shown in Figure B.3.

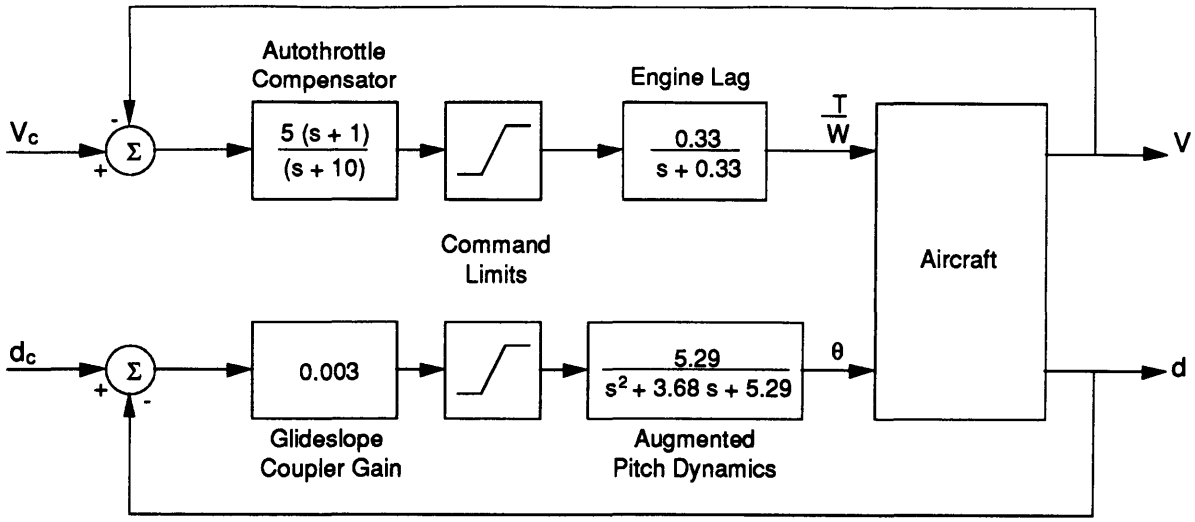

Figure B.3. Airspeed and glideslope tracking system for the generic jet transport model.

The command limits for the autothrottle channel were the idle thrust-to-weight ratio (lower limit) and the max thrust-to-weight ratio (upper limit). Max thrust-to-weight ratio was computed from the excess thrust-to-weight ratio given in Table B.4 using the drag-to-weight ratio at the approach trim condition. The upper pitch command limit was set by the stick shaker angle of attack, and there was no need to enforce a lower limit.

The autothrottle (airspeed control loop) was designed first. A lead-lag compensator was required to achieve a reasonable bandwidth. The closed loop airspeed response had a dominant mode natural frequency of 1.43 rad/sec with a damping ratio of 0.77. Next, the new transfer function from pitch command to glideslope error was computed and the glideslope tracking loop was closed. Acceptable characteristics were achieved with a pure gain closure; dominant mode natural frequency was 0.41 rad/sec with a damping ratio of 0.76. Time responses to an initial glideslope altitude error of 50 meters were presented in Figure 6.13.

B.5 Simulated Microburst Winds

TASS Winds. In the hazard criterion correlation study, several vertical slices were taken from a numerically-modeled microburst. Each vertical slice included two-axis winds (W_x, W_h) indexed by groundtrack distance and altitude. In the aircraft simulation, winds were computed from these slices by 2-D linear interpolation, and time derivatives in the aircraft frame of the 2-D earth-referenced winds ($\dot{W}_x$, $\dot{W}_h$) were computed as follows:

$$\dot{W}_x = \dot{x}\frac{\partial W_x}{\partial x} + \dot{h}\frac{\partial W_x}{\partial h} \tag{B.25}$$

$$\dot{W}_h = \dot{x}\frac{\partial W_h}{\partial x} + \dot{h}\frac{\partial W_h}{\partial h} \tag{B.26}$$

where the spatial derivatives of W_x and W_h were computed by two-dimensional central differencing. Note that the winds were time-invariant, so no actual time derivatives appear in the above equations. The wind gradients are due only to aircraft motion through a non-uniform wind field.

OBV Winds. For the hazard threshold study, the Oseguera-Bowles-Vicroy parametric microburst model was used. The analytical expressions for winds and spatial gradients in Appendix C were directly computed during the simulation runs, and equations B.25 and B.26 were used to evaluate $\dot{W}_x$ and $\dot{W}_h$.

Appendix C. Oseguera-Bowles-Vicroy Microburst Model Equations

C.1 Model Equations

This analytical microburst model was first proposed by Oseguera and Bowles [1988] and improved by Vicroy [1991]. It is an axisymmetric steady-flow model which employs radial and altitude-dependent shaping functions to satisfy the mass continuity equation. The W_{xE}, W_{yE}, and W_h microburst wind components are functions of relative position (x, y, h) and four model parameters:

U_m Maximum horizontal outflow velocity

R_p Microburst core radius

Z_m Altitude (AGL) of maximum horizontal wind velocity

α Shaping parameter (set to 2.0 for all of the work presented here)

$$W_{xE} = \frac{\lambda\tilde{x}}{2}\left[e^{C_1(h/Z_m)} - e^{C_2(h/Z_m)}\right]e^{\left[\frac{2-\left(\tilde{x}^2+\tilde{y}^2\right)^{\alpha}/R_p^{2\alpha}}{2\alpha}\right]} \tag{C.1}$$

$$W_{yE} = \frac{\lambda\tilde{y}}{2}\left[e^{C_1(h/Z_m)} - e^{C_2(h/Z_m)}\right]e^{\left[\frac{2-\left(\tilde{x}^2+\tilde{y}^2\right)^{\alpha}/R_p^{2\alpha}}{2\alpha}\right]} \tag{C.2}$$

$$W_h = -\lambda\left\{\frac{Z_m}{C_1}\left[e^{C_1(h/Z_m)} - 1\right] - \frac{Z_m}{C_2}\left[e^{C_2(h/Z_m)} - 1\right]\right\} \times\left[1 - \frac{\left(\tilde{x}^2+\tilde{y}^2\right)^{\alpha}}{2R_p^{2\alpha}}\right]e^{\left[\frac{2-\left(\tilde{x}^2+\tilde{y}^2\right)^{\alpha}/R_p^{2\alpha}}{2\alpha}\right]} \tag{C.3}$$

where, if the microburst center is located at (x_0, y_0), the position offsets are given by:

$$\tilde{x} = x - x_0 \tag{C.4}$$

$$\tilde{y} = y - y_0 \tag{C.5}$$

and the radial scale factor λ is:

$$\lambda = \frac{2U_m}{R_p\left(e^{C_1} - e^{C_2}\right)e^{(1/2\alpha)}} \tag{C.6}$$

C_1 and C_2 are empirically-adjusted constants with the following values:

$$C_1 = -0.15 \tag{C.7}$$

$$C_2 = -3.2175 \tag{C.8}$$

To compute wind gradients, equations for spatial derivatives of the winds are needed. These are:

$$\frac{\partial W_{xE}}{\partial x} = \frac{\lambda}{2}\left[e^{C_1(h/Z_m)} - e^{C_2(h/Z_m)}\right]\left[1 - \frac{\tilde{x}^2\left(\tilde{x}^2+\tilde{y}^2\right)^{\alpha-1}}{R_p^{2\alpha}}\right]e^{\left[\frac{2-\left(\tilde{x}^2+\tilde{y}^2\right)^{\alpha}/R_p^{2\alpha}}{2\alpha}\right]} \tag{C.9}$$

$$\frac{\partial W_{xE}}{\partial y} = \frac{-\lambda\tilde{x}\tilde{y}\left(\tilde{x}^2+\tilde{y}^2\right)^{\alpha-1}}{2R_p^{2\alpha}}\left[e^{C_1(h/Z_m)} - e^{C_2(h/Z_m)}\right]e^{\left[\frac{2-\left(\tilde{x}^2+\tilde{y}^2\right)^{\alpha}/R_p^{2\alpha}}{2\alpha}\right]} \tag{C.10}$$

$$\frac{\partial W_{xE}}{\partial h} = \frac{\lambda\tilde{x}}{2}\left[\frac{C_1}{Z_m}e^{C_1(h/Z_m)} - \frac{C_2}{Z_m}e^{C_2(h/Z_m)}\right]e^{\left[\frac{2-\left(\tilde{x}^2+\tilde{y}^2\right)^{\alpha}/R_p^{2\alpha}}{2\alpha}\right]} \tag{C.11}$$

$$\frac{\partial W_{yE}}{\partial x} = \frac{\partial W_{xE}}{\partial y} \tag{C.12}$$

$$\frac{\partial W_{yE}}{\partial y} = \frac{\lambda}{2}\left[e^{C_1(h/Z_m)} - e^{C_2(h/Z_m)}\right]\left[1 - \frac{\tilde{y}^2\left(\tilde{x}^2+\tilde{y}^2\right)^{\alpha-1}}{R_p^{2\alpha}}\right]e^{\left[\frac{2-\left(\tilde{x}^2+\tilde{y}^2\right)^{\alpha}/R_p^{2\alpha}}{2\alpha}\right]} \tag{C.13}$$

$$\frac{\partial W_{yE}}{\partial h} = \frac{\lambda\tilde{y}}{2}\left[\frac{C_1}{Z_m}e^{C_1(h/Z_m)} - \frac{C_2}{Z_m}e^{C_2(h/Z_m)}\right]e^{\left[\frac{2-\left(\tilde{x}^2+\tilde{y}^2\right)^{\alpha}/R_p^{2\alpha}}{2\alpha}\right]} \tag{C.14}$$

$$\frac{\partial W_h}{\partial x} = \frac{\lambda\tilde{x}\left(\tilde{x}^2+\tilde{y}^2\right)^{\alpha-1}}{R_p^{2\alpha}}\left\{\frac{Z_m}{C_1}\left[e^{C_1(h/Z_m)}-1\right]-\frac{Z_m}{C_2}\left[e^{C_2(h/Z_m)}-1\right]\right\}$$
$$\times\left[\alpha+1-\frac{\left(\tilde{x}^2+\tilde{y}^2\right)^{\alpha}}{2R_p^{2\alpha}}\right]e^{\left[\frac{2-\left(\tilde{x}^2+\tilde{y}^2\right)^{\alpha}/R_p^{2\alpha}}{2\alpha}\right]} \qquad \text{(C.15)}$$

$$\frac{\partial W_h}{\partial y} = \frac{\lambda\tilde{y}\left(\tilde{x}^2+\tilde{y}^2\right)^{\alpha-1}}{R_p^{2\alpha}}\left\{\frac{Z_m}{C_1}\left[e^{C_1(h/Z_m)}-1\right]-\frac{Z_m}{C_2}\left[e^{C_2(h/Z_m)}-1\right]\right\}$$
$$\times\left[\alpha+1-\frac{\left(\tilde{x}^2+\tilde{y}^2\right)^{\alpha}}{2R_p^{2\alpha}}\right]e^{\left[\frac{2-\left(\tilde{x}^2+\tilde{y}^2\right)^{\alpha}/R_p^{2\alpha}}{2\alpha}\right]} \qquad \text{(C.16)}$$

$$\frac{\partial W_h}{\partial h} = -\lambda\left[e^{C_1(h/Z_m)}-e^{C_2(h/Z_m)}\right]\left[1-\frac{\left(\tilde{x}^2+\tilde{y}^2\right)^{\alpha}}{2R_p^{2\alpha}}\right]e^{\left[\frac{2-\left(\tilde{x}^2+\tilde{y}^2\right)^{\alpha}/R_p^{2\alpha}}{2\alpha}\right]} \qquad \text{(C.17)}$$

C.2 Projection to Spherical Coordinates

Doppler radars or lidars measure the wind component radial to the sensor. At a given point, this component is the projection of the three-dimensional wind vector onto the one-dimensional subspace radial to the sensor. To use these measurements in either the least-squares technique or the IEKF algorithm, the relationship between the OBV winds (in Cartesian coordinates) and the radial component is needed. This relationship is the radial element of a transformation from Cartesian to spherical coordinates, where the coordinate axes are defined as shown in Table C.1.

Table C.1. Coordinate frames for wind component tranformations

Cartesian coordinates		Spherical coordinates	
x	East W_{xE} = wind velocity	r	Radial to sensor W_r = wind velocity
y	North W_{yE} = wind velocity	ψ	Azimuth angle North = 0 Positive clockwise
h	Up W_h = wind velocity	θ	Elevation angle from x-y plane Positive upward

The radial velocity W_r is a function of W_{xE}, W_{yE}, W_h, ψ, and θ as follows:

$$W_r = \left(W_{xE}\cos\psi + W_{yE}\sin\psi\right)\cos\theta + W_h\sin\theta \tag{C.18}$$

Similarly, the partial derivatives needed for the Jacobean, **J**, in the least-squares technique and for the measurement matrix, H_k, in the IEKF algorithm are:

$$\frac{\partial W_r}{\partial \mathbf{x}} = \left(\frac{\partial W_{xE}}{\partial \mathbf{x}}\cos\psi + \frac{\partial W_{yE}}{\partial \mathbf{x}}\sin\psi\right)\cos\theta + \frac{\partial W_h}{\partial \mathbf{x}}\sin\theta \tag{C.19}$$

where **x** is the parameter vector for the analytical microburst model, not to be confused with the east coordinate x. The derivatives in the preceding expression are quite complex, and were computed by repeated application of the derivative chain rule.

Appendix D. Microburst Model Matching Least-Squares Algorithm

An algorithm was developed to match a parametric microburst model to a set of wind measurements. The technique was an improved version of that used by Schultz [1990] to develop a vortex ring model of the Dallas-Fort Worth airport microburst [Fujita, 1986]. The algorithm computes the values of the n model parameters, **x**, which minimize the total mean squared error between a set of "truth" winds and the analytical model winds:

$$F(\mathbf{x}) = \frac{1}{m}\sum_{i=1}^{m}\left(z_{model,i}(\mathbf{x}) - z_{actual,i}\right)^2 b_i \qquad (D.1)$$

where m is the total number of measurement data points. $\mathbf{z}_{actual}$ is a column vector of all measurements at all (x, y, h) locations, which can include wind and/or spatial shear data. For the work in Chapter 7, three-axis winds (W_{xE}, W_{yE}, W_h) were used, so $\mathbf{z}_{actual}$ had 3 elements for each (x, y, h) measurement position. $\mathbf{z}_{model}$ is the vector of wind or shear values predicted by the analytical model at the appropriate measurement locations, using the current parameter set **x**. The weights b_i can be set to reflect confidence in particular measurements; a typical choice is to use the reciprocal of the measurement noise variances. The weights were identically 1 for the analysis in Chapter 7. Note that F(**x**) here is the scalar *objective function* for minimization, and should not be confused with F-factor.

The objective function F was minimized using a constrained version of the Gauss-Newton minimization technique for non-linear sum-of-squares functions [Scales, 1985]. When the objective function can be expressed as a sum of squares:

$$F(\mathbf{x}) = \sum_{i=1}^{m} f_i(\mathbf{x}) \qquad (D.2)$$

or in vector form,

$$F(\mathbf{x}) = \mathbf{f}^T(\mathbf{x})\mathbf{f}(\mathbf{x}) \tag{D.3}$$

$$\mathbf{f}(\mathbf{x}) = \begin{bmatrix} f_1 & f_2 & f_3 & \dots & f_m \end{bmatrix}^T \tag{D.4}$$

then a *search direction* at the k^{th} iteration, $\mathbf{p}_k$, can be computed by solving the following matrix equation:

$$\mathbf{J}_k^T \mathbf{J}_k \mathbf{p}_k = -\mathbf{J}_k^T \mathbf{f}_k \tag{D.5}$$

where $\mathbf{J}_k$ is the *Jacobean matrix:*

$$\mathbf{J} = \begin{bmatrix} \partial f_1/\partial x_1 & \cdot & \cdot & \cdot & \partial f_1/\partial x_n \\ \cdot & & & & \cdot \\ \cdot & & & & \cdot \\ \cdot & & & & \cdot \\ \partial f_m/\partial x_1 & \cdot & \cdot & \cdot & \partial f_m/\partial x_n \end{bmatrix} \tag{D.6}$$

Equation D.5 is solved by LU factorization to yield the search direction. $\mathbf{p}_k$ is used to update the parameter estimate as follows:

$$\mathbf{x}_{k+1} = \mathbf{x}_k + \alpha_k \mathbf{p}_k \tag{D.7}$$

In the simplest implementation, $\alpha_k = 1$ for all k. However, the convergence properties of the algorithm are enhanced when α_k is computed from a linear search. This search need not be very accurate. The procedure used here [Fletcher, 1970] ensures that a reasonable decrease in the objective function is achieved at each step. Initially, $\alpha_k = 1$. The new value of the objective function, F_{k+1}, is computed. A reasonable decrease in the objective function has been achieved if:

$$\text{if } F_{k+1} - F_k \le \mu\alpha_k \left(\mathbf{p}_k^T \bullet \mathbf{g}_k\right) \tag{D.8}$$

$$\mathbf{g}_k = \nabla F(\mathbf{x}_k) \tag{D.9}$$

in which case the search is terminated. Note that $\mathbf{g}_k$ is the *gradient* of $F(\mathbf{x}_k)$. If the test D.8 fails, the step α_k is multiplied by ω (where $0 \leq \omega \leq 1$), $\mathbf{x}_{k+1}$ and F_{k+1} are reevaluated, and the test is reapplied. The procedure ends either when D.8 is satisfied, in which case k is incremented and a new search direction is computed, or when α_k is reduced below a specified minimum value, in which case the minimization procedure is finished. For the work presented in Chapter 7, $\mu = 0.001$, $\omega = 0.5$, and the minimum value of $\alpha_k = 0.0001$.

The Gauss-Newton method (characterized by the search direction computation, D.5) is a simplification of Newton's minimization method. The full form of Newton's method requires evaluation of the *Hessian matrix* ($\nabla^2 F$). As a result, the Gauss-Newton algorithm requires much less computation. The Gauss-Newton method will converge correctly and at comparable rates to Newton's method for "small residual" problems in which the final minimum value of the objective function is small. It was found to converge quickly and for a wide range of initial conditions when used to match microburst winds with the OBV microburst model as in Chapter 7.

The above algorithm description is completely general; it is not limited to the OBV microburst model. The OBV model equations (Appendix C) are used to compute the objective function, F_k, and to compute the Jacobean, $\mathbf{J}$. Other microburst models can be used, provided that the wind equations are once-differentiable with respect to the model parameters to allow computation of $\mathbf{J}$. The algebraic derivative expressions used to compute $\mathbf{J}$ are complex, and evaluation of $\mathbf{J}$ (at least for the OBV model) is the most computationally-intensive part of the procedure.

The procedure could be further extended in several ways. A model which included a temperature equation, for example, could be used to match IR temperature measurements. Alternately, spatial gradients could be used as the measurements to generate a windfield which more closely matches wind shear rather than winds. Finally,

it would be straightforward to adapt the algorithm to other atmospheric phenomena for which parameters of an appropriate analytical model can be related to measured quantities by algebraic once-differentiable equations.